Spring 2008

Photoassociative Spectroscopy of Ultracold Metastable Argon and Study of Dual Species Trap Loss in a Rubidium-Metastable Argon MOT

Michael K. Shaffer
Old Dominion University

PHOTOASSOCIATIVE SPECTROSCOPY OF ULTRACOLD METASTABLE ARGON AND STUDY OF DUAL SPECIES TRAP LOSS IN A RUBIDIUM - METASTABLE ARGON MOT

by

Michael K. Shaffer
B.S. May 2002, Frostburg State University
M.S. August 2004, Old Dominion University

A Dissertation Submitted to the Faculty of
Old Dominion University in Partial Fulfillment of the
Requirement for the Degree of

DOCTOR OF PHILOSOPHY

PHYSICS

OLD DOMINION UNIVERSITY
May 2008

Approved by:

Charles I. Sukenik (Director)

Mark D. Havey (Member)

Gilbert R. Hoy (Member)

J. Wallace Van Orden (Member)

John R. Donat (Member)

ABSTRACT

PHOTOASSOCIATIVE SPECTROSCOPY OF ULTRACOLD METASTABLE ARGON AND STUDY OF DUAL SPECIES TRAP LOSS IN A RUBIDIUM - METASTABLE ARGON MOT

Michael K. Shaffer
Old Dominion University, 2008
Director: Dr. Charles I. Sukenik

This dissertation presents the findings of two experimental investigations in ultracold atomic and molecular physics: The study of the dual species trap loss in a rubidium - metastable argon magneto-optical trap and the photoassociative spectroscopy of ultracold metastable argon. The interspecies trap loss rate coefficients have been measured for ultracold collisions between ^{85}Rb and ^{40}Ar* in a dual-species magneto-optical trap (MOT) and the two rates have been found to be approximately equal over the range of intensities studied with values of $\beta'_{Rb-Ar*} = 3.0 \pm 1.3 \times 10^{-11}$ cm^3/s and $\beta'_{Ar*-Rb} = 1.9 \pm 0.9 \times 10^{-11}$ cm^3/s where β'_{Rb-Ar*} is the trap loss coefficient for Rb in the presence of Ar* and β'_{Ar*-Rb} is the reciprocal term. In addition, the trap loss rate coefficient for cold collisions in a metastable argon MOT alone have been measured with an average value of $\beta_{Ar*} = 5.2 \pm 1.6 \times 10^{-10}$ cm^3/s. Using a quadrupole mass spectrometer, the production of Ar^+, Ar_2^+, Rb^+, and $RbAr^+$ ions in the dual MOT have been observed, clearly identifying heteronuclear Penning and associative ionization as trap loss mechanisms. In the second experiment, the first ever investigation of the photoassociative (PA) spectroscopy of Ar* has been made. The exploratory study focuses on PA spectroscopy near the $4s[3/2]_2 + 4p[5/2]_3$ asymptote of the Ar_2* diatomic molecule over a 10 GHz range red detuned of the atomic resonance. With a range of probe laser intensities from $\sim 10^2 - 10^5 I_{Sat}$, 12 resonances have been observed. The spectra have been analyzed using the near-dissociation LeRoy-Bernstein method. Through this analysis, the spectra seem to best correlate with excitations to the 5_g state.

ACKNOWLEDGEMENTS

Of all my numerous experiences and relations that have brought me to this point in my life, it would be exceptionally unreasonable to even suggest that, in a single page or a thousand, I could properly express my deep thanks and gratitude to all who deserve to be acknowledged here. Though sometimes it goes unspoken, I am truly grateful for all things, small and great, that have made me who I am today and for that, I thank you wholeheartedly.

Dr. Charles Sukenik has, without a doubt, been key to a great and memorable graduate experience. His mentorship, coupled with his keen insight to physics, great sense of humor, and seemingly endless patience, has invoked nothing but growth and insight of my own, not only in the world of physics, but in life as well and I feel extremely fortunate to have worked in his laboratory.

I would also like to thank my dissertation committee members, Dr. Mark Havey, Dr. Gil Hoy, Dr. Wally van Orden, and Dr. John Donat for their comments and suggestions to improve my research. Many additional thanks to Dr. Havey for numerous discussions on physics, the occasional recreational ski trip, and most definitely his excellent quantum mechanics and atomic physics lectures.

Eman Ahmed and Gambhir Ranjit I thank for being such great lab members and friends, sharing jokes and "shocking" times, all the while getting research done. Gambhir, now has the Argon experiment, my office, and my pen... and that's ok. In a broad, encompassing, and hardly sufficient manner, I would like to thank the physics department faculty for their help and support and I would like to thank Walt Hooks, Annette Vialet, and Delicia Malin for keeping the grad students smiling, happy and (on occasion) fed. I also want to express thanks to all who contributed to the PGSA, especially the officers of the inaugural year, this year, and the years to come. Thank you Mike Mayer and Ana Samolov for taking the reigns and doing so much, Jan Drake and Jason Martinez, the list goes on. Ciao Saori. A special thanks, also, to our department chair Dr. Gail Dodge for her enthusiasm and unwavering support of the group.

To my dearest friends, especially Ray and Kat, thank you also, for your patience and helping me retain my sanity. Lastly, I would like to thank all of my family who have shown constant support and love and mean so much to me. Thank you so very much.

TABLE OF CONTENTS

LIST OF TABLES

LIST OF FIGURES

CHAPTER I

INTRODUCTION

Since the early stages of laser cooling, the field of ultracold physics, along with its many tools and techniques, has brought about numerous significant accomplishments in atomic and molecular physics. Beginning with the first application of using light to change the momentum of neutral atoms [1, 2], very soon afterwards neutral atoms were cooled and confined in the first magneto-optical trap (MOT) [3], which, two decades later, is still one of the most useful and versatile tools for conducting investigations at ultracold temperatures. These advances paved the way for the realization of Bose-Einstein Condensates in a variety of alkali atoms [4, 5, 6] as well as hydrogen [7] and metastable helium [8]. The coherence of these atomic samples led further to the development of more practical applications such as atom interferometers and wave guides [9] and atomic clocks [10] and even developments in quantum computing [11, 12, 13]. As development of new ideas and tools continues to expand, an interest in ultracold collisions and molecule production has emerged [14, 15], where by studying behavior at ultracold temperatures, the most fundamental of interactions can be observed. Interest in ultracold molecules is broad and multidisciplinary, including symmetry investigations [16], quantum chemistry, to even the production of ultracold polar molecules to be used as a quantum bit in quantum computing. The first reported cold molecules produced in MOTs were generally a homonuclear alkali such as Cs_2 [17, 18], Rb_2 [19], and K_2 [20]. That list quickly expanded to include heteronuclear alkali molecules such as KRb [21] and RbCs [22].

Photoassociative spectroscopy (PAS), the probing of free-bound transitions with high resolution, has proven to be a powerful tool for investigating ultracold atomic and molecular systems. In PAS, two free atoms, usually in the ground state, absorb a photon and form a bound, excited molecule. At ultracold temperatures, the low translational energy and narrow thermal distribution allow vibrational and rotational structure to be clearly resolved, even close to the dissociation limit. PAS can also be used for investigating states which are not accessible by conventional spectroscopy-like purely long-range states- and for isolating effects due to hyperfine structure. Pure long range states are of particular interest because, with inner classical turning points on the order of 100 a_0, their location and character depend almost exclusively on atomic parameters. PAS investigations can also aid in determining s-wave

scattering lengths which are important for calculating the elastic scattering rates in evaporative cooling making possible Bose-Einstein condensates and for determining the accuracy of frequency standards based on atomic clocks [23]. The empirical nature of spectroscopic experiments aside, photoassociation can also be used to influence the products of chemical reactions. Proper choices of laser frequencies and polarizations can be used to direct reactants towards specific reaction channels to either promote or discourage the production of a specific product. An example for this would be molecule production through photoassociation or optical shielding where ionization rates are largely suppressed [24, 25]. Accurate potential curves are also required in order to calculate relaxation rates in atom-molecule collisions, an area of growing interest in ultracold molecular physics studies. Though there are inherently more technical difficulties in making a rare gas MOT as compared to an alkali-metal MOT because of the need to provide atoms in the metastable state, there are a number of advantages in studying ultracold rare gas physics. Since the even isotopes of the noble gases have zero nuclear spin, they lack hyperfine structure. Though this simplifies the energy level structure of the atom, the fine structure splittings play an important role. Additionally, to cool and trap rare gases in a MOT, the atoms must be trapped while in a metastable state which typically has more than half the ionization potential of internal energy. This adds a degree of interest to the system because ionization is now a very probable collision channel. While in some experiments this can be a detrimental source of trap loss, in other experiments, such as those reported here, the ionization rate can be an important observable and the focus of the study itself.

This thesis focuses on the first two experiments in a research program aimed at the photoassociation Rubiudium-85 (^{85}Rb) and Argon-40 (^{40}Ar) in a metastable state (denoted Ar*) to form a RbAr ground state molecule. The first investigation detailed will be the Rb-Ar* dual species trap loss experiment. The second will be the photoassociative spectroscopy of Ar*.

In application to the long term goals of this research program, PAS can be used to study heteronuclear interactions as well as single-species dimers. To date, most of the investigations of heteronuclear ultracold systems have been in either dual alkali (Na/K [26], Na/Cs [27], Na/Rb[28], and Li/Cs [29]) or dual alkali isotope (^{85}Rb/^{87}Rb [30], ^{6}Li/^{7}Li[31], ^{84}Rb/^{87}Rb [32], Yb[33]) dimers. The long term goal of this research will be the photoassociation of Rb and Ar*, the first photoassociative investigation

of an alkali-rare gas system. In this thesis, the PAS of the Ar* homonuclear system is investigated as a step en route to the PAS of the Rb-Ar* dimer. This work represents the first photoassociative spectroscopic investigation of Ar* and the only PAS investigation of a metastable rare gas aside from recent work in He* [34].

The research program for RbAr molecule production and spectroscopy consists of a number of well-defined experimental steps. Each of these steps is designed to focus on the physics of the system at hand. Before the heteronuclear molecular system can be produced and investigated, a thorough understanding of the physics encountered along the way must be attained. The experiments in this research program are to:

1.) Investigate and characterize the collisional dynamics of Rb and Ar* at ultracold temperatures.

2.) Perform photoassociative spectroscopy on Ar*, accompanied with a spectral analysis (PA spectra for Rb are currently available).

3.) Perform photoassociative spectroscopy on the Rb-Ar* dimer.

4.) Verify the production of RbAr molecules.

5.) Trap RbAr molecule in a dipole force trap and perform spectroscopy.

This dissertation reports on items (1) and (2) above and is organized in the following way. In Chapter II, a summary of the physics concepts relevant to these experiments will be discussed, including the principles of light forces and atom cooling, the operation of the magneto-optical trap, ultracold binary collisions and photoassociative spectroscopy. Chapter III provides a detailed explanation of laser systems, vacuum systems, detection, data acquisition, as well as other various aspects of the experimental apparatus. Chapter IV discusses the setup and results of the Rb-Ar* dual species trap loss measurement experiment. In Chapter V, the details of the photoassociative spectroscopy of Ar* experiment are presented. Finally, the conclusion and future outlook of these experiments will be discussed in Chapter VI.

CHAPTER II

THEORETICAL BACKGROUND

In both the photoassociation of Ar* and Ar*-Rb trap loss experiments, atom-light and atom-atom interactions are intrinsic and vital to the functionality of the apparatus and the interpretation of the experimental results. A brief review of the theory of these interactions and their relevant extensions will be discussed in this chapter along with other physical characteristics of the atomic system.

II.1 GENERAL NOTATION FOR ATOMIC AND MOLECULAR STATES

In this experiment there are four quantum systems whose states should be well described. The Rb atom, the Ar atom, and the Ar_2 and RbAr molecules. While it would be convenient to use one notation to fully describe the states of each system, conventionally it is not the case. Detailed below are the notations chosen (by convention or otherwise) to describe the alkali atom, the rare gas atom, and the diatomic molecule.

Like other alkalis, ^{85}Rb has the ground state electron configuration of a closed core with one electron in its valence shell. Since the core shells are closed, these electrons do not contribute to the orbital angular momentum, leaving the total orbital momentum to be determined by the state of the one valence electron. In this case, it is convenient to describe the state of the atoms using Russell-Saunders notation

$$n^{2S+1}L_J \tag{1}$$

where n is the principle quantum number of the valence electron, $\vec{L} = \vec{l}$ is the total orbital angular momentum quantum number and $\vec{S} = \vec{s}$ is the total electronic spin. The total angular momentum of the electron is then $\vec{J} = \vec{l} + \vec{s}$. Since $\vec{J}$ is the vector sum of $\vec{L}$ and $\vec{S}$, the spin-orbit interaction, $V_{SO} = A\vec{L} \cdot \vec{S}$, needs consideration and introduces an energy level splitting referred to as fine-structure splitting. Additionally, there is further splitting due to the interaction between the nuclear spin, $\vec{I}$, and the total angular momentum, referred to as hyperfine splitting. The total angular momentum of the atom is then $\vec{F} = \vec{I} + \vec{J}$ and it is then convenient to further describe

the state by including F as a parameter in the notation. Using this notation, the ground state of ^{85}Rb is expressed as $5^2S_{1/2}$ F=2.

^{40}Ar in its ground state can also be described in the same notation as $3p^6(^1S_0)$. When considering the metastable states of Ar, however, a different notation may be more suitable since Russell-Saunders is a convenient notation for describing an atomic state when only the valence electron(s) contributes to the electron spin and angular momentum. In the process of becoming metastable, one of the core electrons in Ar is excited to the valence shell leaving an electron vacancy in the core. It is now important to include the core angular momentum as well as the valence electron angular momentum when describing the state. The notation commonly used for describing metastable states of a rare gas atom is referred to as jl coupling.

$$^{2S+1}L_j nl[K]_J \tag{2}$$

where L and S refer to the core angular momentum and spin, l and s refer to the angular momentum and spin of the valence electron, n is again the principle quantum number, $j = L + S$, $K = j + l$ and $J = K + s$ is the total angular momentum of the atom. Similarly to above, the energy levels are subject to fine structure splitting, but because ^{40}Ar is an even isotope, it has no residual nuclear spin and therefore there is no hyperfine splitting.

Diatomic molecules, like their atomic constituents, have energetic structure that is accessible through photonic interactions as well as through collisions and requires a comprehensive notation to label each state. For atoms, this was limited to the electronic state denoted by the principle quantum number n, with special regard given to the couplings between the angular momentum $\vec{L}$, the electronic spin $\vec{S}$, and the nuclear spin $\vec{F}$. For diatomic molecules, the need to label the electronic states of the constituent atoms is further expanded by the introduction of two additional degrees of freedom: vibrational and rotational. To first address the electronic states, these states can be addressed by a) their energetic order, b) symmetry properties of their molecular wave function, c) the angular momenta of the constituent atoms forming the molecular state and their projections along the internuclear axis, d) the vector sum of their electronic spins, and e) the atomic states to which the constituent atoms dissociate into as $R \to \infty$. Though in general, it may not be necessary to include all of these criteria, the molecular state cannot be sufficiently described by just one.

The electronic state of a diatomic molecule can be assigned in terms of the principle quantum numbers of the constituent atoms, however it may be misleading. For atomic notation, the assignment of the principle quantum number gives the energetic order of the states and this is not always the case for molecules. The commonly accepted molecular state notation developed with spectroscopic experiments which did label in energetic order. Here, the ground state is labeled the X-state and the next energetically higher state is labeled the A-state, then next the B-state, and so forth.

The symmetry properties of the electron wave function Ψ, refer to how the wave function transforms as it is acted on by the geometric operators for reflection and inversion. The reflection operator σ reflects the coordinates of the electron about the internuclear axis defined between the two nuclei. The wave function is labeled as positive ,Ψ^+, if $\hat{\sigma}\Psi = +\Psi$ and negative Ψ^-, if $\hat{\sigma}\Psi = -\Psi$. The inversion operator I defines the wave functions parity (where historically, even parity is labeled gerade and odd parity is ungerade) and is only applicable to diatomic molecules with indistinguishable nuclei. Here the wave function is labeled Ψ_g if $I\Psi(r) = +\Psi(-r)$ and Ψ_u if $I\Psi(r) = -\Psi(-r)$.

In an atom, the electron in its orbit has an orbital angular momentum l and intrinsic spin s. The case is also the same for molecules, however, the associated projections of l and s are now taken along the internuclear axis of the molecule. They are labeled $l_z = \lambda\hbar$ for orbital angular momentum (where $\lambda = |m_l|$) and $s_z = \sigma\hbar$ for spin. For a molecule with more than one electron, the values for L and S can be summed as $L = \sum l_i$ and $S = \sum s_i$ to give the total orbital and spin angular momenta with associated $L_z = \Lambda\hbar$ and $S_z = \Sigma\hbar$ projections on the internuclear axis. It is important to note that if the coupling between L and S is weak, then Λ and Σ are good, well defined quantum numbers. If the coupling between L and S is strong, then the projection of their vector sum, $J_z = \Omega\hbar$ where $J = L + S$, is a good quantum number, but Λ and Σ are no longer well defined. As $R \to \infty$ and the two atoms, A and B, of the molecule become dissociated, each atom has its own electron orbital angular momentum L_A and L_B (with projections M_{LA} and M_{LB}) and spin S_A and S_B. With the well defined values for M_L of each atom, the possible values of Λ for the molecule can be determined by $\Lambda = |M_{LA} + M_{LB}|$. States are assigned labels according to their value of Λ where $\Lambda = 0, 1, 2$ are called Σ-states, Π-states, and Δ-states respectively. An additional label denotes the multiplicity of the state by the value $(2S + 1)$. The molecular notation including fine structure labeling is

[35]

$$^{2S+1}\Lambda_{\Omega}, \quad \text{or} \quad ^{2S+1}\Lambda^{(+,-)}_{\Omega(g,u)} \tag{3}$$

if symmetry rules can be applied.

As previously stated, molecules have the two additional degrees of freedom, rotational and vibrational, which each have quantized energy levels associated with them. To address the rotational degree of freedom for a molecule, the assumption will be made that the distance between the nuclei will be fixed. The associated rotational kinetic energy is

$$E_{Rot} = \frac{I\omega^2}{2} \tag{4}$$

where I is the moment of inertia of the molecule. For a diatomic molecule, $I = MR^2$ with respect to the rotational axis where R is the internuclear separation of the rigid rotator and M is the reduced mass of the molecule. The system's angular momentum is $|J| = I\omega$. Equation 4 can now be expressed as

$$E_{Rot} = \frac{J^2}{2I} = \frac{J(J+1)\hbar^2}{2MR^2} \tag{5}$$

where $J^2 = J(J+1)\hbar^2$. Because the system can only take on integer values of J, the rotational energy spacings in a molecule can be estimated. This is the rotational energy spacing of the rigid rotator, but in fact the molecule is not rigid and there is a small correction to account for centrifugal distortion that will be neglected here.

To solve for the vibrational energy levels analytically, the assumption must be made that the molecular potential is harmonic. This assumption is of course far from the true form of the potential over all R, but over a certain region near the minimum in V of a deep potential, a harmonic potential can approximate the true potential fairly well. Being that the assumed potential is harmonic, the energy levels are simply that of the harmonic oscillator

$$E_{Vib} = (\nu + 1/2)\hbar\omega \tag{6}$$

where the oscillation frequency is determined by $\omega = \sqrt{k_r/M}$ and the energy levels are spaced equally since

$$\Delta E_{Vib} = E_{Vib}(\nu+1) - E_{Vib}(\nu) = \hbar\omega \tag{7}$$

This approximation works well within the vicinity of the minimum in V, but becomes increasingly inaccurate as the distance between the classical turning points of the oscillator increases and the true potential deviates from the harmonic approximation. Though the energy levels have equal spacings near the bottom of the near-harmonic potential, the energy levels become increasingly closer together as the energy approaches dissociation. To evaluate the vibrational energy levels of an arbitrary potential, the Schrödinger wave equation (SWE) needs to be solved for that potential. (i.e. a Morse potential that would typically approximate molecular potentials can only be solved numerically since there is no analytical solution for the SWE with this potential.)

II.2 RB AND AR

To simultaneously cool and confine Rb and Ar in the same region at ultracold temperatures requires a very unique apparatus, in part due to the differences between the two species. The forces responsible for cooling and trapping are discussed later in sections below. To efficiently be able to laser cool an atom, it must have a suitable electronic transition for scattering photons such that upon decay, the atom will return to the original state with high probability where then it can again scatter another photon of the same frequency as the first. This is refereed to as a cycling transition. Historically for this reason, alkali atoms such as Rb with a single valence electron have commonly been the species of choice to confine in a MOT, particulary because most alkalies have a cycling transition at a frequency easily attainable by modern laser sources. A good candidate cycling transition in ^{85}Rb, is the $5^2S_{1/2}$ F=3 to $5^2P_{3/2}$ F=4 transition, resonant with a photon of λ=780.242 nm.

Because the nearby $5^2P_{3/2}$ F=3 state is only $\sim$120 MHz away, the trapping laser will not only populate the $5^2P_{3/2}$ F=4 state, but can also populate the $5^2P_{3/2}$ F=3 state with a much smaller probability. When the $5^2P_{3/2}$ F=4 state relaxes, selection rules require that it will decay back to the $5^2S_{1/2}$ F=3 state where it can scatter another photon. When the $5^2P_{3/2}$ F=3 state relaxes, it may do so either to the $5^2S_{1/2}$ F=3 or F=2 state. If it has decayed to the F=2 state, the atom is no longer resonant with the trapping laser and is lost from the MOT. See Figure 1.

Though the probability of this is occurring is small, the millions of scattering events in the MOT make this a very significant trap loss mechanism. To recover these atoms back into the $5^2S_{1/2}$ F=3 state where they can continue to be trapped, a

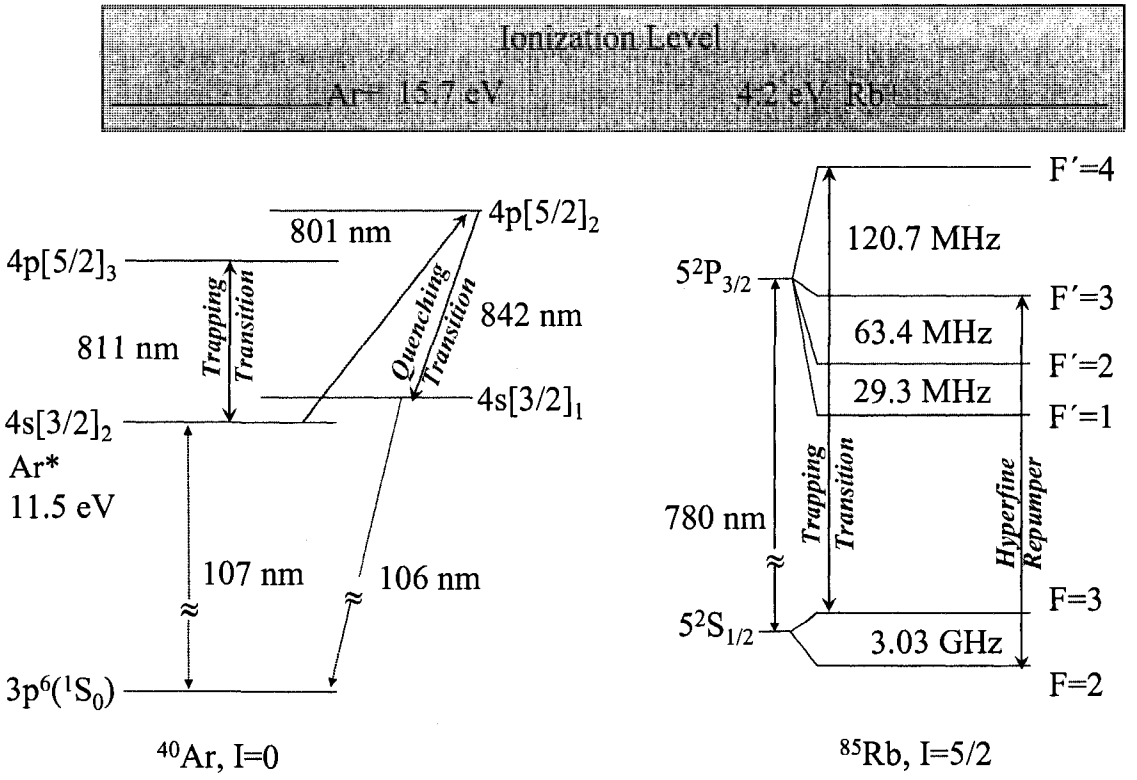

FIG. 1: Abbreviated energy level diagrams for ^{40}Ar and ^{85}Rb

second laser frequency is required. Referred to as the hyperfine repumper, this second laser is tuned to the $5^2S_{1/2}$ F=2 to $5^2P_{3/2}$ F=3 transition where upon decay the $5^2S_{1/2}$ F=3 state can be repopulated so trapping and cooling can continue. Conventionally, Rb and other alkalis have been loaded into a MOT from a low density thermal source background vapor where the tail-end of the Maxwell-Boltzmann distribution has a sufficient population density within the capture velocity for the MOT. This is the case for this apparatus as well.

For ^{40}Ar, the case is very different from Rb. All rare gases in the ground state have a closed valence shell. Consequently, to drive the transition from the $3p^6(^1S_0)$ ground state to the first excited state requires a UV photon. Ar, for example, would require a 107 nm photon, rendering the exploitation of that transition as the "cycling transition" for a MOT completely infeasible with today's cw laser sources. However, there is an alternative. All rare gases have metastable, or long lived excited states where a core electron is excited to the valence shell. These metastable states are electric-dipole forbidden to decay to the ground state and therefore have an excited

state lifetime on the order of tens of second compared to typical excited state lifetimes of ~30 ns. For metastable Ar, denoted Ar*, this lifetime is ~60 seconds which is more than ample time to cool and trap Ar* in this experiment. With a single electron now in the valence shell, the atom's electronic structure behaves similar to that of the alkalis. From these metastable states, there are a number of electric-dipole allowed transitions to other excited states that are resonant at wavelengths well within the range of cw lasers. For Ar in the $4s[3/2]_2$ metastable state, a transition to the $4p[5/2]_3$ requires an 811.54 nm photon and will only decay back to the $4s[3/2]_2$ metastable state. Therefore this transition can be used as a cycling transition for optically trapping and cooling and unlike for Rb, there is no hyperfine repumper needed for trapping Ar* since even isotopes have no nuclear spin to result in hyperfine splitting.

There are other transitions, as seen with the 801 nm transition in Ar from $4s[3/2]_2$ to $4p[5/2]_2$, that have a behavior unique to those atoms in metastable states. The $4p[5/2]_2$ state of Ar can decay to the $4s[3/2]_1$ state which is dipole allowed to decay back to $3p^6(^1S_0)$, the true ground state of Ar. This transition is referred to as a *quench* transition. Once in its true ground state, there are no efficient means to again excite the atom to its metastable state and the atom is lost from the MOT.

II.3 LIGHT FORCES ON AN ATOM

When a light field is incident on an atom, the atom may interact by scattering a photon of momentum $\hbar\vec{k}$. Upon absorption, the associated impulse is experienced by the atom as a force in the direction of the incident photon. After absorption, the spontaneous emission of a photon from the excited atom occurs in a random direction, where here the atom again experiences a momentum kick, or force, but in the direction opposite to the emitted photon. As this two-step absorption-emission process is repeated many times, the force experienced by the atom due to absorption of the photon will always be in the direction of the wave vector $\vec{k}$ of the light field, while the force resulting from the emission process will average to zero. This results in a net force in the direction of $\vec{k}$ and is referred to as the scattering light force or radiation pressure.

An atom in a light field can also interact with the light field through a different mechanism called the dipole force. This force arises from the interaction of the atom's electric dipole, induced by the oscillating electric field of the light field, with the magnitude of gradient of the time-averaged electric field.

Both the scattering and dipole light forces can be mathematically described in a semiclassical treatment of a light field interacting with a two-level atom [36]. The interaction Hamiltonian $\mathcal{H}$ for an atom in an electric field $\vec{E}(\vec{r},t)$ can be expressed as

$$\mathcal{H} = -\vec{\mu}_{eg} \cdot \vec{E}(\vec{r},t) \tag{8}$$

where $\vec{\mu}_{eg}$ is the transition dipole moment for the system. For an atom immersed in a light field, the force can be written as

$$\vec{F} = -\langle \vec{\nabla}_R \mathcal{H} \rangle = \vec{\nabla}_R \langle \vec{\mu}_{eg} \cdot \vec{E}(\vec{R},t) \rangle \tag{9}$$

where the spatial variation of the electric field is neglected. Using the Rabi frequency defined as

$$\Omega_{Rabi} = \frac{-eE_o}{\hbar}\langle e|r|g\rangle = -\frac{\vec{\mu}_{eg} \cdot \vec{E}_0}{\hbar} \tag{10}$$

and solving the optical Bloch equations for a two-level atom [36], the resulting force can be expressed as the sum of two forces.

$$\vec{F} = \vec{F}_{sp} + \vec{F}_{dip} \tag{11}$$

where

$$\vec{F}_{sp} = \vec{\nabla}_R(\vec{k} \cdot \vec{R})\frac{\hbar\Omega^2}{2}\left(\frac{\Gamma/2}{\delta^2 + (\Gamma/2)^2 + \Omega^2/2}\right) \tag{12}$$

and

$$\vec{F}_{dip} = -\vec{\nabla}_R|\vec{E}_0|\frac{\hbar\Omega^2}{2|\vec{E}_0|}\left(\frac{\delta}{\delta^2 + (\Gamma/2)^2 + \Omega^2/2}\right) \tag{13}$$

where Γ is the natural linewidth of the transition and δ is the relative detuning of the laser frequency from the transition frequency. These expressions can be rewritten in terms of the on-resonance saturation parameter

$$s_o = 2|\Omega|^2/\Gamma^2 = I/I_{sat} \tag{14}$$

to yield

$$\vec{F}_{sp} = \frac{\hbar\vec{k}s_o\Gamma/2}{1 + s_o + (2\delta/\Gamma)^2} \tag{15}$$

and

$$\vec{F}_{dip} = -\frac{\vec{\nabla} I}{2I} \frac{\hbar \delta s_o}{1 + s_o + (2\delta/\Gamma)^2} \tag{16}$$

where I is the light intensity.

The spontaneous light force, $\vec{F}_{sp}$, is the component of the total force resulting from the in phase interaction between Ω_{Rabi} and $\vec{E}(\vec{r}, t)$. The second term is the dipole light force and results from the out of phase interaction. The dipole light force, $\vec{F}_{dip}$, is a conservative force to first order, making it ideal for spatially confining cold atoms, but offers no means to actively cool or change the net momentum of an atom. $\vec{F}_{sp}$, on the other hand, is dissipative in nature and can be used to change the net momentum of the atom.

II.4 THE MAGNETO OPTICAL TRAP

First suggested by Pritchard in 1987, the spontaneous light force can be used to cool and trap neutral atoms by optically pumping a transition whereby the light field dissipates the atoms' momentum. Reducing an atom's momentum requires that the atom experiences a force in the opposite direction from it's velocity vector $\vec{v}$. As an atom with velocity $\vec{v} = 0$ and mass m, is immersed in a light field, the magnitude of $\vec{F}_{sp}$ maximizes when the laser field frequency ω_L, is resonant with the atomic transition frequency ω_A, and $\delta = \omega_A - \omega_L = 0$. For an atom moving with some non-zero component of velocity $\vec{v}$ parallel to $\vec{k}$, this is no longer the case since the Doppler shift, $\delta_D = -\vec{k} \cdot \vec{v}$, has shifted the frequency of the light field experienced by the atom. Substituting $\delta \rightarrow \delta_{Eff} = \omega_A - \omega_L - \delta_D$, and the spontaneous light force now reads

$$\vec{F}_{sp} = \frac{\hbar \vec{k} s_o \frac{\Gamma}{2}}{1 + s_o + (\frac{2(\omega_A - \omega_L - \delta_D)}{\Gamma})^2} \tag{17}$$

This expression is now maximized when $\omega_L = \omega_A - \delta_D$. One way to look at this result is that a laser tuned to $\omega_L = \omega_A$ is only resonant to atoms near the velocity class $\vec{v} = 0$. Alternatively, this expression shows that by choosing the proper laser detuning, F_{sp} maximizes around a particular velocity class of atoms where

$$\omega_L = \omega_A - \delta_D = \omega_A + \vec{k} \cdot \vec{v} \tag{18}$$

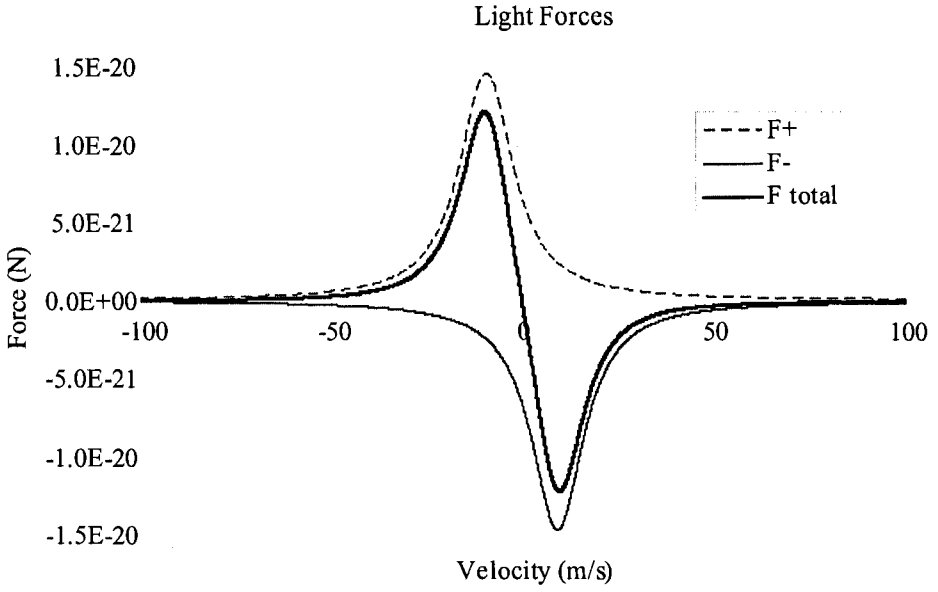

FIG. 2: Plot of F_{sp} for an atom with velocity v, in a laser field red detuned of the atomic line. The figure shows the forces for light incident from the left, $\vec{F}_+$, from the right, $\vec{F}_-$, and the forces felt in a 1-D optical molasses.

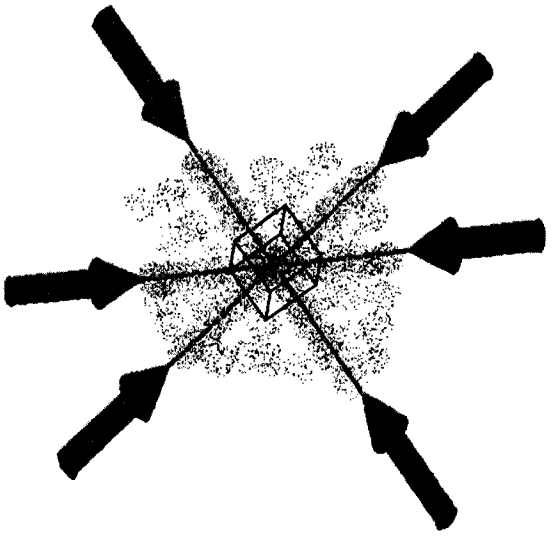

FIG. 3: Optical Molasses: Three sets of perpendicular laser beams red detuned from the atomic resonance

as illustrated in Figure 2.

To cool, or slow, atoms, F_{sp} should be maximized for atoms with $\vec{v}$ in the opposite direction to $\vec{k}$ requiring for the laser that $\omega_L < \omega_A$ or to be red detuned of the atomic transition. Since the laser can only slow atoms that are moving anti-parallel to the beam, to slow atoms with velocities of an arbitrary direction, six lasers beams are arranged such that they intersect a common volume as described in Figure 3. Referred to as optical molasses, this configuration plays a vital role in the operation of the magneto-optical trap (MOT).

Though optical molasses can cool atoms by using the velocity selective spontaneous light force, it is not a position dependent force and therefore cannot spatially confine the atoms. For this, the atomic structure of the atom being trapped needs to be considered. For the simple system that drives a $J_g = 0 \rightarrow J_e = 1$ transition, the excited state has three magnetic sub-levels $M_J = 1, 0, -1$. If no magnetic field is present ($B = 0$), these levels are degenerate and will be each excited with equal probability. However, if a magnetic field is applied, the Zeeman effect will lift the degeneracy by shifting the energy levels by $\delta_Z = g\mu_B(\vec{J} \cdot \vec{B})/\hbar = \mu_B M_J B/\hbar$ where $\vec{J}$ and M_J are the total angular momentum and its projection along the z-axis,

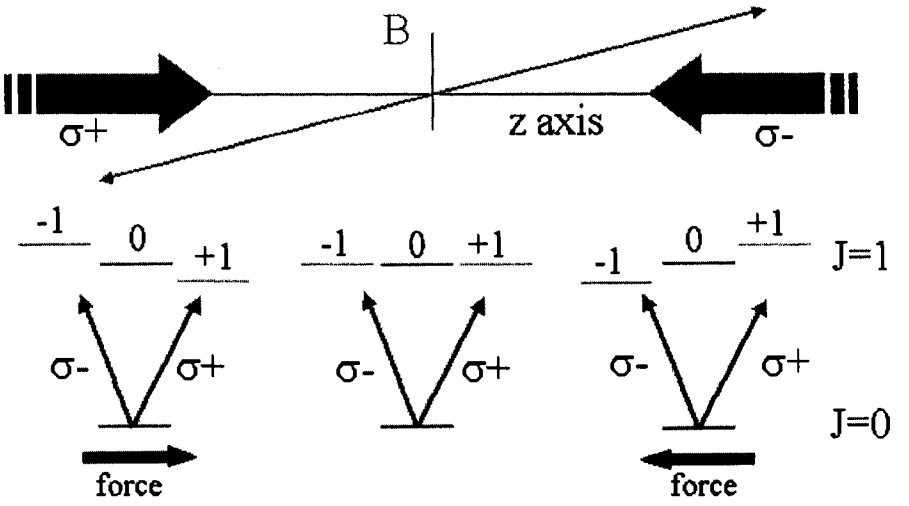

FIG. 4: The application of a magnetic field gradient lifts the degeneracy of the upper state, giving a spatial dependence to the scattering light force F_{sp}, shown here for a $J = 0 \rightarrow J' = 1$ transition.

$\mu_B = e\hbar/2m_e c$ is the Bohr magneton, and g is the Landé g-factor. If a spatially linearly increasing magnetic field $B(z)$ is applied, the magnitude of δ_Z becomes spatially varying.

Consider, in one dimension, a region where $B(z)$ can have negative or positive values. The sign of δ_Z is dependent on the sign of both B and M_J, therefore on the left side of Figure 4, where B is negative, the magnetic sublevels $M_J = -1, 0, +1$ will split such that $M_J = -1$ will be higher in energy than the $M_J = +1$ with an energy separation proportional to B. As the magnitude of B decreases to zero, the sublevels become degenerate. As B becomes positive, again the sublevels split, but with the opposite sign. If red detuned, σ^- polarized light is applied from right to left, it is clear that the atoms to the right of center have the highest probability of scattering light since they are closest to resonance with the laser beam. (Note that σ^- drives the transition to the $M_J = -1$ state). This higher probability to scatter photons results in a force on these atoms towards the left. Similarly, σ^+ red detuned light coming from the left will result in atoms on the left of the minimum in $|B(z)|$ to experience a force towards the right. In both cases, the atoms are pushed toward the minimum in $|B(z)|$, constituting a one-dimensional trap. Fortunately, this concept

can easily be applied to other transitions where $J_g \rightarrow J_e = J_g + 1$, since few elements have a simple $J_g = 0 \rightarrow J_e = 1$ transition. The force, in the z direction, is now described by the spatially dependent expression

$$\vec{F}_{\pm} = \pm \frac{\hbar \vec{k} s_o \frac{\Gamma}{2}}{1 + s_o + (\frac{2\delta_{\pm}}{\Gamma})^2} \tag{19}$$

where

$$\delta_{\pm} = \omega_A - \omega_L \mp \vec{k} \cdot \vec{v} \pm \mu' B(z)/\hbar \tag{20}$$

To construct the trap in three dimensions, three pairs of perpendicularly intersecting laser beams of appropriate polarization and detuning are placed in the inhomogeneous magnetic field of anti-Helmholtz coils, such that there is a minimum in $|B(z)|$ in the center of the trapping volume. This configuration is called the magneto-optical trap (MOT).

The behavior of an atom in a MOT can be described by considering Equation 19. When the detuning of the laser from resonance, δ, is large when compared with the Doppler and Zeeman shifts, Equation 19 can be expanded and expressed as a damped harmonic oscillator of the form

$$\vec{F} \sim -\beta \vec{v} - \kappa \vec{r} \tag{21}$$

where $\beta = \kappa \hbar k/(A\mu')$ and A is the gradient of the magnetic field B. In Figure 5, the motion of an atom in the trap has been modeled by numerically solving Equation 19.

II.5 COOING LIMITS AND SUB-DOPPLER COOLING

As discussed in the previous section, the spontaneous or scattering light force cools atoms via the process of photon absorption and emission. The nature of the emission process leads to fluctuations in the scattering force due to the recoil kick from the emitted photon leading to a heating mechanism. Knowing the recoil kick the atom experiences due to the photon emission/absoroption is $\hbar\vec{k}$, an expression for this heating can be obtained. The photon scattering rate is defined as

$$\gamma = \frac{s_o \Gamma/2}{1 + s_o + (\frac{2\delta}{\Gamma})^2} \tag{22}$$

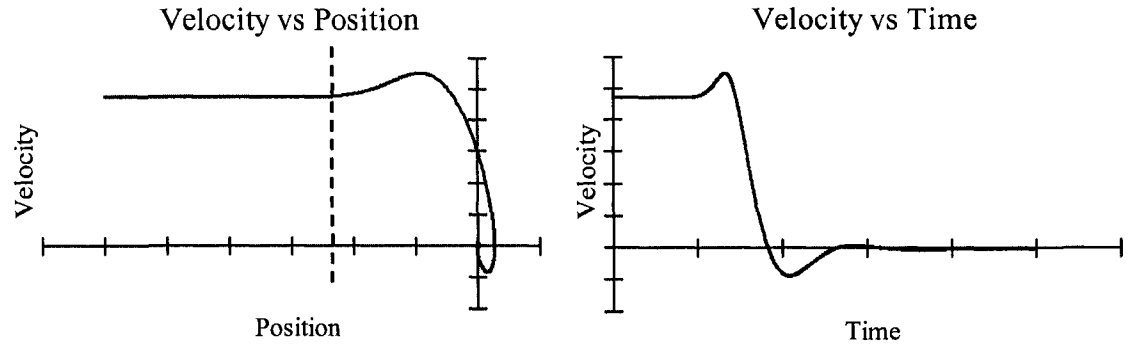

FIG. 5: Simple model of how an atom behaves in a MOT. The dashed lines represent where the trapping volume begins.

where for small s_o, $\gamma \approx s_o\Gamma$. The heating mechanism due to the random direction of the photon emission can be written as

$$\frac{\partial}{\partial t}\langle p^2\rangle = 2s_o\Gamma(\hbar k)^2 \tag{23}$$

and the rate of change of the energy is

$$\frac{\partial}{\partial t}E_{Heat} = \frac{s_o\Gamma(\hbar k)^2}{M} \tag{24}$$

where $E = k_BT/2 = \langle p^2\rangle/2M$ is the thermal energy of the system.

To determine a cooling limit for the scattering light force, the system can be considered in a steady state where the cooling force is balanced by the heating mechanism. Derived from Equation 17 in the limiting case where $s_o \ll 1$,

$$\frac{\partial}{\partial t}E_{Cool} \approx -2\hbar s_o(kv)^2 \tag{25}$$

Equating these two expressions for competing processes gives

$$\frac{k_BT_D}{2} = \frac{\hbar\Gamma}{4} \tag{26}$$

where T_D is referred to as the Doppler temperature. This limit is reached for the optimal laser detuning of $\delta = -\Gamma/2$ and corresponds to temperatures of $\sim 140\mu K$ and $\sim 130\mu K$ for ^{85}Rb and ^{40}Ar*, respectively.

Though the Doppler temperature is the cooling limit for the scattering light force, it was quickly discovered that the temperatures in an optical molasses could be well below the Doppler temperature, suggesting that other cooling mechanisms are at work. For the treatment of the scattering light force a two-level atom was assumed. For many atoms, however, there exist hyperfine levels and Zeeman sub-levels with small energy differences as to be close enough to not be ignored. In fact it is the existence of these multi-level atoms that lead the way into sub-doppler cooling mechanisms such as polarization gradient cooling.

II.6 THE DIPOLE FORCE TRAP

While the magneto optical trap with its optical molasses has the ability to cool and spatially confine atoms, it is also quite limited in the maximum density attainable due to excited state collisions, (discussed in the following sections), and radiation trapping where scattered photons re-scatter off another atom in the trap. Both of these density limiting factors come about because the force responsible for the trapping and cooling, F_{sp}, relies on a near-resonant optical field. While there are some *tricks* to getting increased densities in MOTs, such as Dark Spot MOTs, the spontaneous light force can only achieve so much.

Alternatively, the dipole light force

$$\vec{F}_{dip} = -\frac{\vec{\nabla} I}{2I} \frac{\hbar \delta s_o}{1 + s_o + (2\delta/\Gamma)^2} \tag{27}$$

does not rely on scattering resonant photons to achieve spatial confinement, but rather can use far-off resonant light and is dependent on the magnitude of the electric field gradient produced by the laser field. Being able to operate far from an atomic resonance allows for a very small excited state population, greatly reducing the number of excited state collisions and radiation trapping, and allowing for a much higher obtainable density.

One of the simplest traps comes about by creating a strong electric field gradient by tightly focusing a laser beam with a TEM00 Gaussian profile such that the intensity varies spatially with r as

$$I(r) = I_o e^{-r^2/\omega_o^2} \tag{28}$$

where I is the intensity of the electric field, ω_o is the Gaussian waist at the focus, and r is the transverse distance from the center of the focus. When the laser in tuned red

of resonance, the ground state atoms in the light field experience a light shift which is largest at the center of the focus where the light is most intense. This results in the atoms experiencing a force towards higher intensities that can be expressed

$$\vec{F}_{dip} \approx -\frac{\hbar\gamma^2}{8\delta I}\nabla I(r) \tag{29}$$

and by taking the gradient of Equation 28 and making a substitution

$$\vec{F}_{dip} \approx -\frac{\hbar\gamma^2}{4\delta}\frac{I_o}{I}\frac{r}{\omega_o^2}e^{-r^2/\omega_o^2} \tag{30}$$

which is harmonic for the Gaussian waist at the focus. This expression describes the transverse dipole force, but a similar argument is valid in the longitudinal direction as well, resulting in a spatially confining force in three dimensions. A dipole force trap is conservative to first order, which results in the lack in ability to optically cool the atoms in the trap. This means that the atoms to be loaded into the trap need to be cold prior to loading. For this reason, atoms are typically cooled in a MOT and carefully loaded into the dipole trap. Dipole force traps can confine atoms at densities of $\sim 10^{12}$ atoms/cm^3, two to three orders of magnitude higher than those found in MOTs, and at temperatures of $100\mu K$.

In application to photoassociative spectroscopy, dipole traps have been used to gain density of alkali samples to increase PA signal to noise when probed with a PA beam. Unfortunately, when trying to apply the same technique to PA of metastable rare gases, the increased sample density would result in an increased rate in ionizing collisions due to the significant internal energy of the metastable atom. One alternative experiment could be to have a MOT of Ar*, quench the MOT to the true ground state, and load Ar ground state atoms into a dipole trap where they can be investigated spectroscopically.

II.7 ULTRACOLD COLLISIONS

Collisions play an important role in a MOT and, along with light pressure, are responsible for limiting its size and density. They can arise from collisions between cold trapped atoms and thermal background atoms, where the kinetic energy of a hot atom is transferred to a cold atom and both atoms have a temperature above the capture temperature for the MOT, resulting in trap loss. There are also collisions between ultracold trapped atoms, which may be elastic or inelastic and arise

through a number of different mechanisms. Both of these types of collisions greatly affect the behavior of the atom loading rate of the MOT including the MOT loading time, maximum MOT size, volume and density. The physics of understanding these collision processes will be briefly detailed here.

II.7.1 Ground State Collisions

The interaction between two colliding, structureless particles can be described by solving the time-independent Schrödinger wave equation (SWE) for the system where the interaction potential between the two particles is $V(R)$ and R is the distance between the particles. In spherical coordinates the SWE becomes

$$\left\{-\frac{\hbar^2}{2\mu R^2}\frac{d}{dR}\left(R^2\frac{d}{dR}\right)+\frac{\hbar^2 l(l+1)}{2\mu R^2}+V(R)\right\}\Psi_k(R)=E\Psi_k(R) \tag{31}$$

where μ is the reduced mass of the system, $E=\hbar^2k^2/2\mu$ is the particle energy and $\hbar^2 l(l+1)/(2\mu R^2)$ is the centrifugal energy term for a partial wave l. At distances on the order of a few a_0, the potential energy of $V(R)$ is fairly appreciable and the solutions to the SWE are complicated but can be expressed as a partial wave series expansion in terms of Legendre polynomials $P_l(\cos\theta)$ as

$$\Psi_k(R)=\sum_{l=0}^{\infty}A_l(k,R)P_l(\cos\theta) \tag{32}$$

where $A_l(k,R)$ are coefficients for each l. At larger internuclear distances the magnitude of $V(R)$ is not as appreciable and the solutions to the SWE begin to trend to simple oscillatory functions. As $R\rightarrow\infty$, the solutions are identical to the solutions of the SWE if $V(R)=0$ with the exception of a phase shift δ_l. The total scattering cross section can then be written in terms of this phase shift and partial wave number as

$$\sigma=\frac{4\pi}{k^2}\sum_{l=0}^{\infty}(2l+1)\sin^2\delta_l \tag{33}$$

This expression can be further simplified by considering the centrifugal energy term in the Hamiltonian of Equation 31. If the particle energy E is less than the centrifugal energy term, the particle can not penetrate to small enough R where the potential $V(R)$ becomes appreciably large. The effective potential becomes essentially zero and the phase shift δ_l goes to zero as well. In short, given the particle's

energy, the centrifugal energy term determines what partial waves can contribute to the collision (this does not apply to ionic molecules). For the ground state trapped atoms found in a typical MOT, the centrifugal energy term for partial waves $l \geq 1$ is already larger than the particles energy which is $E \sim \hbar\gamma/2$, restricting to only $l = 0$ partial wave scattering, also called s-wave scattering. The collisions of this nature are typically characterized by the s-wave scattering length a where

$$a = -\lim_{k \to 0} \frac{\delta_{l=0}}{k} \tag{34}$$

II.7.2 Excited State Collisions

In a MOT at any given time when the trapping lasers are on, driving the trapping transition, $\sim 30\%$ of the trapped atoms are in the excited state and this changes the collision dynamics. Two atoms in the ground state will experience a van der Waals potential where the leading coefficient of a multipole expansion of the potential is the C_6/R^6 term. If one of the atoms is in an excited state, the leading coefficient of the potential is the dipole-dipole C_3/R^3 term (and C_5/R^5 quadrupole-quadrupole if both are in the excited state). Collisions that take place between two ground state atoms can only be an elastic collision, where both atoms leave the collision in exactly the same state as they started, or a hyperfine-structure changing collision (HCC) where the F quantum number changes. (Here elastic collisions are vital to the production of Bose-Einstein Condensates (BEC) since they are responsible for re-thermalization of the trapped atoms via momentum transfer which makes evaporative cooling possible.) On the other hand, excited state collisions can lead to fine-structure changing collisions (FCC), radiative escape (RE) or, in some cases, ionization of the atom(s), all of which contribute to increased trap loss.

An excited state collision between two atoms can be described in the following way, visually aided by Figure 6. Two, homonuclear, unbound, ground state atoms at internuclear distance R experience a potential dominated by a weak van der Waals interaction. The pair of atoms absorbs a photon, $\hbar\omega$, and now experience an excited molecular potential which is dominated by a dipole-dipole interaction. With the atoms now experiencing a larger potential gradient, they begin to accelerate towards each other. Because of the low temperature of the atomic sample, the collision occurs over a period of time much longer than a typical atomic excited state lifetime τ and the quasi-molecule has a certain probability to relax by emitting a photon $\hbar\omega'$ back

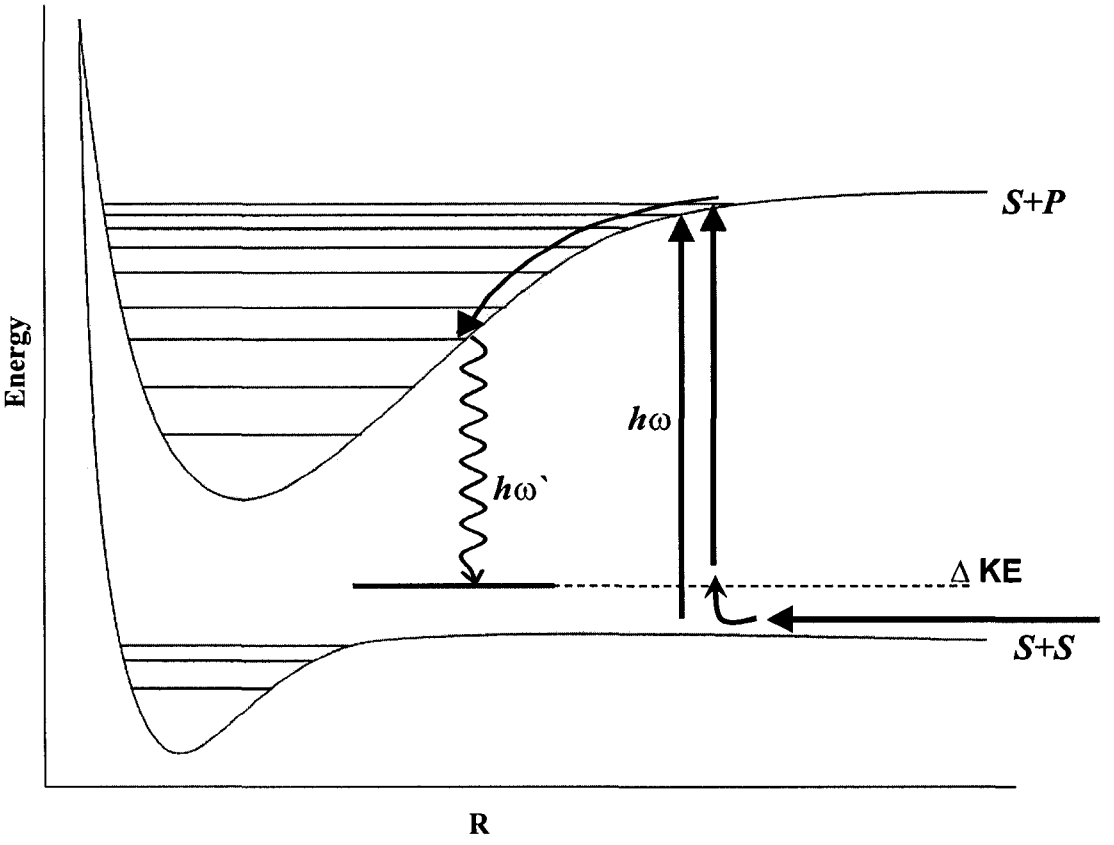

FIG. 6: Schematic of an excited state collision resulting in radiative escape. Two atoms approaching on a ground state potential are excited and gain relative kinetic energy as they travel along the upper potential. If they spontaneously relax by photon emission before reaching small internuclear distance, the kinetic energy they picked up may eject them from the trap.

to the original ground state before reaching small R. Depending on where this event occurs, the atoms can pick up enough kinetic energy while on the excited molecular potential to escape the MOT after relaxation. This is known as radiative escape and is described by

$$Rb + Rb + \hbar\omega \rightarrow Rb_2^* \rightarrow Rb + Rb + \hbar\omega' + \Delta KE \tag{35}$$

where if $\Delta KE = \hbar\omega - \hbar\omega'$ exceeds the trap depth, the atoms escape the MOT.

If the atom pair remain on the exited molecular potential long enough to reach small R (small R being inwards of a few a_0 from the potential minimum) the atoms are considered to be in the region where FCC and ionization can take place if energetically allowed. At large R, the molecular potential approaches an asymptote largely governed by atomic fine structure. In a semiclassical analysis, at small R, electron cloud overlap dominates the behavior resulting in various crossings of potential curves for different molecular states. To a good approximation, at these crossings the atom pair can cross from one potential to the other with a probability denoted by the Landau-Zener single-transit curve crossing probability given by

$$P_{LZ} = 1 - e^{-\pi\Lambda} \tag{36}$$

with

$$\Lambda = \frac{\hbar\Omega^2}{2\alpha v_C} \tag{37}$$

where Ω, the Rabi frequency, is the coupling between the two potentials, α and v_C are the gradient of the potential and atom velocity, respectively at the Condon point. If two atoms undergo a collision which begins on the $5^2S_{1/2} + 5^2P_{3/2}$ molecular potential and as they approach small R there is a curve crossing with the $5^2S_{1/2} + 5^2P_{1/2}$ potential, depending on the Landau-Zener single-transit curve crossing probability, the atom pair may cross and exit on the $5^2S_{1/2} + 5^2P_{1/2}$ potential where the difference in energy is compensated by an increase in nuclear kinetic energy. This is known as a fine-structure changing collision (FCC), described by

$$5^2S_{1/2} + 5^2P_{3/2} \rightarrow 5^2S_{1/2} + 5^2P_{1/2} + \Delta KE \tag{38}$$

and is also a large contributing factor to trap loss in alkali MOTs.

In the case of Ar* (and other metastable rare gases and Na), this process can have a very different outcome resulting in ionization. Though the final products

for Na and Ar* collisions are both ions, the mechanism responsible for this is very different for each. In Na, the mechanism in very similar to the Landau-Zener picture responsible for FCC and radiative escape. As reported in [37], the minimum in the Na_2^+ molecular ion potential well has an energy lower than that of the asymptotic energy for Na_2 $P_{3/2}$+$P_{3/2}$ potential. In an Na MOT where trapping is conducted using the 589 nm $S_{1/2}$ to $P_{3/2}$ transition, collisions occurring between two excited Na atoms have near unity probability of ionization.

The picture for the ionization mechanism for Ar*, and other metastable rare gases, differs from that of Na. In the metastable state, Ar* contains ~11.5 eV of energy, ~4.2 eV below its ~15.7 eV ionization potential. Consequently, the asymptote of the Ar*+Ar* potential lies well above the Ar^++Ar potential, making it energetically favorable to ionize. Depicted in Figure 7, as two Ar* atoms approach along the potential, at some small internuclear distance they auto-ionize via a Frank-Condon like transition where the ejected electron, instead of a photon, carries away most of the energy as KE leaving the Ar^+ or Ar_2^+ product. Though both this mechanisms and that of Na both result in ionization, the driving mechanisms are quite different.

$$4s[3/2]_2 + 4p[5/2]_2 \rightarrow Ar_2^+ + e \rightarrow Ar + Ar^+ + e \tag{39}$$

As just described, some trap loss in a MOT occurs through the formation of quasi-molecules that readily interact through various channels, usually resulting in two free atoms. It is also possible that stable, bound cold molecules can be produced. If, for example, two Rb atoms interact on the $5^2S_{1/2}$ + $5^2P_{3/2}$ potential, if they do not undergo FCC or RE, at a certain R the quasi-molecule can relax by photon emission to a bound molecular state on the $5^2S_{1/2}$ + $5^2S_{1/2}$ potential. Because the bound molecule is no longer resonant with the trapping laser, it too is a source of trap loss for the MOT.

II.7.3 Trap Loss in a MOT

The number of atoms in the MOT at any time is in large part determined by the collision rate between trapped atoms and that of collisions between the thermal background vapor and the trapped atoms. These losses can be quantified by observing the transient loading, or decay, curves of the number of trapped atoms as a function of time and fitting to a mathematical model for the atom load rate. The rate of

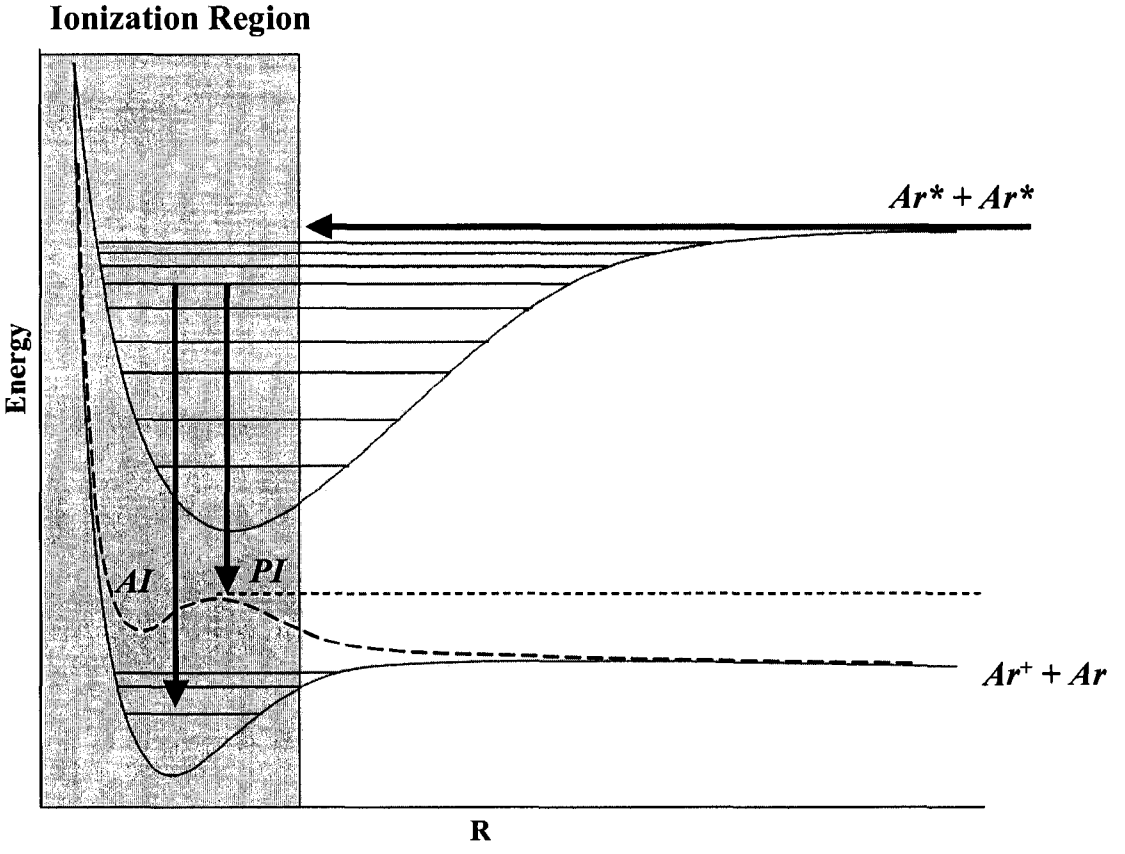

FIG. 7: Schematic showing Penning (PI) and associative (AI) ionization channels for metastable Argon

change of the number of atoms in the MOT, $N(t)$, can be mathematically described by the differential equation

$$\frac{dN_{Rb}(t)}{dt} = L - \gamma N_{Rb}(t) - \beta_{Rb} \int_v n(r,t)^2_{Rb} d^3r \tag{40}$$

where L is the atom capture rate, γ is the loss rate coefficient due to background vapor collisions, and β is trap loss coefficient between trapped atoms in the MOT with the integral taken over the volume of the MOT, V. The density function, $n(r,t)$ is assumed to be Gaussian and of the form

$$n(r,t) = n_0(t) e^{-2(r/\omega(t))^2} \tag{41}$$

where n_0 is the maximum atom density, ω is the waist of the MOT, and r is the position from the center of the MOT. Here, the assumption that the MOT is of a Gaussian density distribution is valid since the experiment is run in the region of low trap light intensity where the MOT forms with a constant volume. This is verified later by florescence imaging of the MOT. At higher trap light intensities, radiation trapping begins to play a role in limiting the maximum density, which creates a flat-top density distribution, requiring a different form for $n(r,t)$. After integration, Equation 40 becomes

$$\frac{dN_{Rb}(t)}{dt} = L - \gamma N_{Rb}(t) - \frac{\beta_{Rb} N_{Rb}(t)^2}{\omega^3_{Rb} \pi^{3/2}} \tag{42}$$

Imposing the initial condition of $N(t=0) = 0$, this differential equation has the analytical solution of

$$N(t) = N_0 \left[1 - \frac{(1+\xi)\exp(-t/\tau_L)}{1+\xi\exp(-t/\tau_L)} \right] \tag{43}$$

where

$$\tau_L = \frac{1-\xi}{\gamma(1+\xi)} \tag{44}$$

and

$$\xi = \left(1 + \sqrt{8} \frac{\gamma}{\beta n_0} \right)^{-1} \tag{45}$$

The time evolution of $N(t)$ can be directly measured experimentally through fluorescence detection from the MOT. By fitting Equation 43, the coefficients γ and β can be extracted for a homonuclear system.

By constructing a MOT where two species can be simultaneously loaded in the same spatial region, heteronuclear collisions may also be investigated as is done in this experiment for Ar* and Rb. First consider the load rate equation for the number of trapped Rb atoms in the presence of an Ar* MOT. The rate equation for the Rb MOT loading is now modified due to the additional loss term associated with the presence of Ar* MOT and is expressed

$$\frac{dN_{Rb}}{dt} = L - \gamma N_{Rb}(t) - \beta_{Rb}\int_v n_{Rb}^2 d^3r - \beta'_{Rb-Ar*}\int_v n_{Rb}n_{Ar*}d^3r \tag{46}$$

where β'_{Rb-Ar*} is the trap coefficient for Rb in the presence of Ar* and the integral is taken over the volume of the MOT which assumes a perfect overlap between the Gaussian density distributions for both MOTs, n_{Rb} and n_{Ar*}. Upon integration, the expression becomes

$$\frac{dN_{Rb}(t)}{dt} = L - \gamma N_{Rb}(t) - \frac{\beta_{Rb}N_{Rb}(t)^2}{\omega_{Rb}^3\pi^{3/2}} - \beta'_{Rb-Ar*}N_{Rb}(t)N_{Ar*}(t)\left[\frac{2}{(\omega_{Rb}^2+\omega_{Ar*}^2)\pi}\right]^{3/2} \tag{47}$$

The expression for the reciprocal relationship of Ar* in the presence of Rb is of similar form here

$$\frac{dN_{Ar*}(t)}{dt} = L - \gamma N_{Ar*}(t) - \frac{\beta_{Ar*}N_{Ar*}(t)^2}{\omega_{Ar*}^3\pi^{3/2}} - \beta'_{Ar*-Rb}N_{Ar*}(t)N_{Rb}(t)\left[\frac{2}{(\omega_{Ar*}^2+\omega_{Rb}^2)\pi}\right]^{3/2} \tag{48}$$

These relationships will be discussed further in chapter IV.

II.8 PHOTOASSOCIATIVE SPECTROSCOPY

As two free atoms undergo a collision in a light field, if the atom pair absorbs a photon and is excited to a bound excited molecular state, it has undergone photoassociation. Though similar in some aspects to the process of radiative escape, photoassociation is distinctly different in that the absorption of a photon $\hbar\omega$ drives a free-bound transition into one of the ro-vibrational levels of the excited molecular potential as in Figure 8. Once the atoms are in the excited molecular potential, there are a number of channels for the atoms to exit. Since the molecular state is excited, the molecule

can relax by photon emission. Depending on the internuclear distance R at which this occurs, the atoms can relax to their original dissociated states. This process can also lead to radiative escape where the atoms pick up appreciable kinetic energy before decaying back to the ground state. Alternatively, if the molecule relaxes at small R, there is a probability that the quasi-molecule relaxes into a stable, bound, ground state molecule. Additionally, in the case of metastable rare gases such as Ar*, when energetically favorable there is the possibility that at small internuclear distance, the bound excited state molecule experiences a Frank-Condon like transition to the molecular ion potential resulting in either Penning or associative ionization. In the case of an Ar_2^* molecule, this is the dominant mechanism. The chances of photoassociation taking place and exiting through a certain channel are governed by transition/interaction probabilities determined through quantum mechanics and are largely dependent on the radial part of the Schrödinger wave equation and the angular momentum of the incoming and outgoing states.

Though, for decades, photoassociation has been known to occur in thermal samples of atoms, Doppler and pressure broadening of the accessible levels in these samples are orders of magnitude larger than the energetic spacings between the bound states. Spectroscopy of this system will yield little information about the molecular structure or potentials because the photoassociative resonances grossly overlap due to this broadening and the excitation to individual levels can not be resolved. Now, with the availability of ultracold atomic samples, the photoassociation of atoms can be spectroscopically investigated with much detail and spectral resolution.

By tuning the frequency of the PA laser, $\hbar\omega_{PA}$, the colliding ground state atoms can be photoassociated into different ro-vibrational excited molecular potentials as the laser comes into resonance with the energy difference between the free, ground state atoms and the excited ro-vibrational level. Most photoassociative spectroscopy experiments conducted in ultracold atomic samples observe a photoassociation resonance as an increase in trap loss in the MOT as the PA laser is scanned over the transition. With the measurement generally done by MOT fluorescence detection, this method is very effective for states with strong transition probabilities and an intense PA laser source. If the transition strength is weak, however, the small amount of trap loss in the MOT will result in a low signal to noise ratio where peak detection and assignments can become difficult or impossible. The low densities typically found in MOTs can result in low signal to noise. To increase the density of the

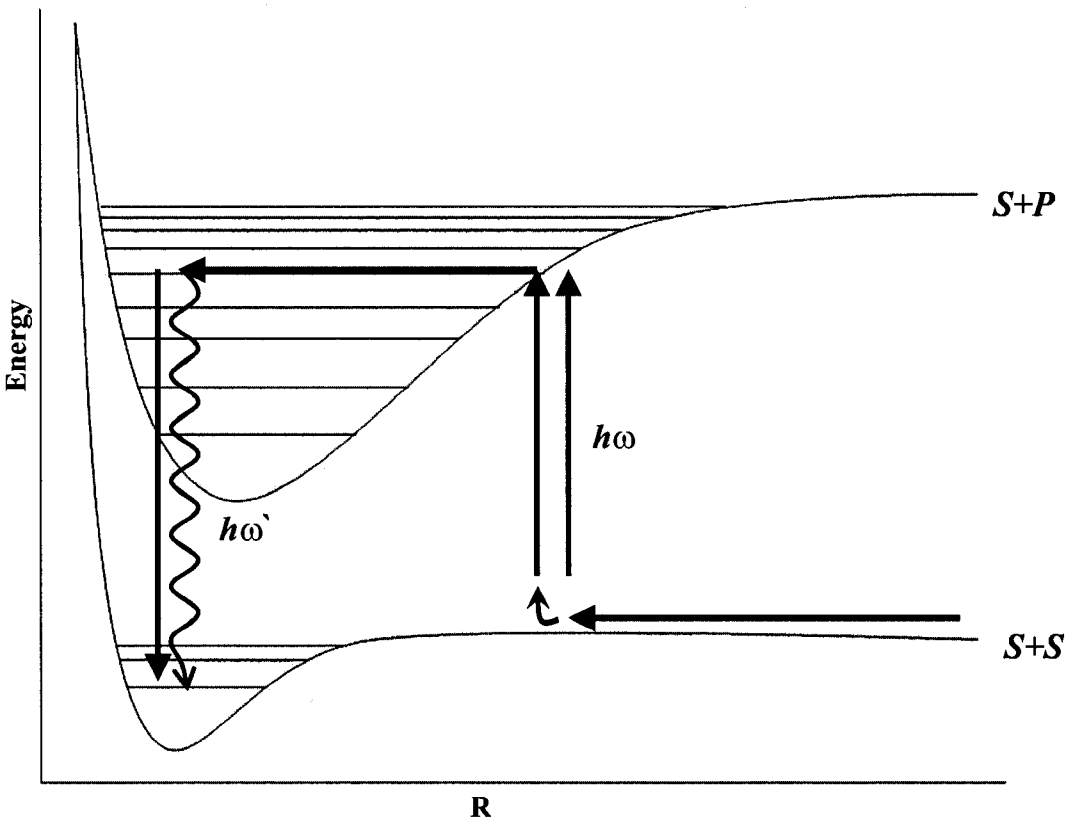

FIG. 8: Schematic of two atoms undergoing photoassociation followed by molecule formation.

atomic sample for PAS, for alkalis a common tool is the dark-spot MOT, where the density limiting radiation pressure is reduced by pumping atoms into a different hyperfine state where they are no longer resonant with the trapping light [38]. Using this method, densities can improve from $10^{10}/\text{cm}^3$ for a conventional MOT to $10^{12}/\text{cm}^3$ for a dark-spot MOT. Unfortunately, this method requires that the atoms being trapped have a non-zero nuclear spin for hyperfine splitting. As an alternative method to detecting trap loss, if the event of two atoms undergoing photoassociation results in the production of an ion, the signal to noise ratio can be improved by detecting these ions instead of depending on a fluorescence measurement.

Although the Ar* MOT naturally produces ~10 kHz of Ar^+ and Ar_2^+ ions due to excited state collisions driven by the trapping laser, this method is still most favorable. The ions produced by the MOT when the trapping lasers are on, serve as a large background. However, by briefly turning off the trapping light, the MOT relaxes to the ground state where ionization rates are 100-1000 times less, ~10 Hz. Probing the ground state MOT during this period ensures that any transitions made are one color, $\hbar\omega_{PA}$, and the ions are detected with good signal to noise. It should be noted that ensuring that only single-color transitions occur does not eliminate the possibility of two photon transitions as seen in Na [39].

In application to other species that may not auto-ionize, ion detection can also be used to observe a photoassociative resonance by using the method of direct ionization [40]. Depicted in Figure 9, this can be accomplished by having an additional laser whose frequency needs to be chosen such that it is not resonant with any atomic or molecular resonances, but will excite the photoassociated molecule into the molecular ion continuum. In this fashion, the photoassociated molecule will be ionized and can be detected with near infinite signal to noise since there is little residual ion background.

By scanning the PA laser over a range of frequencies near an atomic resonance and recording the rate of ion production (or trap loss) as a function of the PA laser frequency, a photoassociative spectrum can be obtained. By measuring the spacings between the observed peaks and knowing the peaks relative position to the dissociation limit, peaks can be grouped into series and assigned. Having an understanding of the molecular states and structures greatly aids in the assignment of peaks to a particular series for a state, but the spectra can become complicated and making proper assignments is not a trivial task.

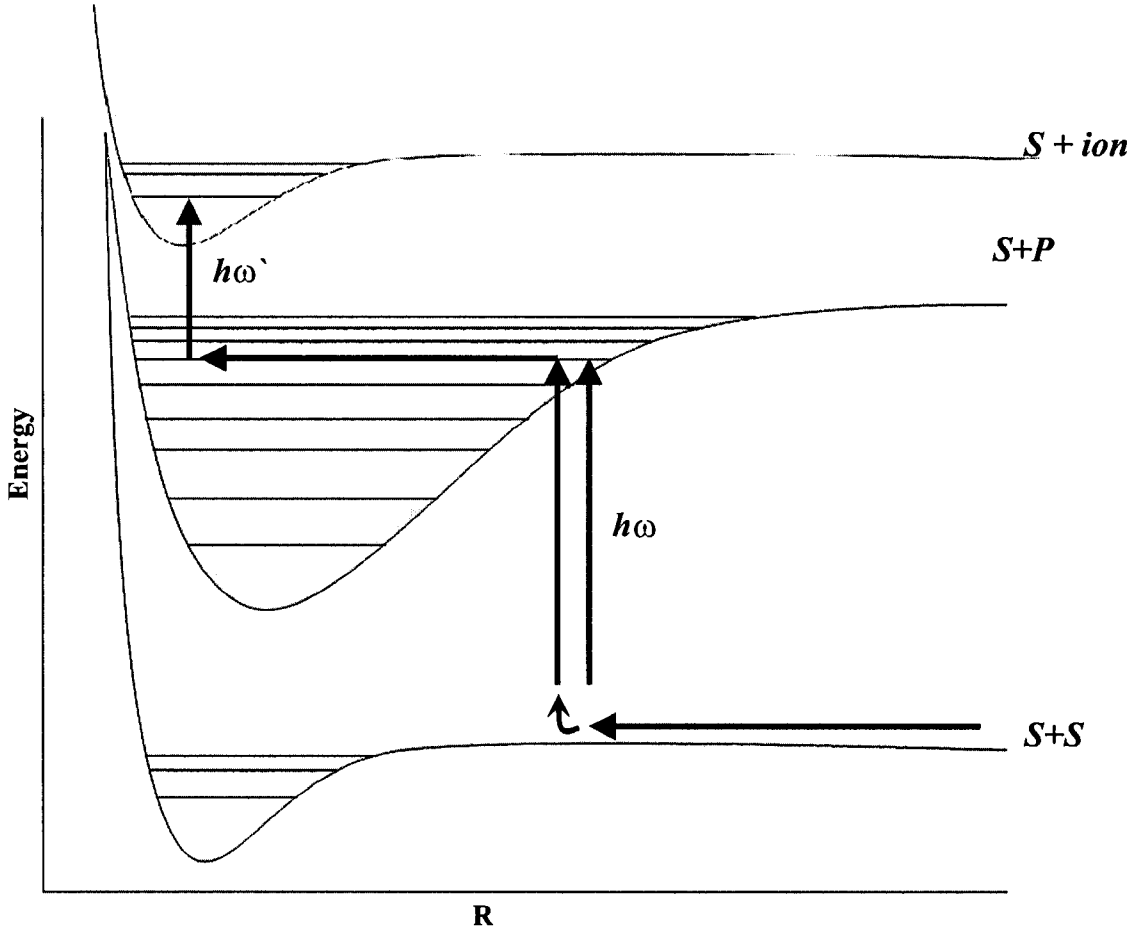

FIG. 9: Schematic of direct photoionization where two atoms undergoing photoassociation are then photoionized. The ion can be easily detected.

II.9 LEROY-BERNSTEIN ANALYSIS

To conduct an analysis of photoassociative spectra, the Leroy-Bernstein method will be used to find the location of ro-vibrational levels of a molecular potential and potentially aid in the identification of series progressions in the spectra. This method is a tool for long-range analysis of the high-lying ro-vibrational states where the atoms spend the majority of the time at large internuclear distances where the electron cloud overlap between the two atoms is absent. At these distances where the coulomb force is very small, the potential is largely determined by atomic parameters and can be well approximated by a series expansion of the form $V(R) = D - C_n/R^n$ where D is the dissociation level and n is the power of the long-range potential. (For two similar atoms in the ground state the potential is dominated by the n=6 term, and for two similar atoms where one is singly excited, the potential is dominated by the n=3 dipole-dipole term).

While it is generally more common to see the Leroy-Bernstein equation for vibrational states of a potential, it is also useful to include the rotational states as well. Here, the derivation of the Leroy-Bernstein equation closely follows that in [41] and in [42]. The development begins with the Jeffreys, Brillouin, Kramers, and Wentzel (JBKB) semi classical method and Bohr quantization condition

$$\nu + \frac{1}{2} = \frac{\sqrt{2\mu}}{\pi\hbar} \int_{R_-}^{R_+} \sqrt{(E(\nu) - V(R))} dR \tag{49}$$

where

$$V(R) = D - \sum_n \frac{C_n}{R^n} \tag{50}$$

and $E(\nu)$ is the energy of level ν, μ is the reduced mass, and R_- and R_+ are the classical inner and outer turning points. If ν is treated as a continuous variable, Equation 49 is differentiated with respect to $E(\nu)$,

$$\frac{d\nu}{dE(\nu)} = \frac{\sqrt{2\mu}}{2\pi\hbar} \int_{R_-}^{R_+} ((E(\nu) - V(R)))^{-1/2} dR \tag{51}$$

and substituting in $V(R)$ with only the dominate n term of the series,

$$\frac{d\nu}{dE(\nu)} \approx \frac{\sqrt{2\mu}}{2\pi\hbar} \int_{0}^{R_+} ((E(\nu) - D + \frac{C_n}{R^n}))^{-1/2} dR \tag{52}$$

By using an approximation for the potential at R_+

$$E(\nu) = V(R_+) \approx D - \frac{C_n}{R_+(\nu)^n} \tag{53}$$

and making a substitution of variables of $u = R_+/R$, Equation 52 becomes

$$\frac{d\nu}{dE(\nu)} \approx \frac{\sqrt{2\mu}}{2\pi\hbar} C_n^{1/n} (D - E(\nu))^{-(n+2)/(2n)} \int_1^\infty u^{-2}(u^n - 1)^{-1/2} du \tag{54}$$

and upon integration becomes

$$\frac{d\nu}{dE(\nu)} = \frac{2\pi\hbar n}{\sqrt{2\mu}} C_n^{-1/n} \frac{\Gamma(1 + 1/n)}{\Gamma(1/2 + 1/n)} (D - E(\nu))^{(n+2)/2n} \tag{55}$$

where Γ is the Gamma function. For the case of $n \neq 2$, the Leroy-Bernstein equation can take the common form of

$$D - E = \left[\left(\sqrt{\frac{\pi}{2\mu}} \frac{\Gamma(1 + 1/n)}{\Gamma(1/2 + 1/n)} \frac{\hbar(n-2)}{(C_n)^{1/n}} \right) (\nu_D - \nu) \right]^{\frac{2n}{n-2}} \tag{56}$$

Through this expression, if a series progression is identified in spectra where the energy differences can be accurately determined, the common C_n for the series can be extracted and then compared to theoretical calculations. Alternatively, the reciprocal action can be taken where if values of C_n are known, the Leroy-Bernstein equation can be used to predict the positions of resonances that may be observed in experimental spectra.

In a further extension of this treatment, an expression for the rotational energies near dissociation can also be derived as outlined in [42]. Here, the rotational constant B_ν is expressed in terms of the expectation value of $1/R^2$. Once again using a semi-classical treatment, this can be expressed as

$$B_\nu = \frac{\hbar}{4\pi\mu c} \frac{\int_{R_-}^{R_+} R^{-2}(E(\nu) - V(R))^{-1/2} dR}{\int_{R_-}^{R_+} (E(\nu) - V(R))^{-1/2} dR} \tag{57}$$

and by again substituting $u = R_+/R$ and letting $R_- \to 0$

$$B_\nu = \frac{\hbar}{4\pi\mu c} \left(\frac{D - E(\nu)}{C_n} \right)^{2/n} \frac{\int_0^\infty (u^n - 1)^{-1/2} du}{\int_0^\infty u^{-2}(u^n - 1)^{-1/2} du} \tag{58}$$

With requiring that $n \geq 2$, integration of this expression leads to an expression for the rotational constant B_ν for states lying near the dissociation limit.

$$B_\nu = \frac{\hbar}{4\pi\mu c} \left(\frac{D - E(\nu)}{C_n} \right)^{2/n} \frac{\Gamma(1 + 1/n)\Gamma(1/2 - 1/n)}{\Gamma(1/2 + 1/n)\Gamma(1 - 1/n)} \tag{59}$$

II.10 MOLECULAR TRANSITION PROBABILITIES

In many photoassociative spectra, it is typical to have numerous peaks of various relative peak heights which are, in large part, determined by the molecular transition probability. If a particular transition has a low probability of occurring, the associated resonance may be difficult to detect in comparison to a resonance associated with a transition with a high probability. The probability of molecular transitions occurring was first described qualitatively by Frank [43] and later mathematically described by Condon [44].

Frank's description of molecular transitions was based on the idea that the "electron jump in a molecule takes place so rapidly in comparison to the vibrational motion that immediately afterward the nuclei still have very nearly the same relative position and velocity as before the jump" [43], although the gradient of the molecular potential may be very different between the upper and lower states. As Condon would later show, it is the wavefunction overlap between the lower and upper states that determines the transition probability, or the Frank-Condon factor.

A few year after Frank's statement, Condon described this using quantum mechanics where the probability of a transition between two states was developed. This derivation follows closely to that in [45]. The transition probability between two states, eigenfunction Ψ and Ψ', respectively representing the lower and upper molecular states, is proportional to the square of transition moment $\mathbf{R}$ where

$$\mathbf{R} = \int \Psi'^{*} \mathbf{M} \Psi d\tau \tag{60}$$

where $\mathbf{M}$ is the matrix for the electric moment and the eigenfunction Ψ can be represented as the product of the electronic and vibrational eigenfunctions as

$$\Psi = \Psi_e \Psi_v \tag{61}$$

If $\mathbf{M}$ is resolved into its two parts, one for the electrons and one for the nuclei,

$$\mathbf{M} = \mathbf{M}_e + \mathbf{M}_n \tag{62}$$

then $\mathbf{R}$ can be written as

$$\mathbf{R} = \int \mathbf{M}_e \Psi_e'^{*} \Psi_v' \Psi_e \Psi_v d\tau + \int \mathbf{M}_n \Psi_e^{*} \Psi_v \Psi_e' \Psi_v' d\tau \tag{63}$$

and since $\mathbf{M_n}$ is independent of the coordinates of the electrons, this may be rewritten as

$$\mathbf{R} = \int \mathbf{M}_e \Psi_e'^* \Psi_v' \Psi_e \Psi_v d\tau + \int \mathbf{M}_n \Psi\prime_v \Psi_v d\tau_n \int \Psi_e'^* \Psi_e d\tau_e \tag{64}$$

where $d\tau_e$ and $d\tau_n$ are the elements of volume around the electrons and nuclei, respectively. Since electronic eigenfunctions for different electronic states are orthogonal to each other, $\mathbf{R}$ can be expressed (provided $\mathbf{M}_e$ does not depend on τ_n)

$$\mathbf{R} = \int \Psi_v' \Psi_v d\tau_n \int \mathbf{M}_e \Psi_e'^* \Psi_e d\tau_e \tag{65}$$

where

$$\mathbf{R}_v = \int \Psi_v' \Psi_v d\tau_n \tag{66}$$

and

$$\mathbf{R}_e = \int \mathbf{M}_e \Psi_e'^* \Psi_e d\tau_e \tag{67}$$

Here the first integral is only dependent on the internuclear distance and the second integral is the electronic transition moment, of which the square is proportional to the transition probability. Expressed in terms of the band intensity for absorption, this result is

$$I_{abs} = \frac{8\pi^3}{3hc} I_o \Delta x N_v v \bar{\mathbf{R}}_e^2 \left[\int \Psi_v' \Psi d\tau_n \right]^2 \tag{68}$$

where $\bar{\mathbf{R}}_e$ is the average value of $\mathbf{R}$ for the electron.

Though these expressions are powerful results, without good approximations for the wavefuntions of the lower and upper states, relative transition probabilities cannot be extracted.

CHAPTER III

EXPERIMENTAL APPARATUS

Though this thesis investigates two independent experiments, the Rb-Ar* trap loss experiment and the photoassociation of Ar* are essentially conducted on the same apparatus aside from small modifications. In order to conduct these investigations, it is necessary, on many facets, to implement a fairly intensive and technical experimental apparatus since the requirements are very demanding. As summarized by Figure 10, there are five distinct sections that make up the entire apparatus, each of which has a critical role in proper experiment operation. These sections are the MOT chamber, the vacuum system, the laser systems, detection systems, and data acquisition.

The MOT chamber is the region where the ultracold sample of atoms will be formed and the investigations will take place. To create and maintain the environment where the MOT can take form requires a cooperative and unwavering effort from the other systems. To minimize the number of collisions that atoms in the MOT may have with the background gas in the chamber, the vacuum system is responsible for maintaining Ultra High Vacuum (UHV) conditions of $\sim 10^{-9}$ Torr in the MOT chamber. The laser systems provide the light fields required to form the MOT as well as any probe laser that will be used. The frequency and power stability of these lasers is critical for maintaining MOT stability and establishing reproducible experimental results. The detection system is comprised of a number of different devices, such as photomultiplier tubes, cameras, a channel electron multiplier, and a residual gas analyzer (RGA) / quadrupole mass spectrometer (QMS) that give a means to detect some observable of the MOT and be recorded. The data acquisition system consists of a number of different components including an interfaced computer, photon counter, multichannel scaler, National Instruments data acquisition (NI-daq) board for Labview, Charge Coupled Device (CCD) camera controller, a Tektronix digital oscilloscope and timing generators. In this section, the details of this apparatus and each of these sections are discussed.

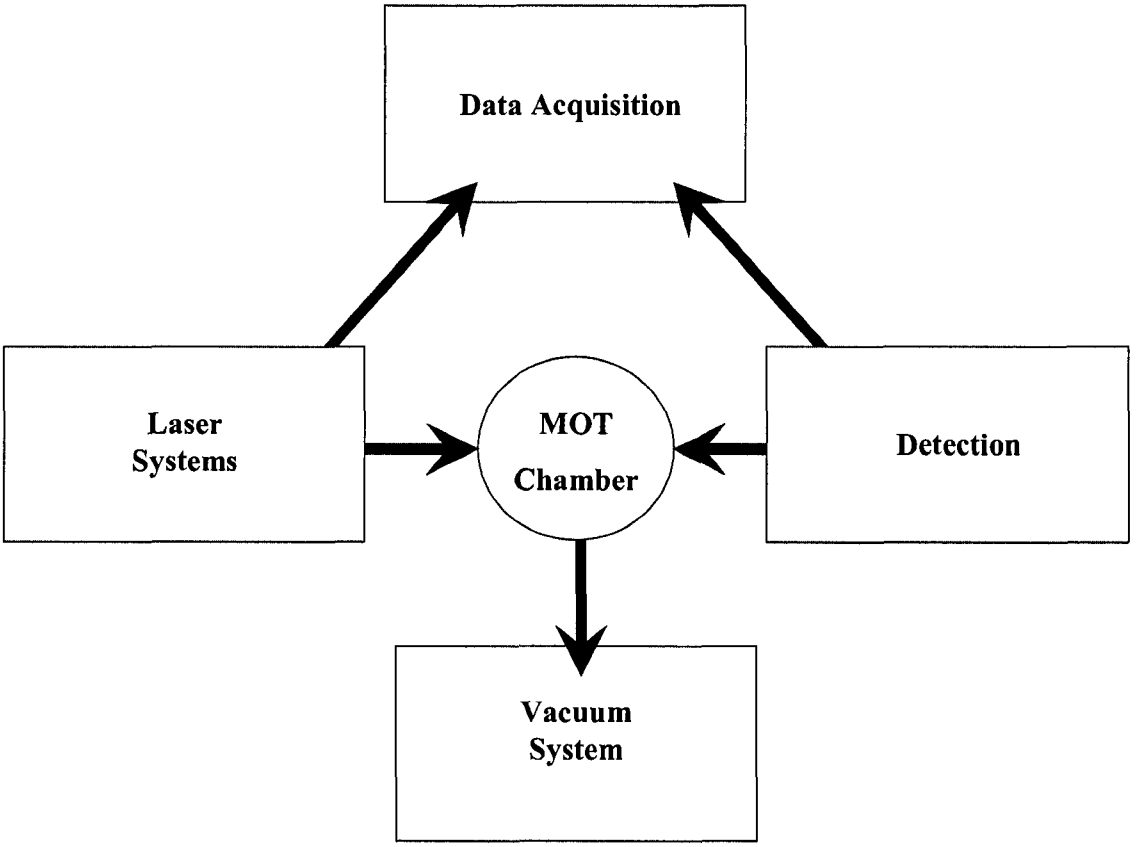

FIG. 10: Simple overview schematic for this experiment.

III.1 AR* SOURCE AND ZEEMAN SLOWER

One of the largest technical differences between the Rb and Ar* MOT is the availability of Ar* for trapping. Where the Rb can be loaded into a MOT simply from a background vapor, Ar in its metastable state is not naturally occurring and must therefore be, by some means, produced and transported into the MOT trapping region. To produce the Ar* for trapping, there are a number of methods which can be used. The most common of which are DC, RF, and microwave discharges. Characteristic of all discharges is that they excite atoms to some distribution of excited atomic and ion states leading to a metastable production efficiency to be relatively low $\sim 10^{-5} - 10^{-4}$ metastable to background atoms. In this experiment, Ar atoms not in the $4s[3/2]_2$ state serve only to increase MOT trap loss due to background gas collisions. With maximum efficiency in consideration, the experiment uses an RF discharge design of Chen *et al.* [46] found to have one of the best metastable yields and a relatively cool production temperature. The discharge in this apparatus was previously constructed by Busch [47]. In summary of this work, the co-axial discharge is constructed of a 1 cm diameter quartz tube pressure fit to the regulated research grade Ar gas source on one end and torr-sealed to the vacuum chamber on the other to accommodate an atomic beam after the discharge. The quartz tube is axially surrounded by an eight loop coil of 14-gauge copper wire approximately 1 cm from the quartz tube. The coil and quartz tube are surrounded by a cylindrical grounded brass shield to which one end of the copper coil is grounded. The other end of the copper coil is attached to the antenna of an RF oscillator. The discharge is driven by a 155 MHz RF signal at ~10-15 W produced by the flow diagram in Figure 12.

Though the pressure of the Ar in the discharge itself is difficult to determine (estimated at 1 mTorr), an ion gauge in the vacuum chamber immediately following the discharge is monitored. By adjusting the flow of Ar to establish the same ion gauge reading, the discharge can be run under similar conditions from day to day. Busch [47] mentions that the maximum metastable production occurs when the pressure in the source chamber is $\sim 1\text{-}5\times10^{-5}$ torr. This figure is confirmed as the MOT seems to locally optimize when the source chamber ion gauge reads $\sim 3.5\times10^{-5}$ torr. However, it was found through experience that the MOT also optimizes at lower pressures. The number of atoms in the MOT is a function of many different contributing factors as Equation 40 suggests and, specifically, is subject to not only the

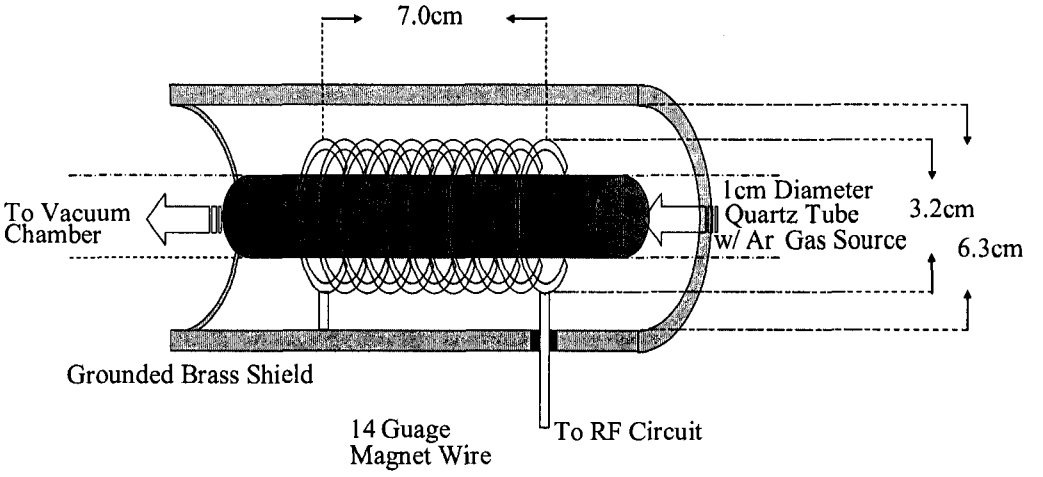

FIG. 11: Schematic of the Ar discharge, the Ar* source for this experiment.

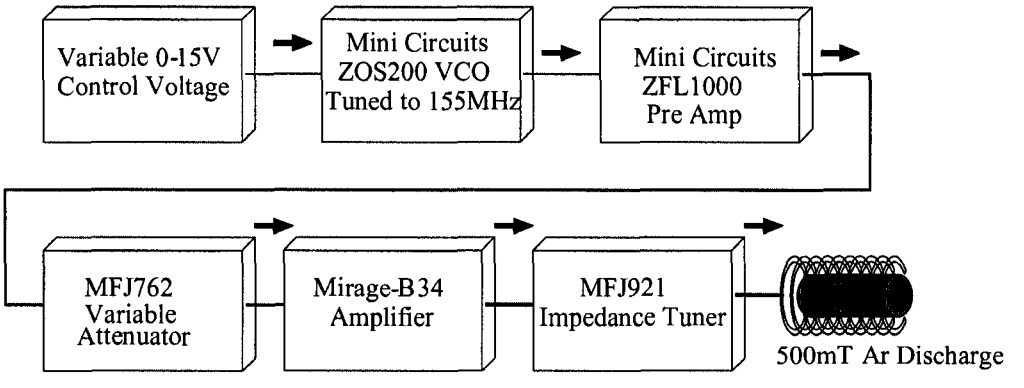

FIG. 12: The flow diagram of the 155MHz RF circuit driving the Ar discharge

number of available metastables contributing to the load rate L, but also the number of background atoms serving to deplete the MOT through collisions making up the loss rate coefficient from background gas, β. This suggests the optimization of the MOT is not trivially related to the optimization of the number of metastables being produced.

Instead of running the discharge with the source chamber ion gauge reading the suggested $\sim 3.5 \times 10^{-5}$ torr, the discharge was run at 8×10^{-6} torr as measured by the source chamber ion gauge. It should be noted that at this pressure, the discharge is not as forgiving in terms of tuning the antenna and standing wave ratio for the circuit and it takes a few tries to maintain the discharge glow. Once glowing, the discharge becomes stable and only minor tuning adjustments are needed. Optimizing the MOT at this pressure requires a subtle, but important step in running the discharge. It must run as brightly as possible and it is critical that the discharge glow extends well passed the region of the resonator coils. Only under these conditions will the metastable production rise and result in a MOT larger than obtainable at the higher source pressure. After the metastables are produced in the discharge, they are transported in a differentially pumped Ar* atomic beam through a Zeeman slower (described here shortly) and to the science chamber where the MOT is formed.

When loading atoms into a MOT, as an atom passes through the cooling and trapping volume, defined as the volume where all six trapping laser beams intersect, the atom will scatter photons, dissipating its momentum and slowing down. If the atom has enough momentum to traverse the entire trapping volume and is not slowed sufficiently, the atom will eventually collide with the science chamber walls and re-thermalize. Hence, only atoms entering the trapping volume with an initial velocity below a certain value can be trapped. This velocity is called the capture velocity and is dependent on the size of the trapping volume, the mass of the atom being trapped, the momentum of the incident photon, and the photon scattering rate (which is in turn proportional to the intensity of the trapping light and its Doppler shifted detuning to the atoms resonant transition). The capture velocity for both Rb and Ar* are $\sim$50 m/s, compared to the average velocity of a thermal source of atoms being $\sim$300 m/s.

When trapping Rb and other alkalis in a MOT, this does not present much of a problem because the Maxwell-Boltzmann distribution for a thermal background vapor of ($\sim$1 Torr) Rb has a sufficient percentage of the source atoms below the

capture velocity. Cooling and trapping of the slower atoms of this distribution is sufficient to load a MOT of a few million atoms. The case for Ar* is quite different. Due to the low metastable production efficiency of the RF discharge and the low density of the Ar* atomic beam, the number of Ar* atoms below the capture velocity is horribly insufficient and the MOT cannot confine many atoms. In addition, the Ar* atoms that are not trapped immediately upon exiting the atomic beam will collide with the chamber walls and quench, ultimately contributing to background gas and trap loss. One effective method to increase the number of atoms available for trapping is to compress the thermal distribution of the atoms to within the capture velocity by using a Zeeman slower.

Like the MOT, the Zeeman slower also uses the spontaneous light force to slow Ar*, but only in the one dimension along the atomic beam. The challenge here is to have the laser light maintain resonance with a large distribution of incoming atom velocities (and associated Doppler shifts) such that a large percentage of the Ar* atoms are slowed to the desired velocity for MOT capture. By exploiting the Zeeman splitting of the excited $4p[5/2]_3$ state in Ar*, a magnetic field can be applied such that the Zeeman shift is equal to the Doppler shift of the atom for a given velocity, following

$$k\nu(z) - \frac{\mu_B B(z)}{\hbar} + 2\pi\delta = 0 \tag{69}$$

where $k = 2\pi/\lambda$, μ_B is the Bohr magneton, $B(z)$ is the variable magnetic field along the axis of the atomic beam, and $\delta = \omega_L - \omega_A$. By using a tapered solenoid around the atomic beam, the magnetic field can be designed for a range of velocities such that a thermal atom, of v< 300 m/s will be resonant with the slowing light for up to the entire length of the solenoid. For this to occur, the taper of the solenoid coil density needs to be such that the axial magnetic field is of the form

$$B(z) = \frac{\hbar 2\pi\delta}{\mu_B} + \frac{\hbar k v_i}{\mu_B}\sqrt{1 - \frac{z - z_i}{z_f - z_i}\left(1 - \frac{v_f^2}{v_i^2}\right)} \tag{70}$$

The Zeeman slower in this apparatus was previously designed and fabricated by Busch. Specifications and further explanation can be found in [47]. For the purpose of this dissertation, only a general overview and relevant parameters will be discussed. Shown in Figure 13, the Zeeman slower in this experiment is composed of two separate tapered solenoids for a few reasons detailed in [47]. It is important to note that the

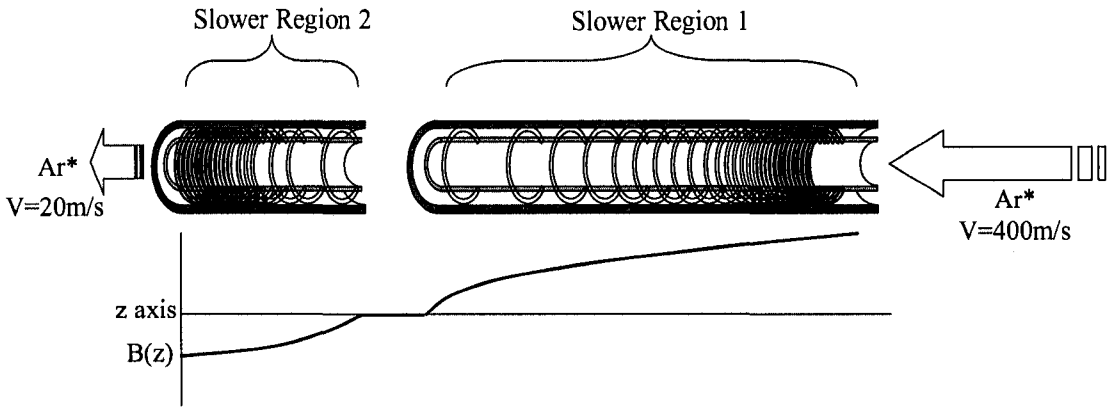

FIG. 13: Schematic of the Ar* Zeeman slower.

laser light used for slowing the atoms in the Zeeman slower is $\sim$30 I_{Sat} of σ^+ circularly polarized light, detuned 160 MHz red of the $4s[3/2]_2$ to $4p[5/2]_3$ trapping transition as to not disturb or unbalance the MOT. See [47] for other relevant parameters.

III.2 THE VACUUM SYSTEM

Due to the nature of this research, it is imperative that the experiment is conducted under the highest vacuum reasonably achievable. Trap loss from hot background atoms even at μTorr pressures is sufficient to reduce the number of trapped atoms to near nil. In many alkali metal traps, it is typical to have a sealed stainless steel chamber evacuated to $\sim 10^{-9}$ Torr or lower in pressure and load the MOT from a low density background vapor of atoms. In this experiment, however, we have the challenge of trapping Ar in its metastable state. With a lifetime of 60 seconds and no efficient means to excite Ar to the metastable state in low density background vapor, the metastable argon is produced in an RF discharge at $\sim 10^{-3}$ Torr. Since a science chamber pressure of $\sim 10^{-9}$ Torr is preferred, the Ar* atoms must be transported to the chamber with their state preserved while simultaneously differentially pumping to achieve the UHV pressures in the science chamber.

Figure 14 shows the basic schematic for the vacuum system. Here, research grade Argon flows through a dual-stage brass regulator to a leak valve (Granville Phillips Company 5097) controlled by a 216 Servo Driver. The Argon then flows through stainless steel flexible pipe to the 1 cm diameter quartz tube of the RF discharge. In

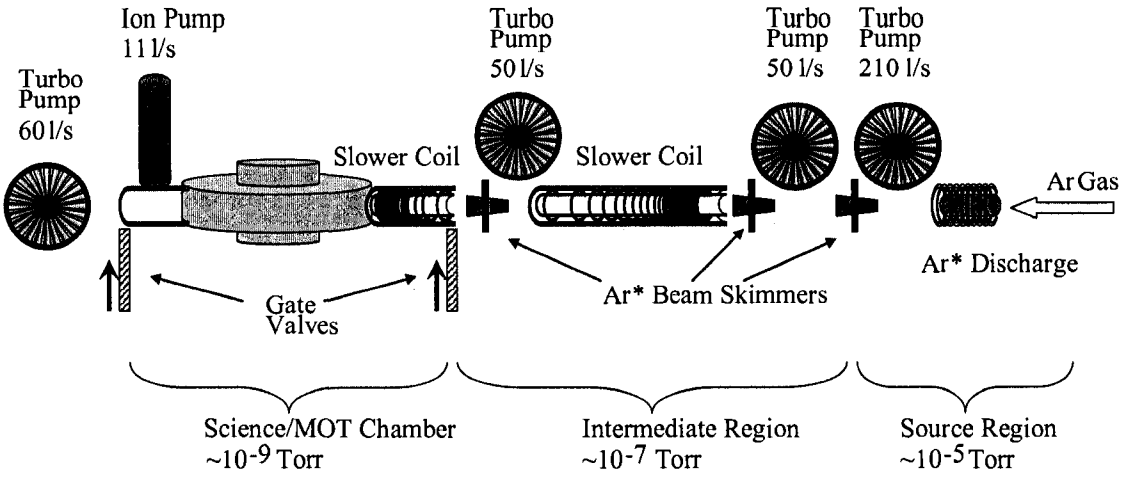

FIG. 14: Simple schematic of vacuum system for this experiment

the first pumping region near the Ar source and RF discharge, a skimmer, constructed of a 1 cm diameter pipe with a tapered end and torr-sealed into a flange, is the first stage of Ar* beam collimation and differential pumping. The rejected atoms are then subject to a Pfeiffer TMU262P 210- l/s turbo pump, and an ion gauge for pressure monitoring. When running the experiment, this pressure is normally $\sim 10^{-5}$ Torr, and $\sim 10^{-7}$ Torr when the Ar source is closed. Also residing in the region between the RF discharge and the skimmer, is a field plate assembly held at -200 V to deflect ions that may be in the atomic beam.

The second pumping region has another skimmer as in the first region where rejected atoms are subject to a Pfeiffer TPH050 50- l/s turbo pump. Here another ion gauge monitors the pressure in this region to be $< 10^{-5}$ Torr when running and $\sim 10^{-7}$ Torr with the Ar source closed. The next region is the Zeeman slower region where the Ar* atoms are slowed and a third skimmer and turbo pump (TPH050) reside at the end before a gate valve (MDC 1500) which can isolate the science chamber from the rest of the atomic beam vacuum system. The science chamber is pumped on by another turbo pump, Pfeiffer TPU071-60 l/s, though another gate valve (MDC 1500) as well as an Ultek D I-11 l/s ion pump. When running, this vacuum system can hold the science chamber at a sustainable $\sim 5\times10^{-9}$ Torr pressure with a modest population of slowed Ar* available for trapping. When sealed by both gate valves, the science chamber is held at $\sim 10^{-9}$ Torr by the ion pump alone.

All turbo pumps are backed by 2 Alcatel ZM2004A roughing pumps which supply a backing pressure of $\sim 5 \times 10^{-2}$ Torr as measured by two Duniway DST-531 thermocouples located near the backs of the turbo pumps. To minimize acoustic vibration and oil vapors in the laboratory, these pumps are located in a storage closet in a separate room and vacuum is supplied through ~20 feet of 3/4" inner diameter flexible reinforced pvc vacuum tube.

III.3 THE SCIENCE CHAMBER

The science chamber for these experiments is a stainless steel chamber with 12 ports in the horizontal plane and 2 in the vertical, each fitted for 2-3/4" conflat connections sealed with copper gaskets. Four ports in the horizontal plane and both in the vertical are capped with 2-3/4" conflat viewports with a 1.5" window coated for broad IR transmission. These ports are dedicated for the trapping and cooling lasers essential for MOT operation. One of these four ports has a conflat-T where a valve and Rb Getters are stored. During Rb MOT operation, a 3.2 amps electric current runs through a series pair of getters to supply the Rb vapor to the science chamber. There is one port connected to the end of the Zeeman slower through a gate valve (MDC1500) allowing the Ar* atoms to enter the science chamber. Directly opposite this port is a conflat-T with an IR coated window where the slower light can be directed along the Zeeman slower, counter propagating the flow of Ar*. The other end of the T hosts the ion pump which continuously pumps on the system when under UHV. Another port is connected to the other gate valve leading to the science chamber turbo pump. Directly opposite this port is a conflat feed-through and mount hosting the Dr. Jsutz channel electron multiplier for ion/electron detection. Two directly opposite ports are capped with uncoated windows used for fluorescence observation and MOT probe lasers. The two remaining ports on the science chamber have been fit with the RGA and ion optics described in the Detection Section. Because of the limited number of ports and large number of experimental needs, many of the ports have been used for multiple and ever-changing purposes. In particular, the ports dedicated for fluorescence and MOT probing also would host CCD cameras and probes for fluorescence and absorption imaging, as well as the ports for the pulsed laser for molecule detection and others.

III.4 THE RB AND AR* MAGNETO-OPTICAL TRAP

With the Rb and slowed Ar* now present in the UHV science chamber, the conditions for a MOT need to be applied. As described in the MOT Theory section, six red detuned circularly polarized laser beams need to intersect in the presence of a magnetic field gradient whose minimum resides near the center of the trapping volume. To achieve this magnetic field gradient, a pair of anti-Helmholtz coils were fashioned symmetrically along the Z (vertical) axis, with each coil on either side of the science chamber having 30 turns of 14-gauge copper wire with a radius of 5 cm and carrying 6.0 amps DC producing a 6.6 Gauss/cm magnetic field gradient along the Z axis and 3.3 gauss/cm along the X and Y axes. In addition to the anti-Helmholtz coils, three additional coils, shim coils, are arranged perpendicular to each other around the science chamber and are used to mitigate the effects of stray magnetic fields from the near-by ion pump, other electronics and the Earth's magnetic field. Each shim coil has ~30 turns with radius 15 cm using 22-gauge copper. Three laser beams that form the MOT intersect perpendicularly and are single pass retro-reflected to ensure a good balance between the light forces along the different directions. The simultaneous trapping of two different species in a MOT is functionally similar to the trapping of a single species. The main difference being the need for additional lasers tuned specifically to trap the second species of atoms. Conveniently, the magnetic field gradient can be the same for both species. At the science chamber the 811 nm (Ar*) and the 780 nm (Rb) trapping laser light individually are decoupled from a Thorlabs FS-SN-3224 FC/APC fiber optics using a Thorlabs C110TM-B f=6.24 mm lens for collimation. Ideally a dichroic beam splitter would be used to make the two beams collinear. Unfortunately, because the wavelengths are only ~30 nm apart, the necessary optic is unavailable. Alternatively, after the two separate trapping lasers are collimated, they each pass through high quality, $\lambda/4$ and $\lambda/2$ waveplates, AR coated for each respective wavelength. Here the 780 nm Rb trapping laser is rotated to have vertical linear polarization while the 811 nm Ar* trapping laser is rotated to have horizontal linear polarization. The two lasers are then spatially overlapped using a broadband, IR coated polarizing beam splitter and IR mirrors. Though the polarization axis of each beam is perpendicular to the other, it turns out to be of little consequence for the experiment. After combination, the beams are then expanded to ~1.5 cm by a two lens telescope M≈7.5 which is the optimal beam width for steering with 1" optics. The lasers then pass through a broadband IR coated $\lambda/2$

waveplate just before another broadband IR coated polarizing beam splitter which reflects some light in the z direction. The $\lambda/2$ waveplate allows for manipulation of the relative intensity of light passing through the beam splitter (going to the X and Y axes) vs being reflected (going to the Z axis). The light that is reflected upwards in the z direction is then steered through a $\lambda/4$ waveplate to become σ^+ circularly polarized light before it passes through the IR coated top chamber window to the center of the science chamber along the Z axis. The Z axis light exits the chamber via another IR coated chamber window where a $\lambda/4$ waveplate changes the polarization to linear light. A mirror directly after the $\lambda/4$ waveplate retro reflects the laser beam. As the laser beam passes through the $\lambda/4$ waveplate a second time, it is now σ^- circularly polarized light. The remaining light that did not get directed to the Z axis is then split on a broadband 50/50 beam splitter sending light to the X and Y axes with balanced intensities. Light along each axis passes through an identical optics train to the Z axis with the conditions in the science chamber of having σ^+ light along the forward X and Y axes and the retro reflection σ^-. Special care is taken to ensure all laser beams intersect perpendicularly in the center of the science chamber and to ensure the retro reflections are well aligned. It is important to note that once a MOT is loaded, the alignment (especially the retro reflections) is tuned for the optimal MOT.

The Zeeman slower beam is decoupled from a Thorlabs FS-SN-3224 FC/APC fiber optic by an C110TM-B f=6.24 mm lens which collimates the beam. It then passes through a $\lambda/4$ waveplate and an IR coated $\lambda/2$ waveplate and a polarizing beamsplitter to ensure polarization is horizontally linear. After a final $\lambda/4$ waveplate to become σ^+ circularly polarized, the beam is then steered into the science chamber and into the Zeeman slower along the axis of the atomic beam.

III.5 LASER SYSTEMS

In this section, information and characteristics of the laser systems used in this experiment will be covered. Since the advent of semiconductor laser diodes, they have found numerous applications in everyday life, from CD, DVD and now "Blu Ray" disk players, to laser range finders, sights and levels, and many more. The everyday demand for these laser diodes and emerging new applications drove the industry into mass production and striving for more robust, stable, and consistent product. Consequently, with free running wavelength ranges spanning nearly the

entire visible and NIR spectrum, laser diodes have become an economical solution for low power laser needs, at costs of $10-$100 per unit, and are now commonplace in research laboratories worldwide.

A characteristic of laser diodes is that, to a certain degree, the free running wavelength can be grossly changed by varying the electric current and/or the temperature which effectively change the low finesse facet cavity of the diode. This method does not give the control needed to maintain the laser frequencies at the sub MHz level required for this experiment. As it turns out, if a small amount of external laser light is injected into the laser diode, the laser diode will lase at the injected wavelength provided the power is sufficient and the wavelength is within a few GHz of the free running wavelength of laser diode. This method is known as injection locking and a laser in this configuration is referred to as a Slave. Alternatively, by placing the laser diode in an external cavity of the Littrow or Littman-Metcalf geometry, fine control of the laser frequency is possible by adjusting the cavity to send a specific wavelength off the diffraction grating. An external cavity diode laser (ECDL) in this configuration is referred to as a Master laser and some of the laser light from this cavity will be used to injection lock the Slave. Hence, by controlling the Master, the Slave is also controlled.

III.5.1 Rb Trapping Laser

As previously mentioned, in order to optically cool and trap ^{85}Rb, two laser frequencies are needed: The trapping laser (λ=780.242 nm), and the hyperfine repumper (λ=780.050 nm). The laser source used to reach these frequencies are semiconducting laser diodes whose free running wavelength is within a few nm of the desired wavelengths. To help isolate the lasers from frequent and noticeable acoustic vibrations in the laboratory, lasers are mounted on the TMC floating optical table.

The master laser, a Sanyo DL-7140-201S laser diode is mounted in a CT110TM-B collimation tube placed in a home built Littman-Metcalf cavity, depicted in Figure 15, where the light emitted from the laser diode is incident at 45 degrees on a 1200 lines/mm grating (Edmund Optics NT43-848). In the Littman-Metcalf cavity, the diffractive 1st order is reflected off an IR coated mirror back upon the grating and into the laser diode for optical feedback. The mirror responsible for the alignment of the feedback is mounted on an adjustable mirror mount with a piezoelectric transducer (PZT), Thorlabs AE0203D04, controlling the alignment in the horizontal plane of the

FIG. 15: Image of a Master Diode laser in Littman-Metcalf geometry.

cavity. The PZT has a translation of 3.0±1.5 μm at 100 V applied voltage and can therefore make very fine adjustments to the angle of the mirror, effectively changing the angle (and wavelength) of the feedback to the laser diode. The wavelength of ECDL is then determined by the diode current, diode temperature and the angle of the feedback light returning to the laser diode. To have the diode laser run at the desired wavelength, all of these must be of the correct settings. To aid in temperature stabilization of the diode and the cavity, the collimation tube housing the laser diode is secured in an aluminum bezel. The bezel contacts a thermoelectric cooler (TEC), Marlow DT12-6-01, which sinks heat to a large aluminum base. This and all other components of the cavity are mounted to an aluminum baseplate, surrounded by an aluminum box (with milled access and laser output holes), and tightly secured to the optical table. Once running properly, the ECDL produces a single-mode spectral line with <1 MHz linewidth, capable of being tuned by the PZT over the 700 MHz free spectral range of the cavity with <1 MHz precision in frequency control. The specular reflection off the grating is the output of the cavity. Of particular importance to the single-mode operation of diode lasers is the presence of an optical isolator (optical diode) strategically placed to attenuate returning light to the cavity by -40dB. Without optical isolators, μW of laser light returning to the cavity can result in unwanted spectral multi-mode behavior of the laser.

Though the laser power output of the diode laser is ~50 mW, the external cavity

introduces significant losses resulting in a cavity output power of only ~10 mW. To increase the laser power available, while maintaining the control of the ECDL Master, part of the Master laser light is used to injection lock a slave laser. Similar to the master laser diode, the slave laser is also a Sanyo DL-7140-201S laser diode housed in a Thorlabs CT110 collimation tube and secured in an aluminum bezel where the temperature is also controlled by a TEC in a similar fashion. The slave, however, does not have an external cavity as the master ECDL has and doesn't suffer the associated losses. To injection lock the slave laser, a 10% reflectivity glass beam splitter directs ~1 mW of master light into the slave, collinearly to the output laser beam of the slave diode laser. With proper current and temperature settings, the slave laser then can run (or be "pulled") at the same running wavelength as the master ECDL. The output of the slave laser then passes through the same beam splitter used to injection lock it (suffering a 10% loss) and is then sent through a number of optics and eventually to the Science chamber where it will cool and trap the Rb with ~10 mW of laser power.

For proper MOT operation, the trapping laser frequency must be maintained with <1 MHz precision and accuracy. The MOT will optimally function when the trapping laser frequency is run at -2Γ (or ~12 MHz) red detuned from the atomic $5^2S_{1/2}$ F=3 to $5^2P_{3/2}$ F=4 transition. Any deviance from this frequency results in a change in the atom density and/or size of the MOT. To lock the laser at this absolute frequency, doppler-free saturated absorption spectroscopy (SAS) of ^{85}Rb is used in a method of phase sensitive detection.

For the SAS of Rb, a beam splitter reflects ~1 mW from the master laser into the geometry shown in Figure 17 where a thick beam splitter sends two weak beams through a quartz cell filled with 500 mTorr of a ^{85}Rb and ^{87}Rb vapor. After passing through the vapor cell, two small glass beam splitters reflect some of the weak probe beams into two photodiodes in a difference taking I to V converter where the relative power of each probe beam after the vapor cell is monitored. The remaining strong, or "pump", beam that passes through the first beam splitter is steered by mirrors to overlap and counter-propagate one of the weak probe beams. Without the pump beam present, as the laser is scanned by the PZT through the atomic resonance, the probe lasers will be partially absorbed by the Rb atoms in the vapor cell and an absorption spectrum can result. However, in this geometry, the hyperfine structure present cannot be resolved due to the ~500 MHz of Doppler broadening resulting

from the thermal distribution of atoms in the vapor cell. By allowing the more intense pump beam to counter-propagate one of the probe beams, a Doppler-free saturated absorption spectrum can be obtained where the hyperfine structure can be resolved. This can be understood in the following way. When the laser is tuned to an atomic resonance, both the probe beams and the pump beam can interact with the Rb atoms of various velocity classes in the vapor cell. When the laser is detuned off resonance, the forward propagating weak probe beam will interact most strongly with Rb atoms that have a parallel velocity class $v_{||}$ in the laboratory reference frame due to the Doppler effect. On the other hand, the counter-propagating pump beam will interact with Rb atoms that have a parallel velocity class $-v_{||}$. If the laser is sufficiently detuned, the probe beam will pass through the vapor cell the same as if the pump beam were not present. As an atomic resonance is approached by tuning the laser, the two velocity classes being excited by the probe and pump beams, begin to converge to a single velocity class of $v_{||}$=0 where both lasers are interacting with the same atoms. Because the pump beam is ~10 times more powerful than the probe beam, the probe beam saturates the $5^2S_{1/2}$ F=3 to $5^2P_{3/2}$ F=4 transition, resulting in the probe beam passing through the vapor cell mostly unabsorbed. By using the second, unsaturated probe beam as a reference signal and scanning the laser, a doppler-free saturated absorption spectrum can be obtained where the atomic resonances are resolved with widths close to the natural linewidth. Figure 16 shows the saturated absorption spectrum for ^{85}Rb along the F=3 to F=2, 3, 4 transitions. It is important to note that in the Rb vapor cell, there are four groups of S-P transitions (each with resolved hyperfine structure) that are near the same wavelength and should be addressed. Two of these transitions are in ^{85}Rb and two are in ^{87}Rb. Of the two in ^{85}Rb, one group arises from the $5^2S_{1/2}$ F=3 to $5^2P_{3/2}$ F=2, 3, 4 transitions, the others from $5^2S_{1/2}$ F=2 to $5^2P_{3/2}$ F=1, 2, 3. The case is similar for ^{87}Rb. Since we are trapping only ^{85}Rb, only the first two groups of spectra are relevant. It is also important to notice the presence of two crossover peaks in the spectra. These peaks are purely artifacts of the SAS, but are very useful in the experiment. These extra peaks arise when the pump beam interacts with a blue shifted velocity class of one transition (say F=3 to F=4) while simultaneously interacting with a red shifted velocity class from another transition (say F=3 to F=3). The resulting depletion in the ground state is observed as a strong absorption line.

The SAS spectrum is used as an absolute frequency reference to help maintain

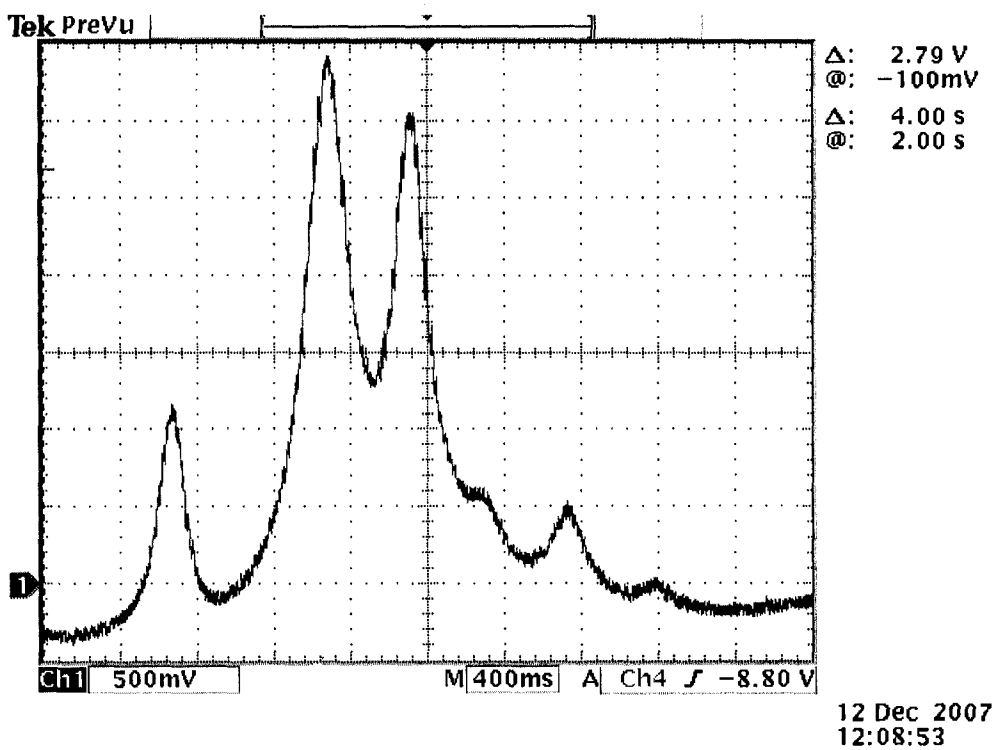

FIG. 16: Saturated absorbtion spectrum for ^{85}Rb along the F=3 to F=2,3,4 transitions. The two largest peaks are crossover peaks.

the -12 MHz detuning from the $5^2S_{1/2}$ F=3 to $5^2P_{3/2}$ F=4 transition. To accomplish this, a lock-in amplifier Princeton Applied Research model 120 is used to create an error signal by which active feedback will make necessary adjustments in the cavity to maintain a given frequency. Here, the current to the master ECDL is modulated by the 10 kHz reference signal generated by the lock-in amplifier. This modulation on the current effectively modulates the laser frequency of the master which is then sent to the SAS where as before, an absorption spectrum is obtained. A lock point is chosen generally to be the maximum of an absorption peak in the SAS spectrum. The signal from the SAS is then input back into the lock-in amplifier where it is de-modulated, integrated and conditioned into a useful error signal. The magnitude and sign of the error signal is proportional to how far, and in what direction, the laser is from the lock point. When activated, a home built circuit adds the error signal with an appropriate gain to the voltage on the PZT, correcting the cavity to output the laser frequency defined at the lock point.

Unfortunately, there is not a maximum to an absorption line in the SAS spectrum of Rb that is precisely at -12 MHz detuned of the Rb trapping transition. To accomplish this, before the laser from the master ECDL enters the SAS, it passes through an acousto-optical modulator (AOM) that shifts the frequency of the light by ±60-100 MHz. By choosing an appropriate peak in the SAS spectrum as a lock point for the shifted master, the AOM can shift the laser such that the master runs at the proper detuning for trapping. Conveniently, the F=2/3 crossover peak in the SAS spectrum lies 92 MHz from the required detuning. By using an AOM to shift the light by -80MHz the proper detuning of -12 MHz is obtained. Alternatively, as in this experiment, if a slave laser is used and switching is required to turn the trapping laser on and off for the experiment, the AOM can instead shift the slave laser light -80 MHz before being sent to the science chamber for cooling and trapping. The AOMs on the trapping lasers are salvaged NEC AOMs, driven by mini circuits ZOS-100 voltage controlled oscillators (VCO) operating at a typical 80 MHz frequency, whose signal is amplified by ~30 dB to ~32 dBm by a home-built amplifier using Motorola electronics. The specific Rb trapping laser geometry is detailed in Figure 17.

Lastly, for the Rb MOT to function optimally, a second laser frequency (the hyperfine repumper) is required to repopulate the $5^2S_{1/2}$ F=3 ground state. In some experiments where precise control over this laser would be advantageous, such as dark-spot MOTs or others [38], a separate laser source is needed. This separate laser

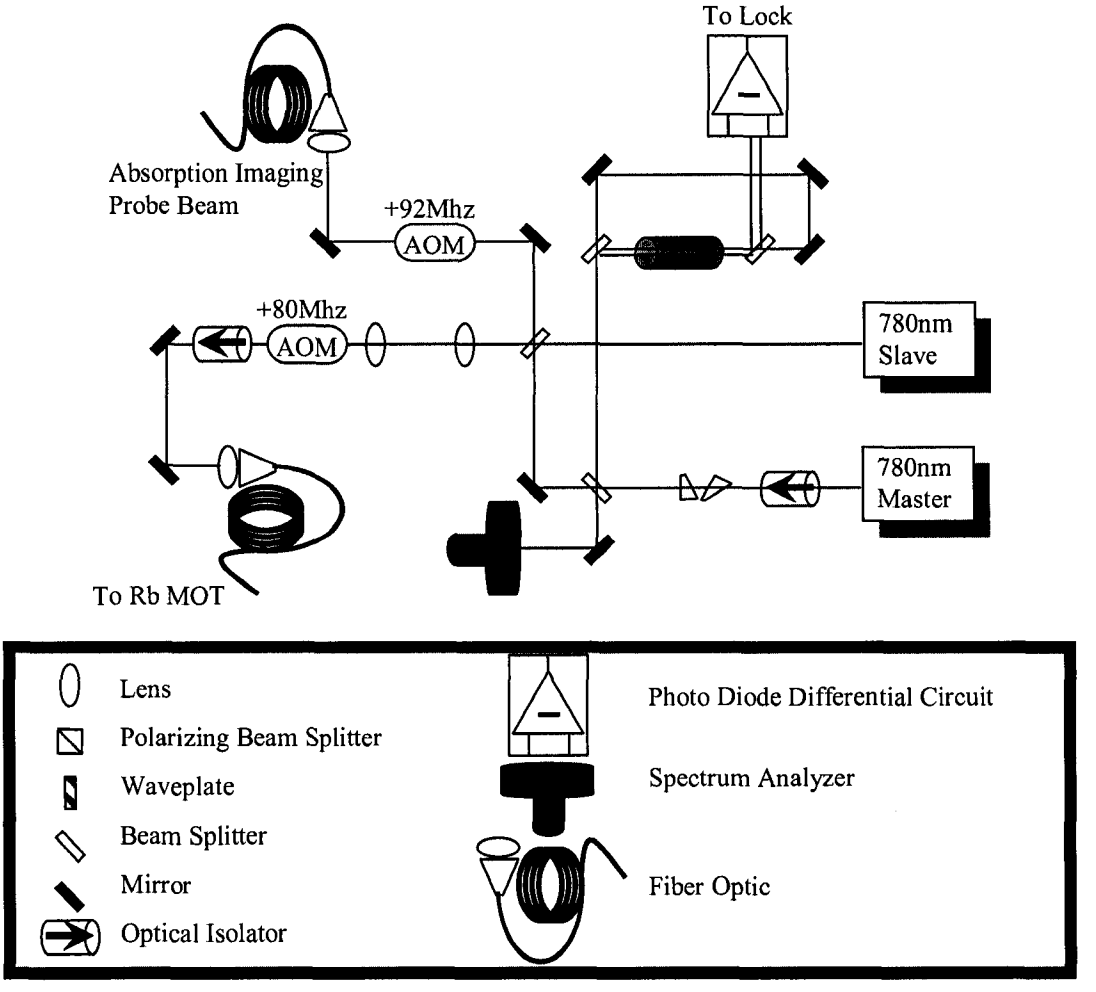

FIG. 17: Schematic of the optical path of the 780 nm Rb trapping laser diodes.

would be designed very similarly to the master-slave setup for cooling and trapping as detailed above. Two main differences would be that the required laser power would be much less and the frequency to which the laser is locked would be that of the $5^2S_{1/2}$ F=2 to $5^2P_{3/2}$ F=3 transition. But in experiments such as this one, the addition of a hyperfine repumper can be done with a laser already in use. The frequency required for the hyperfine repumper is ~3 GHz larger than the trapping laser for the Rb. By modulating the current of the slave laser for trapping the Rb at ~3 GHz, two sidebands are produced on the spectrum of the trapping laser, ± ~3 GHz away from the fundamental as observed on a spectrum analyzer (Burleigh SA FSR 2 GHz). The -3 GHz is of no consequence for this experiment, and the +3 GHz will serve as the hyperfine repumper. By adjusting the amplitude of the microwave modulation, the relative amplitude of the sidebands can modestly be controlled. It is estimated that ~99% of the light is in the fundamental for trapping, leaving ~1% for hyperfine repumping.

The Slave laser light is ultimately coupled into a Thorlabs FS-SN-3224 FC/APC fiber optic via Thorlabs C110 lens and transported to the science chamber with ~10 mW of laser power after the fiber optic. The slave is spectrally observed on the spectrum analyzer to ensure proper pulling and behavior. The remainder of the light from master ECDL that was not used in the SAS or injection locking the slave will be used as a resonant probe beam in absorption imaging.

III.5.2 Ar* Trapping and Zeeman Slower Lasers

Many aspects about the lasers for trapping Ar* are very similar to that for trapping Rb. Since the trapping frequency of Ar* is 30 nm away from that of Rb, a different laser diode is used, a Sanyo DL-LS-2031 150 mW and due to the laser power requirements for the trapping laser and the Zeeman slower laser, a master-slave-slave configuration will be used with one slave dedicated to the trapping frequency and the other slave dedicated to the Zeeman slower frequency.

Also mounted on the TMC floating optical table, the 811 nm master ECDL is nearly identical to the 780 nm master ECDL detailed above with the exception of a different model diode laser. Here, a Sanyo DL-LS-2031 is in place of the Sanyo DL-7140-201S. The same model collimation tube and external cavity components and geometry are employed. The master ECDL is optically isolated from the rest of the beam path by -40dB attenuation of an OFR optical isolator. The slaves are

also mounted and collimated in the same fashion as detailed above. To injection lock the two separate slave lasers, a slight difference in geometry is used in order to maximize available slave laser power. Where the use of a beam splitter could pick off a small amount of master ECDL light and injection lock the slave, the slave will invariably suffer a loss when passing through the same beam splitter. Instead, the slave laser housing/collimation tube is rotated such that the laser output is polarized vertical linear. The slave laser light is incident on an IR coated, polarizing beam splitter (PBS) where 99% of the light is reflected and continues on. The master laser is also incident on this PBS, but passes through a $\lambda/2$ waveplate just prior. This waveplate rotates the polarization such that most of the light is vertically polarized and gets reflected, but the small horizontally polarized component is transmitted where it injection locks the slave laser. Though a slave laser does not pull quite as easily with the injection laser polarization perpendicular to the output, it can be done and works well. This method has two benefits justifying its use. First, there is a very low loss in slave power as compared when using just a glass beam splitter, and second, by simply rotating the $\lambda/2$ waveplate, the amount of master laser power can be easily adjusted. This method is used twice, once for each slave, and the remaining master light continues to the SAS. Figure 18 provides a schematic of the laser path geometry.

As in the SAS geometry previously discussed for the Rb trapping laser, a thick beam splitter sends two weak probe beams through a vapor cell where absorption can take place and the pump beam is then aligned to overlap with one of the probe beams as to obtain a Doppler-free absorption spectrum when the laser is scanned over the atomic resonance. Unfortunately, the atomic resonance needed for a reference frequency, the 811 nm trapping transition for Ar*, is not available when Ar is in its true ground state, $3p^6(^1S_0)$. To create a population of Ar* in the Ar gas cell, the same discharge as described in the Ar* source section is designed around the vapor cell. With similar electronics and physical dimensions for the resonator, the only difference between this discharge and the Ar* atomic beam source is the closed gas cell instead of a flow of Ar. The difference turns out to be of little consequence. With a population of Ar* in the reference cell, the SAS spectrum can be obtained, shown in Figure 19.

The master EDCL for Ar* is locked to the maximum of the absorption line in exactly the same manner as the Rb master ECDL is locked, by using a Stanford

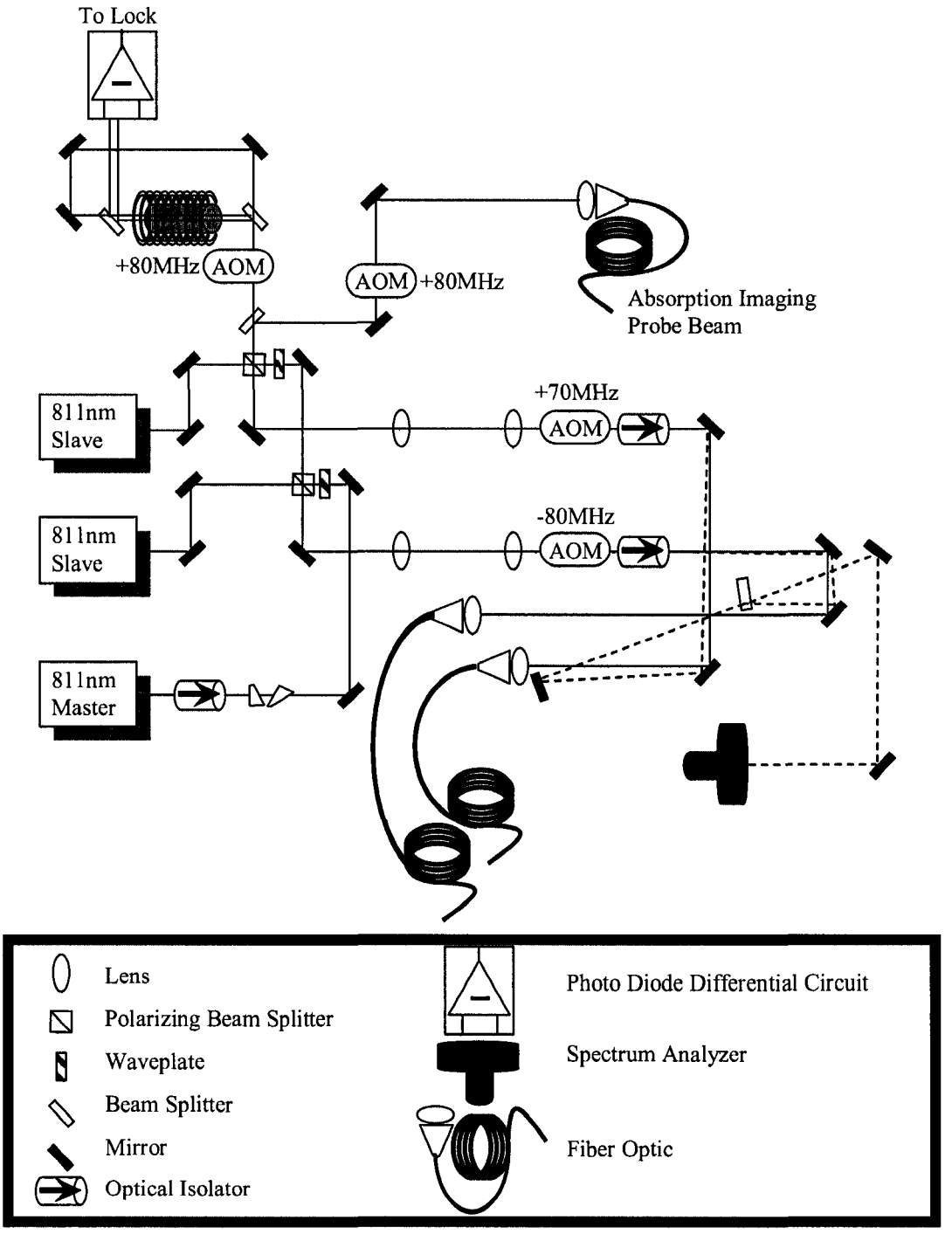

FIG. 18: Schematic of the optical path of the 811 nm Ar* trapping and slowing laser diodes.

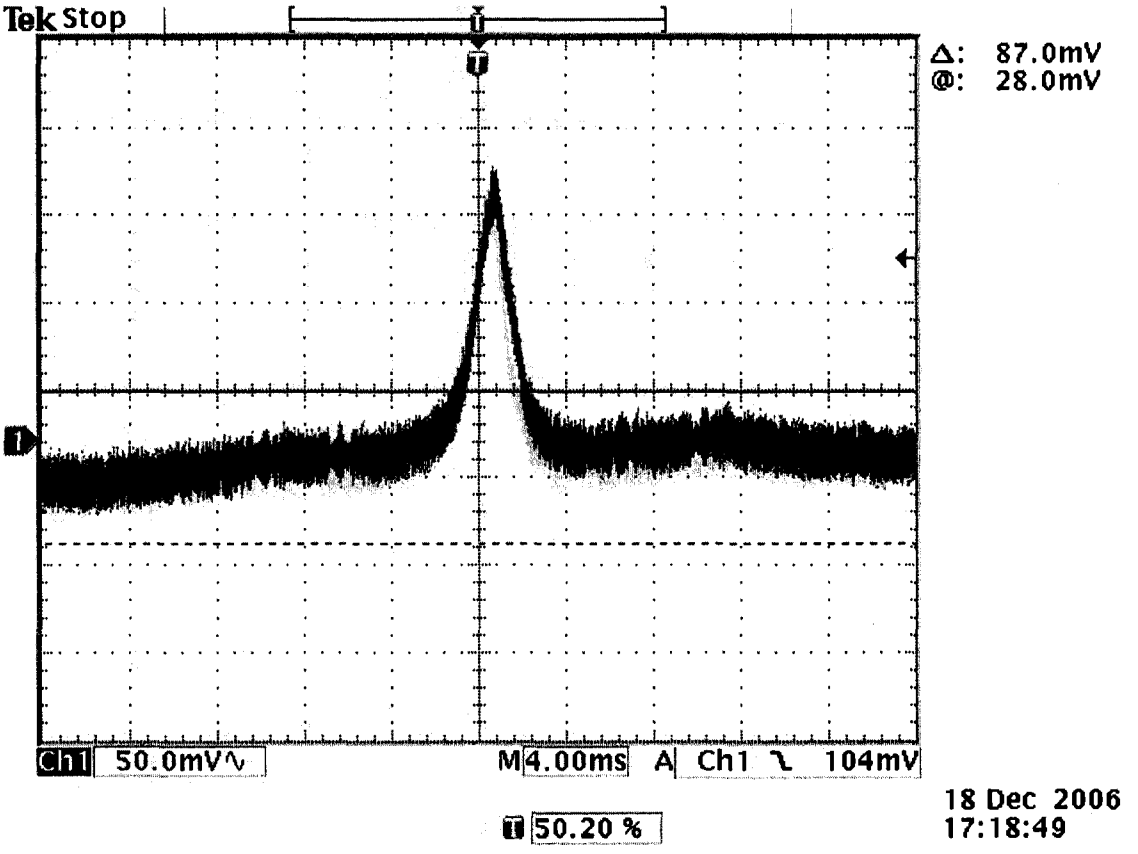

FIG. 19: Saturated absorption signal for Ar*.

Research Systems SR830-DSP lock-in amplifier with a 10 kHz reference signal modulating the ECDL current.

The MOT will optimize when the trapping laser is fixed at -2Γ_{Ar*}, ~11 MHz red detuned of the atomic transition and for the velocity distribution in the Ar* beam, slowing works well at -29Γ_{Ar*}, ~160 MHz red detuned (see Equation 70). Because Ar has no nuclear spin, there is no hyperfine splitting, denoting that the reference absorption line used for locking must be exactly that of the $4s[3/2]_2$ to $4p[5/2]_3$ transition, and all of the frequency shifting needs to be done with AOMs. To do this, the master ECDL is shifted just prior to the SAS by +80 MHz. Locking the master with a frequency shift means the master laser light injection locking the slaves is actually at -80 MHz. Slave 1 will be dedicated as the slowing laser for the Ar* Zeeman slower. To reach the ~160 MHz required, a second AOM will shift the slave laser light another -80 MHz where it is then coupled into a Thorlabs P3-4224-FC5 fiber optic and sent to the science chamber. The other slave, slave 2, is then dedicated as the cooling and trapping laser that will form the Ar* MOT. To reach the required -11 MHz, this slave laser also passes through an AOM, shifting the light +69 MHz from -80 MHz to -11 MHz, after which it is coupled into a Thorlabs P3-4224-FC5 fiber optic by a C110 f=6.24 mm lens and sent to the science chamber.

The remaining light not used for obtaining the SAS signal will be used as a probe beam for absorption imaging.

III.5.3 Photoassociation Lasers

In order to extract a meaningful spectra from the photoassociation of Ar*, the probe laser beam responsible for the observed photoassociation needs to produce a narrow linewidth, at a controlled frequency, and be capable of scanning over frequency ranges of >10 GHz with stable output powers. Additionally, the laser frequency needs to be actively monitored such that the frequency is known on the MHz level. For the PA experiment, two separate laser systems were employed, mainly for reasons of convenience, output power, and confidence in the spectroscopic results. The first laser system described is that of semi conducting diode lasers, very similar to those for the trapping lasers for Ar* as previously discussed, but designed for long scans in frequency. The development of this laser system was experimental and was employed for the conveniences of minimal start-up time and robust performance. This laser system has had many developments in the time that the experiment was run and has

proved to be quite reliable. The second laser system to be described is that of an 899-01 Coherent Ti:S ring laser, pumped by a Coherent Ar ion laser and modified for scanning control. This laser was employed to reach higher laser output power for the probe beam and to ensure confidence in spectroscopy results by reproducing spectra taken by the other laser system. Both of these laser systems are further describe in sections below.

Both independent PA laser systems were aligned into the same frequency diagnostics where the laser frequency and spectrum profile could be monitored. To monitor the frequency, four diagnostics were used including a ~300 MHz Fabry-Perot interferometer, a 10 GHz thick etalon, a Burleigh WA-1000 wavemeter with 300 MHz resolution, and a saturated absorption spectrometer of an Ar* vapor cell for absolute frequency reference. With exception of the WA-1000 wavemeter, each diagnostic uses photodiodes whose current signal is recorded by the Lab View data acquisition program. The WA-1000 is directly networked to the data acquisition computer via RS-232 serial communication where the Lab View program communicates and records the current frequency at regular intervals. The laser spectrum is monitored on a Burleigh spectrum analyzer to ensure single-mode operation, but the signal is not recorded. The Fabry-Perot interferometer was calibrated using the ^{85}Rb saturated absorption spectrum where the free spectral range of the interferometer was found to be FSR=292 MHz.

Diode Lasers

The diode laser system for the PA probe beam consists of two semi-conducting diode lasers in Master-Slave configuration, and designed to scan >10 GHz continuously with stable, reproducible frequency control and laser output power. To accomplish this, the Master diode laser extended cavity was constructed in Littman-Metcalf geometry, with cavity length of ~ 9 cm and a free spectral range (FSR) of ~1.6 GHz. The cavity consists of the diode laser, a 1200 lines/mm diffraction grating and a PZT mounted mirror used for fine tuning the laser frequency. By scanning the PTZ alone, the Master laser was found to only scan 1.6 GHz (the cavity FSR) before mode-hopping. To extend the scanning range of the Master laser, a technique developed by Repasky *et al.* [48] was used, which is described in detail in the appendix of this thesis. Using this technique, the Master laser was able to scan >20 GHz mode-hop free. The Master laser was then sent to the Slave laser for injection locking where the injection

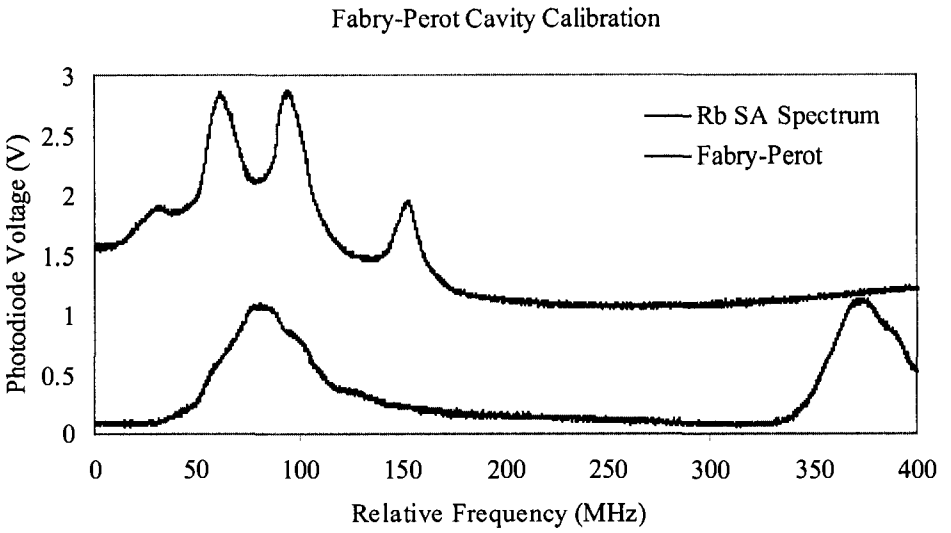

FIG. 20: A plot of the output of the Fabry-Perot cavity and a Rb saturation absorption spectrometer as a laser is scanned.

power of the master laser was controlled by a $\lambda/2$ waveplate and a polarizing beam splitter. The excess Master laser that was not used for injection locking the slave was aligned for beam diagnostics including the ~300 MHz Fabry-Perot interferometer, the 10 GHz etalon, the wavemeter and the Ar* saturated absorption spectrometer. The beam path geometry for this laser system is shown in Figure 21.

The injection locked Slave laser is then sent through an optical isolator and an AOM running at 80 MHz where the first order diffraction is coupled into a fiber optic to be transported to the science chamber. The switching and power of the slave laser to the first order is controlled by control of the RF signal being sent to the AOM. Here again, much like the behavior of the Master, the Slave laser alone can only follow the master single mode for <1 GHz range. To allow the Slave to follow the master for the full range of the scan, an extension of the technique used for extending the scanning range of the Master laser was developed and used for the Slave laser. The details of the techniques used to extend the mode-hop free scanning range of the Slave laser are also discussed in the appendix of this thesis.

Ultimately, this laser system would produce ~40 mW of laser power at the MOT

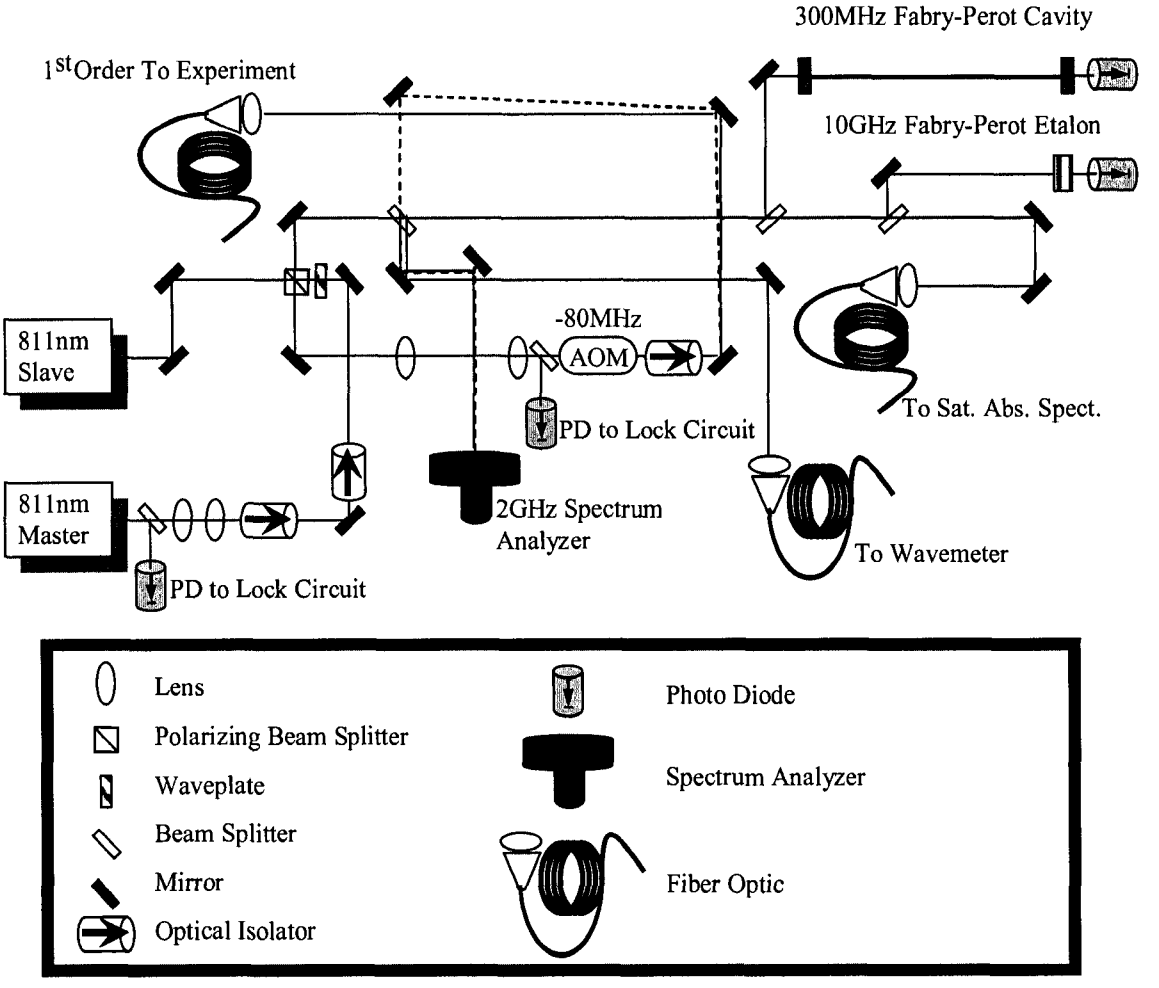

FIG. 21: Schematic of the optical path of the photoassociation probe laser diodes.

site, scannable over a range of >10GHz and high reproducibility. Eventually, with the introduction of a higher power Slave laser, a maximum probe beam laser power of ~100 mW at the MOT was obtained.

Titanium:Sapphire and Ar Ion Lasers

The Titanium:Sapphire (Ti:S) laser is Coherent 899-01 ring laser pumped by a Coherent Innova 300 Ar Ion laser, running multi-line in the visible. (It should be noted that during the course of these experiments, the Innova 300 Ar Ion laser developed power limitations and high frequency jitter, which required the replacing of pump laser source from the Innova 300 with a 90C Argon ion laser on loan from Dr. Havey.) Originally, this 899-01 Ti:S was a broadband laser source, tuned only by discrete, ~0.5 nm mode hops of the three-plate birefringent filter and lacked the intercavity optical components to scan seamlessly. For the photoassociation experiments, the laser is required to continuously scan >10 GHz, mode hop free, and with $\leq$1 MHz linewidth. To accomplish this, various intercavity components and a controller were either borrowed or purchased to modify the 899-01 Ti:S to a narrowband, scanning ring laser (similar to the 899-21 model). These components include: a galvo controlled intercavity assembly (ICA) of a thin and thick etalon, a galvo controlled Brewster plate (woofer), a PZT mounted cavity folding mirror (tweeter), a thermally stabilized reference cavity assembly (RCA), and Coherent 699 control box. With all of these components properly installed and integrated, the 899-01 modified laser is capable of scanning continuously over a ~30 GHz frequency range with high reproducibility. With 6 W of pump laser power, the Ti:S would typically produce ~500 mW of narrowband laser light as measured directly outside the output coupler.

Visually represented in Figure 22, after the Ti:S output laser light exits the cavity, the laser passes through a -40 dB optical isolator where it continues on to a beam splitter where ~5% of the light is directed towards the laser diagnostics and the other ~95% remains to be used in as the PA probe beam. The beam directed toward the laser diagnostics first passes through a glass beam splitter directing ~10% of this light to the Burleigh WA-1000 wavemeter by coupling into a fiber optic. The remainder of this light is then split twice, directing ~10% of the remaining light into the ~300 MHz Fabry-Perot interferometer, ~10% into the 10 GHz thick etalon. The remainder of this light is then coupled into a fiber optic and transported to an Ar* saturated absorption spectrometer.

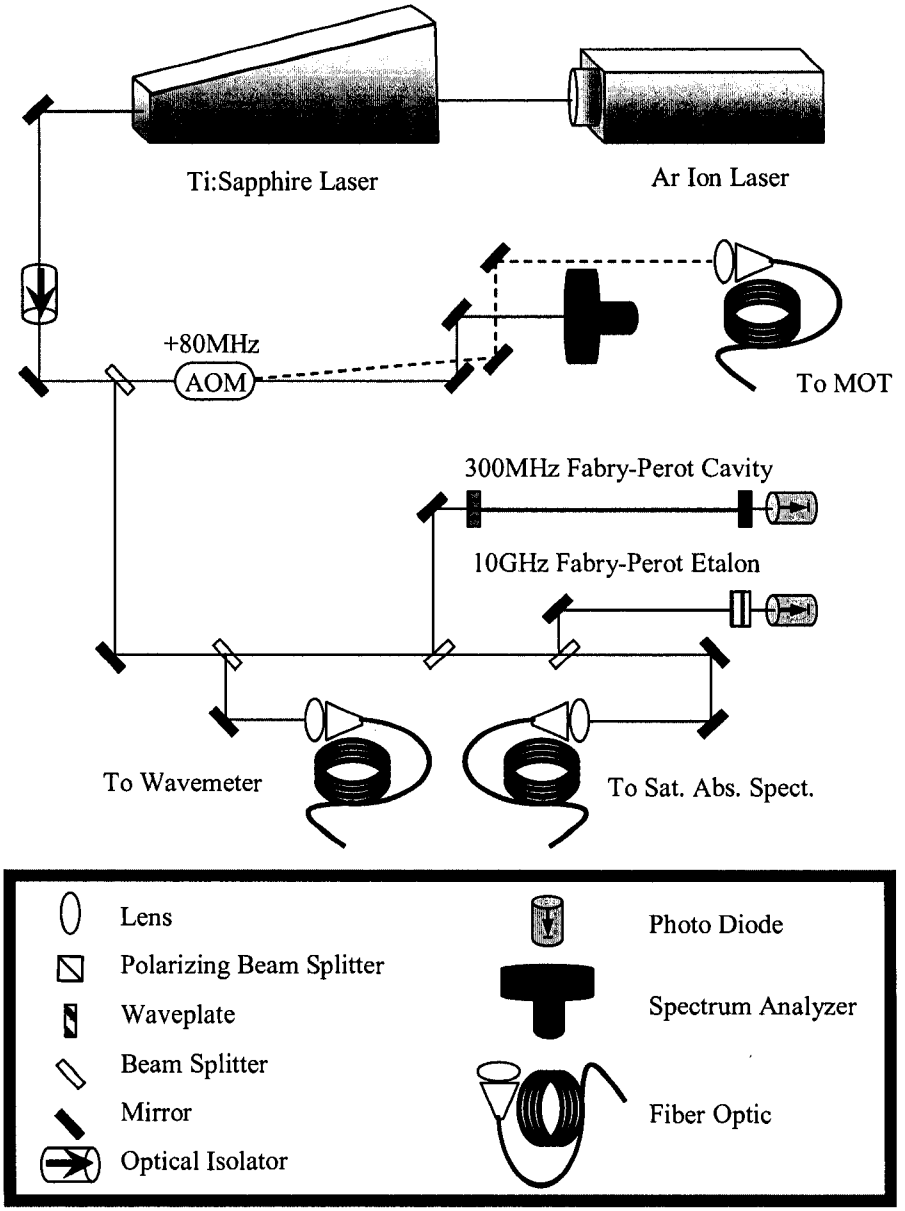

FIG. 22: Schematic of the optical path of the photoassociation probe Ti:S laser system.

The majority of the laser light that passes through the first beam splitter then passes through an AOM running 80 MHz for optimal diffraction to the first order which is coupled to a fiber optic and transported to the science chamber to act as the PA probe beam. By controlling the power of RF signal operating the AOM, the efficiency in diffraction to the first order can range from ~0-75%. Maximum power at the science chamber where the PA beam is delaunched from the fiber is ~125 mW.

III.6 DETECTION

III.6.1 Channeltron Electron Multiplier

As aforementioned, the science chamber has been outfitted with two ion detectors. One is a Channel Electron Multiplier (CEM) from Dr. Jsutz model KBL-10-RS wired for detecting ions. The CEM is powered by an SRS PS350 high voltage power supply dialed to 2500 V. Under these conditions, the gain for the CEM is 10^8 resulting in a 4 ns, 5 mV pulse when an ion is detected and has a maximum count rate of 100 kHz before a drop in the output peak voltage per pulse is observed. Here, a 2-3/4" conflat flange with high voltage insulated feed-throughs has been modified to support a custom designed mount for the CEM. The CEM is mounted at 90 degrees to the Ar* atomic beam. Due to the 11.6 eV of internal energy of the Ar* atom, the CEM will produce a pulse as the Ar* atom quenches on the surface of the cone, adding to the background noise. Since Ar* is electronically neutral, ballistic shielding is sufficient to decrease the number of background counts due to the atomic beam. A grounded, stainless steel, cylindrical shield surrounds the entire CEM reducing the number of background counts from 10 kHz to 1 kHz. Once installed in the science chamber, the cone of the CEM lies ~3 cm from the center of the MOT. This proximity allows for an ion detection efficiency of near unity. If need be, the CEM is mounted such that the circuit can be externally changed from ion detection to electron detection with no need to remove the flange and break vacuum.

III.6.2 SRS RGA200

The second ion detector is an SRS RGA200 residual gas analyzer shown in Figure 24. This detector combines a qaudrupole mass spectrometer (QMS) with an ionizing filament, capable of filtering ions by atomic mass with 0.1 AMU precision and a range from 1-200 AMU. In this configuration, the filament would ionize the residual

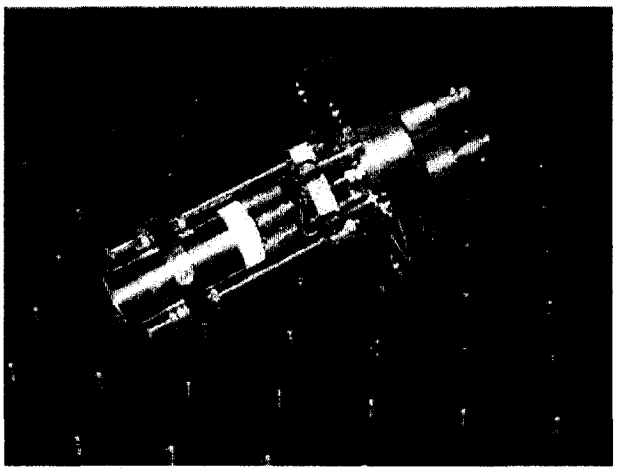

FIG. 23: A picture of channeltron electron multiplier prior to insertion into the science chamber.

gas in the science chamber, accelerate the ions into the QMS where as a function of atomic mass may be detected. This is useful for determining ambient gas pressure and composition, however the filament drastically increases losses in the MOT and therefore can not be used simultaneously with the running experiment.

However, with the internal energy of Ar*, one of the leading causes of trap loss for the Ar* MOT is ionizing collisions. To collect and mass-sort these naturally occurring ions, the SRS RGA200 has been modified to run with the filament off. To aid in accelerating these ions into the QMS with the proper energy, a set of ion optics is installed, designed in the program SimIon which models the ions trajectories.

By using the SimIon simulations, the voltages for each ion optic in Figure 25 are optimized. These values are P1=+1600V, P2=-200V, F1=-130V, and F2=-150V. Though the ion detection efficiency is roughly 1 in 1000, the ability to discriminate ion mass is critical to determining what ion species are created in the MOT.

III.6.3 Photomultiplier Tubes

In addition to detecting ions, a common method to characterize a MOT is by determining atom number by florescence detection using photomultiplier tubes (PMT). PMTs are photosensitive detectors that produce a small electric current proportional to the number of photons collected. As atoms are cooled and trapped in a MOT, the

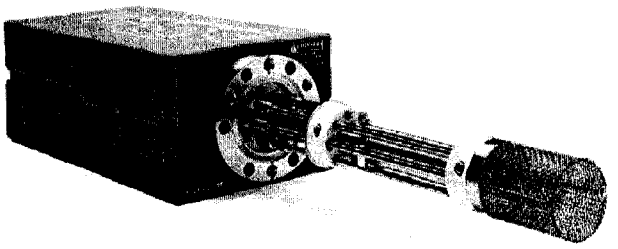

FIG. 24: A picture of the SRS RGA200 residual gas analyzer.

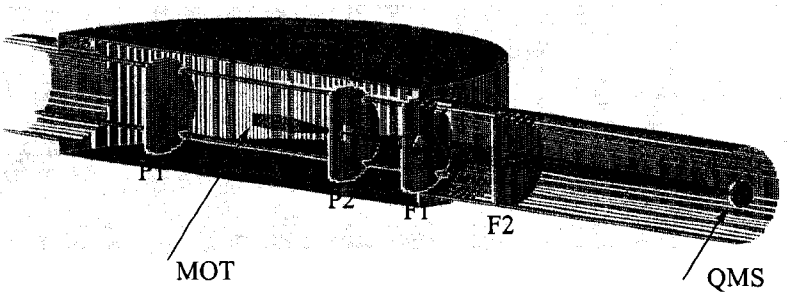

FIG. 25: An image of ion optics trace program in SimIon.

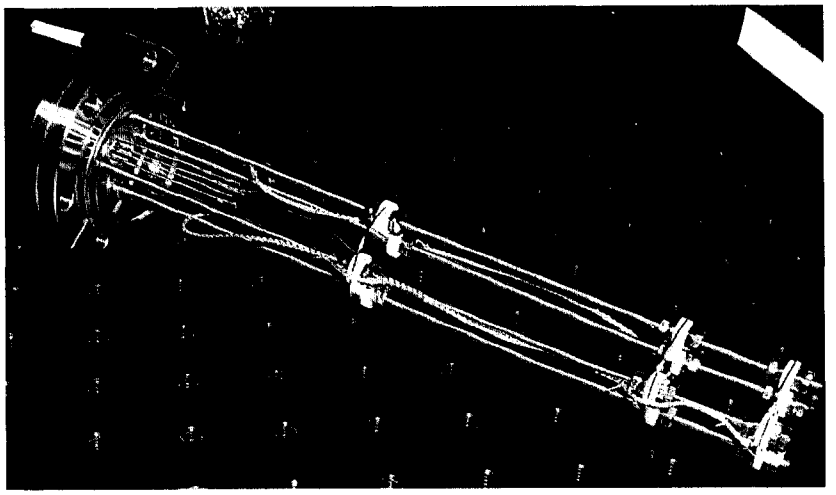

FIG. 26: A picture of ion optics prior to insertion into the science chamber.

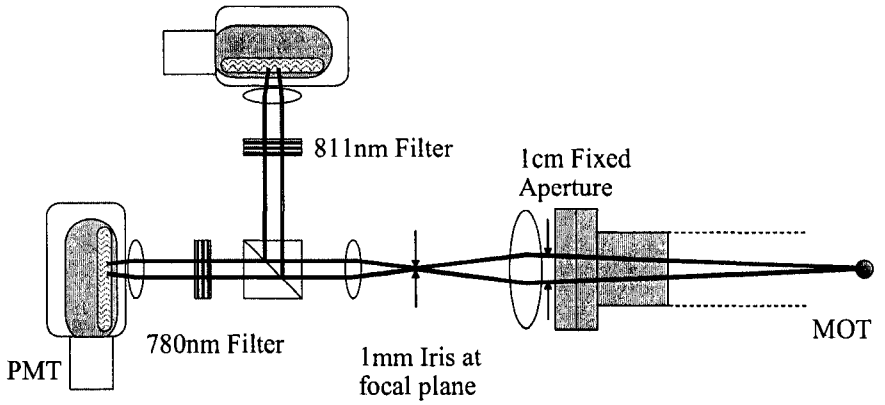

FIG. 27: Schematic of the PMT apparatus for monitoring fluorescence from the Rb and Ar* MOTs.

trapping laser light is scattered isotropically in 4π sr. By collecting a known solid angle of the scattered photons on the PMT and by knowing the scattering rate of the MOT among other factors, the number of atoms in the MOT can be determined generally to within a factor of two. Since two species are to be trapped in this experiment at two different trapping laser wavelengths (811 nm and 780 nm), it is possible to use a narrow bandpass filter to monitor the fluorescence from the Ar* and Rb MOTs individually.

As shown in Figure 27 in this apparatus, a 2" lens (f=75 mm) is placed directly outside one of the uncoated windows of the science chamber to serve as a collection lens. This lens is fitted with an aperture of diameter 1 cm. By knowing the area of the aperture and its distance to the center of the science chamber, a collection solid angle can be expressed as $\pi r^2/4\pi R^2$ where r is the diameter of the aperture and R is the distance between the aperture and the MOT. The scattered light is then imaged onto a translating pinhole to reject unwanted background light. A lens (f=50 mm) then collimates the light where it is split by a beam splitter. The light that passes through is then subject to a Newport 10LF10-780 780 nm narrow bandpass interference filter (FWHM=10 nm) and is then partially focused by a lens (f=55 mm) onto the active region of the PMT, model Hamamatsu R928 on a HC-123 base. Likewise for the beam reflected by the beam splitter is then subject to a 811 nm narrow bandpass interference filter (FWHM=10 nm) and is then partially focused by a lens (f=55 mm) onto the active region of the PMT. Each filter suffers a 50 percent

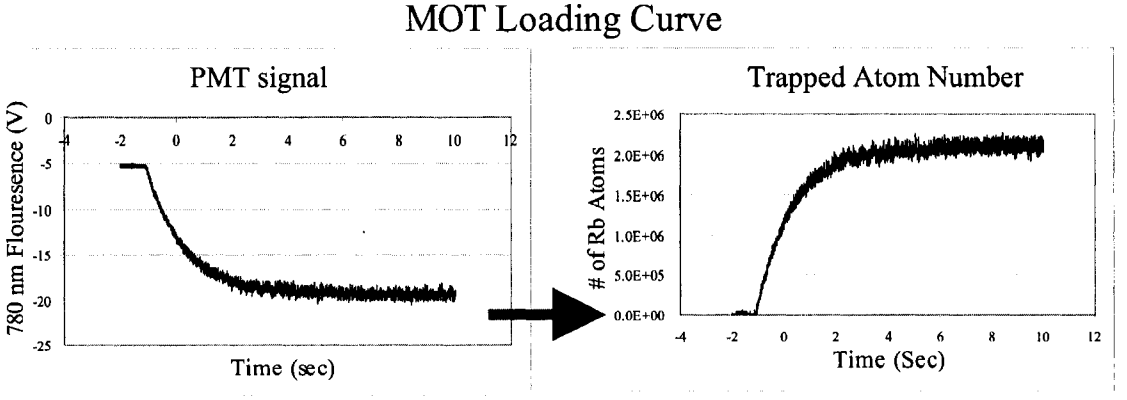

FIG. 28: By using a conversion factor determined by Equation 71, the PMT voltage resulting from the collected MOT florescence can be converted into number of trapped atoms.

loss in transmitted light. The quantum efficiency (qe) of a PMT is dependent on the wavelength of detected light. For the 811 nm and 780 nm light, the qe is $\sim 2\%$ and $\sim 2\%$ respectively. As the photon is detected on the PMT, an electron is released where an avalanche effect results in a gain of 10^7 when the base voltage is it's typical 1.0 kV. With all of these factors in consideration, the expression for the number of atoms of a particular species in terms of PMT electron current is

$$N_a = \frac{I_{PMT}}{L_F L_L L_B \Omega (qe) \Gamma} = I_{PMT} L_{eff} \tag{71}$$

where I_{PMT} is the current produced from the PMT, L_F, L_L and L_B are the losses due to the interference filter, lens and beam splitter, respectively, Ω is the solid angle fraction, and Γ is the scattering rate. If, as in many cases, an I to V converter is used to monitor the fluorescence signal, the gain of that circuit will need to be included in the conversion. Illustrated in Figure 28, this conversion defines a simple relation to convert PMT volts to number of trapped atoms.

III.6.4 Research CCD Camera

For MOT characterization, two imaging techniques are used: Fluorescence Imaging and Absorption Imaging. Both of these techniques used a Princeton Instruments research grade CCD camera.

Fluorescence imaging is a method by which an image of the MOT is projected onto the CCD array of a camera for a short, known amount of time. When the MOT trapping lasers are on, the MOT naturally scatters light isotropically at a certain scattering rate. By taking an image on a research grade CCD camera and knowing the scattering rate, quantum efficiency of the CCD array, the exposure time and the magnification of the image, the MOT size, atom number, and hence density profile can be determined.

The CCD camera was mounted on the optical table aligned with one of the 1.5" windows of the science chamber. A converging collection lens was positioned near the window such that a 1 to 1 relay image was focused onto the CCD array of the camera. Protecting the CCD array is a TTL controlled mechanical shutter with a $\sim$100 μsecond response time. While the trapping lasers are fully on and the MOT is loaded to a steady number of atoms, the CCD array is charged and the mechanical shutter opens for 5 milliseconds and then closes again. The data from the CCD array is recorded as an image file on an interfaced computer. From here, the software can produce an ascii tab delimited array of values from the image where each value corresponds to the intensity of light a single pixel has experienced. Figure 29 is a typical florescence image of a MOT. From the ascii file, a cross-sectional profile of the pixel values will display the 1 dimensional intensity profile for the MOT which can be modeled to determine volume and atom density. The atom density profile for the MOT in this regime of trapping light intensities is very close to Gaussian and the image profile can be fit to

$$n(r,t) = n_o(t)e^{-2[r/\omega(t)]^2} \tag{72}$$

Where for a steady MOT, $n_o(t)$ and $\omega(t)$ are constant in time. By fitting this function to the profile by a least root mean squares fit, r, the width of the MOT and $n_o(t)$, the maximum density (really the intensity), can be determined. However, using fluorescence imaging was found to give slightly inconsistent results for density and atom number, partially due to inconsistent shutter speeds leading to uncertainty in knowing exposure times. Since the shape of the profile is largely unaffected by exposure time, the shape, size and position of the MOT are reasonably accurate using this method.

A much more accurate technique for characterizing the MOT is that of absorption imaging. In this method, the shadow of the MOT is effectively imaged onto the CCD

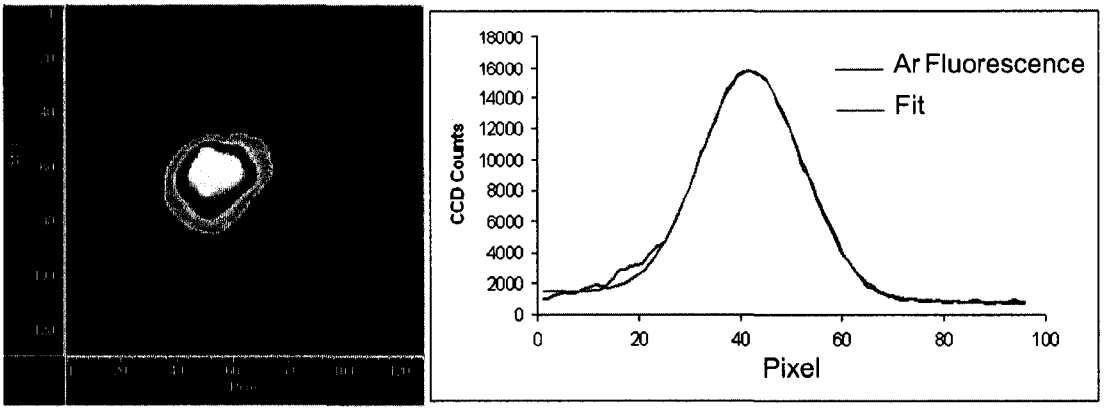

FIG. 29: On the left, a false color fluorescence image of the Ar* MOT (The various colors differentiate relative intensities) and on the right, a cross section of the florescence image, fit to a Gaussian profile of Equation 72.

array of the camera. Here, the MOT is fully loaded by the trapping lasers. The trapping lasers are briefly shut off via AOM's for 100 atomic lifetimes and the MOT is allowed to decay to the ground state. In the 3 μs for this to happen, the MOT does not fall (due to gravity) or ballistically expand (due to a temperature distribution) appreciably. At this time, a very weak collimated probe beam, tuned on resonance and centered on the MOT is turned on for $\sim$100 μseconds. As the beam passes the MOT and leaves the science chamber, it is then shown directly on the CCD array of the research camera. The probe beam itself needs to be sufficiently low in intensity $I \sim 10^{-3} I_S$ as to not appreciably disturb the MOT and not to saturate the CCD array. The spatial waist of the probe beam needs to be 10-100 times that of the MOT ($\omega \sim$1 cm) such that the wavefront at the MOT site is uniform and flat. The resulting image collected by the CCD camera appears to be that of the shadow of the MOT, as shown in Figure 30, where the resonant probe beam is partially absorbed by the atoms in the MOT. The absorption rate of the atoms in the MOT can be determined through Beer's Law:

$$\frac{dI}{dz} = -\sigma(\delta)_{eg} n I \tag{73}$$

where $\sigma(\delta)_{eg}$ is the cross section for absorption at detuning from resonance $\delta = \omega_a - \omega_P$, and n is the density distribution along the Z or axial direction along the

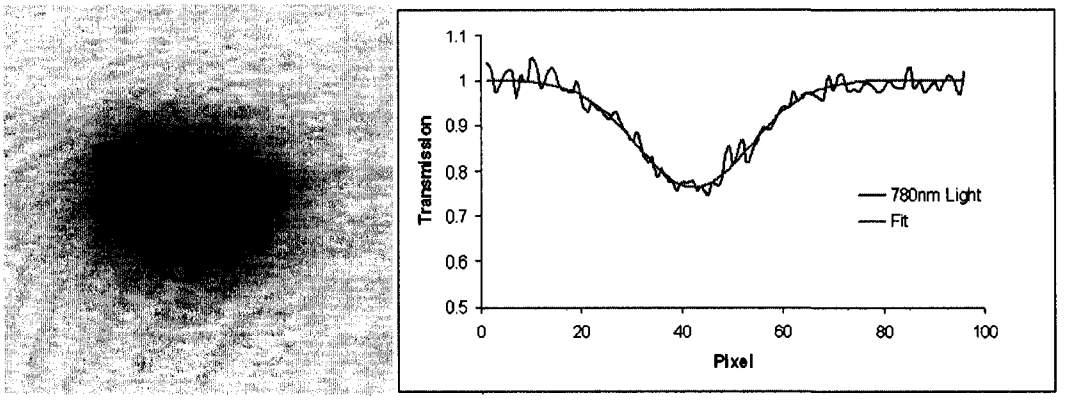

FIG. 30: On the left, an absorption image of the Rb MOT and on the right, a cross section of the image fit to a Gaussian profile of Equation 72.

probe beam.

III.6.5 Observational CCD Cameras

For strictly observational purposes, two CCD security cameras, Sanyo VCB-3512, are used to view the MOT florescence by displaying the video image on a TV screen. Though this is by no means capable of making a quantitative measurement, the economic CCD array of the cameras is much more sensitive to the IR scattered light from the MOT than the human eye and in day to day experience, is a useful tool in evaluating MOT position, shape, stability and presence. The two cameras are aimed at perpendicular vantage points so all projections of the MOT shape can be observed.

III.7 DATA ACQUISITION AND SYSTEM CONTROL

As with any experiment, data acquisition and system control are vital. The methods for recording data need to be organized, coherent, and dependable while the system needs to be controlled in a reproducible, precise way. Often these methods vary with the demands and complexity of the experiment. For the first experiment discussed in this thesis, the Rb-Ar* trap loss, the acquisition and control needs are fairly simple. To control the loading of each individual MOT, the trapping light for each species was blocked or unblocked manually. The data acquisition for the trap loss experiment

is schematically represented in Figure 31. The fluorescence of each MOT, collected by an appropriately filtered PMT, was monitored on a multi-functional TEK3014B oscilloscope (Channels 1 and 2). The scope has the ability to run in "scroll mode" which allows for the recording of voltage values over a maximum time scale of ~100 seconds. This mode is used when recording the transient MOT loading curves which are later exported in a comma separated value (CSV) format and mathematically modeled to determine the α and β trap loss coefficients for each MOT. The scope also can do active averaging of a voltage signal. Because the typical trap loss in either species MOT due to the presence of the other is roughly $\sim 5\%$, which is comparable to the signal noise, it is beneficial to take a rolling average over 128 data points when conducting this measurement. Both measurements of the transient loading curve and the averaged interspecies trap loss, the recorded data is exported as a CVS file then imported and analyzed in software on a PC. In both cases, the scope impedance was 1 MΩ.

To characterize the Rb and Ar* MOTs, the research grade CCD camera was used. To control the camera and the system for imaging, a computer outfitted with imaging software was connected to the camera controller via a serial connection. In order to have the correct experimental conditions for the fluorescence and absorption imaging, a Quantum Composers 1600 series pulse generator was used to control the camera shutter, the probe beam (if used) and the trapping lasers by switching on or off the respective AOMs. The computer was configured to prime the CCD camera and wait for a TTL pulse from the manually triggered pulse generator to open and close the shutter, after which the data was then sent to the computer from the CCD camera. For fluorescence imaging, the MOT to be imaged is loaded and the computer primes the CCD camera. The pulse generator then sends a TTL pulse to the camera to open and close the shutter (the TTL pulse width controls the length of the exposure). Here all trapping lasers are left on and the probe beam is never turned on. For absorption imaging, the method differs slightly from that of fluorescence imaging and the pulse generator is now responsible for turning off the trapping lasers, opening the camera shutter, switching on and off the probe beam, and closing the shutter. After the exposure is complete, the data is again sent to the computer.

The SRS RGA200 residual gas analyzer is also networked to the computer. Here the serial RS-232 connection uses RGA2000 software acquired from SRS to control the tuning and detection mode of the RGA. The RGA then sends data back to

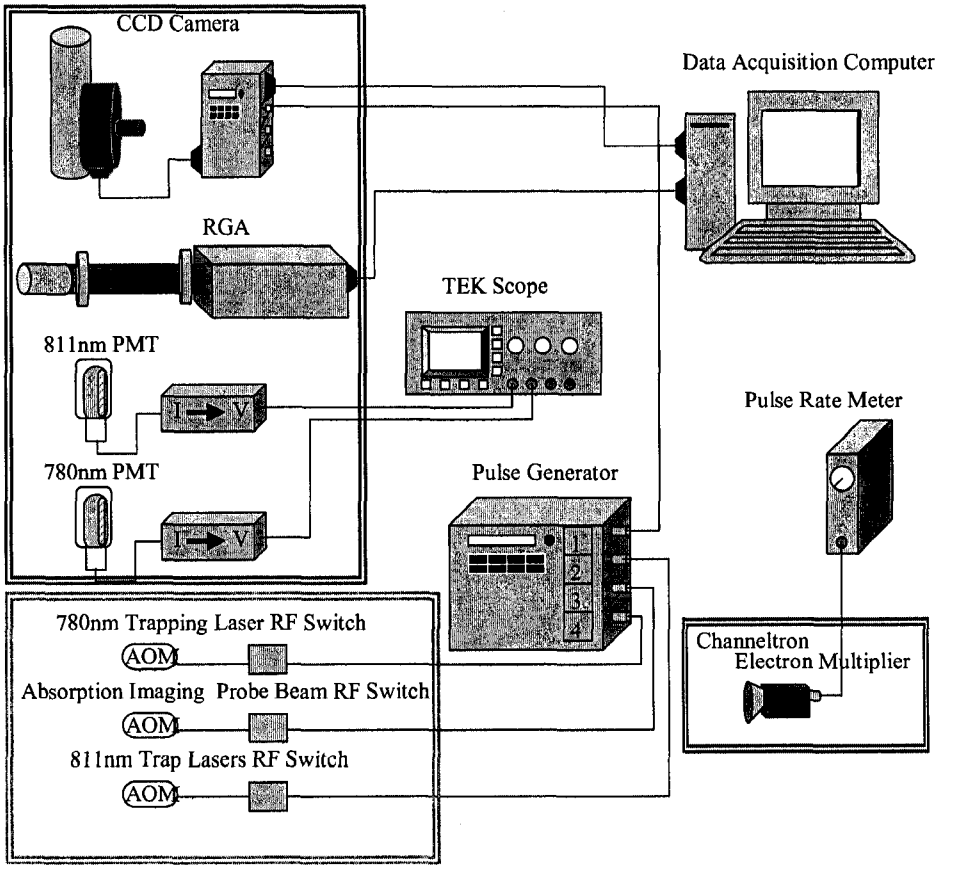

FIG. 31: The data acquisition system for the Rb-Ar* trap loss experiment.

the computer where the software plots the data in an appropriate manner. With exception of the custom switches installed on the RGA to run in a non-ionizing QMS mode, the software completely controls the RGA. Because the throughput of the RGA in QMS mode is 1 to 1000 or less, the RGA is run independently and was never synchronized to the other aspects of the experiment.

For the photoassociative spectroscopy of Ar* experiment, the methods for data acquisition and system control differ to better facilitate the experimental needs. Since spectroscopy of the system is going to be performed, the spectroscopy laser will need to be closely monitored as well as collecting specific data from the MOT as a function of the lasers frequency. Schematically represented in Figure 44, the data acquisition system is more integrated as well as automated. Summarizing the detailed information of the experiment in Chapter V, for a given frequency of the PA laser, the previously loaded MOT is briefly turned off, the PA beam turned on, the gated ions produced by the probe beam are collected in channels A of the photon counter, the probe beam is switched off, the trapping lasers are switched back on, and the gated ions produced during the MOT-on phase are collected in channel B of the photon counter as a background/reference signal, and the sequence is repeated. (Ions are continually being physically collected by a CEM in the science chamber. The resulting voltage pulses are sent to channels A and B where they are discriminated by arrival time (gate) and peak height). It is the quantum composers pulse generator that controls the probing sequence for the experiment by supplying a TTL pulse to trigger the photon counter and subsequent pulses to each of the AOM switches for the trapping, slowing, and PA probe lasers. The photon counter will collect and sum the ions collected over 2000 cycles upon which the photon counter will store that data (channel A and B total counts) in temporary memory and continue counting the next 2000 cycles. A Labview program (see Appendix for details) running on the data acquisition computer is interfaced with the photon counter via rs-232 serial cable and systematically checks to see if that data is available. If it is, the Labview program accesses the data from the photon counter (which erases it from the photon counter memory) and stores it in an array. Once this task is complete, Labview then begins the tasks of communicating with the interfaced Burleigh-1000 wavemeter to collect the value of the laser frequency in GHz, and also reading in the values on four voltage channels on the NI-DAQ board. Each voltage channel is connected to the voltage output of either a PMT for monitoring MOT fluorescence or a 300-MHz

Fabry-Perot cavity, a 10-GHz etalon, and saturated absorption spectrometer which monitors the behavior of the PA probe laser. Once all of these values are collected by the Labview program, they are stored in an array of arbitrary length and the process repeats until a user boolean is toggled which writes the array to a file in tab delimited format. As the probe laser is slowly scanned over a given range, the resulting file contains values for all monitored values in chronological order where a photoassociative spectrum can be made.

CHAPTER IV

TRAP LOSS IN A RB-AR* DUAL SPECIES MOT

As previously discussed in the introduction of this thesis, a growing interest in heteronuclear, atomic interactions at ultracold temperatures has served as motivation for the experimental investigation of the Rb-Ar* dual species MOT. The first of its kind to trap an alkali (Rb) and a metastable rare gas (Ar), this apparatus has set the stage for a set of experiments leading toward the ultimate goal of performing spectroscopy of ultracold, photoassociated RbAr ground state molecules. The first experiment is to determine the heteronuclear trap loss rate coefficient β' for each species in the presence of the other.

IV.1 EXPERIMENTAL TECHNIQUE

Detailed in section II.5, the loss of atoms in a MOT arise from collisions between cold trapped atoms within the MOT as well as collisions between trapped atoms and thermal background atoms. If a second MOT of a different species atom is present, collisions between the two species can result in trap loss as well. These losses can be quantified by considering the MOT load rate equation, repeated below, where γ, β, and β' are the trap loss coefficients for background gas collisions, homonuclear cold collisions, and heteronuclear collisions, respectively. Ultimately, it is the heteronuclear trap loss coefficients for Rb, β'_{Rb-Ar*}, and Ar*, β'_{Ar*-Rb}, that are of interest.

$$\frac{dN_{Rb}}{dt} = L - \gamma N_{Rb} - \beta_{Rb} \int_v n_{Rb}^2 d^3r - \beta'_{Rb-Ar*} \int_v n_{Rb} n_{Ar*} d^3r \tag{74}$$

In order to determine the interspecies trap loss coefficients, the trap loss in a single species MOT must be first characterized. To do this, the initial condition of $N(t=0) = 0$ is imposed on

$$\frac{dN_{Rb}}{dt} = L - \gamma N_{Rb} - \frac{\beta_{Rb} N_{Rb}^2}{\omega_{Rb}^3 \pi^{3/2}} \tag{75}$$

which has the analytic solution of

$$N(t) = N_0 \left[1 - \frac{(1+\xi)\exp(-t/\tau_L)}{1+\xi\exp(-t/\tau_L)} \right] \tag{76}$$

The loading curve of the single species Rb MOT atom number is recorded via fluorescence and imported into a computer where a program fits Equation 76 to extract γ_{Rb} and β_{Rb}. With these values now determined, the interspecies trap loss coefficient can be solved for. To extract β'_{Rb-Ar*}, the Rb MOT is considered in its steady state for both the single species and the dual species load rate equations

$$\frac{dN_{Rb}}{dt} = 0 = L - \gamma N_{Rb} - \frac{\beta_{Rb} N_{Rb}^2}{\omega_{Rb}^3 \pi^{3/2}} \tag{77}$$

and

$$\frac{dN'_{Rb}}{dt} = 0 = L - \gamma N'_{Rb} - \frac{\beta_{Rb} N'^2_{Rb}}{\omega'^3_{Rb} \pi^{3/2}} - \beta'_{Rb-Ar*} N'_{Rb} N_{Ar*} \left[\frac{2}{(\omega'^2_{Rb} + \omega^2_{Ar*})\pi}\right]^{3/2} \tag{78}$$

where N'_{Rb} is the number of atoms in the Rb MOT while Ar* is present. By equating these two expressions, β'_{Rb-Ar*} can be solved for:

$$\beta'_{Rb-Ar*} = \left[\frac{\pi(\omega'^2_{Rb} + \omega^2_{Ar*})}{2}\right]^{3/2} \frac{1}{N'_{Rb} N_{Ar*}}$$
$$\times \left[\gamma(N_{Rb} - N'_{Rb}) + \beta_{Rb}\left[N^2_{Rb}\left(\frac{1}{\pi\omega^2_{Rb}}\right)^{3/2} - N'^2_{Rb}\left(\frac{1}{\pi\omega'^2_{Rb}}\right)^{3/2}\right]\right] \tag{79}$$

Here an analytical solution for β'_{Rb-Ar*} is found in terms of the single species trap loss coefficients, γ_{Rb} and β_{Rb}, the steady state number of trapped atoms N_{Rb}, N'_{Rb}, N_{Ar*} and the Gaussian waists of each MOT ω_{Rb}, ω'_{Rb}, ω_{Ar*} . The reciprocal term β'_{Ar*-Rb} is determined in a similar manner.

Alternatively to this method, it is also possible to determine γ, β, and β' by numerical integration and fitting routines. For this method, Equation 77 for a single species MOT is numerically integrated using a 4th-order Runge-Kutta algorithm. The curve is then fit to an observed, single species MOT loading curve to extract γ and β. In a similar fashion, Equation 78 for the MOT loading in the presence of the other species, is also numerically integrated but with using the previously determined values for γ and β. The curve is then fit to an observed, dual species, MOT loading curve to extract the value of β'.

IV.1.1 Dual MOT Characterization

Regardless of the method used to determine β', it is necessary to characterize each MOT to determine its atom number N, density n_0 and waist ω as well as to confirm

that the MOTs are trapped in the same region since Equations 77 and 78 assume that the MOTs are spatially overlapped.

To measure the atom number, two methods are employed. The first is through fluorescence measurements as described in the PMT section of the apparatus. In review, by collecting the photons scattered by the MOT over some solid angle and knowing the scattering rate at the given trap laser intensity and detuning, the PMT will produce a current proportional to the number of atoms in the MOT. For the Rb MOT, Equation 71 becomes

$$N_{Atoms} = \frac{I_{PMT}}{L_F L_L L_B \Omega (qe) \Gamma} = I_{PMT} L_{eff} \sim 150000 \text{ atoms/V} \tag{80}$$

and for the Ar* MOT

$$N_{Atoms} = \frac{I_{PMT}}{L_F L_L L_B \Omega (qe) \Gamma} = I_{PMT} L_{eff} \sim 100000 \text{ atoms/V} \tag{81}$$

To determine the number of atoms in the MOT given these relations, it would be as simple as reading the value of the voltage produced by the PMT when the MOT is present, but trap laser light and ambient light scattering off the inside of the science chamber produces a background that needs to be accounted for. The true MOT atom number is proportional to the PMT voltage difference between when the MOT is present and when it is not. To conveniently manage this without changing the level of background light, a B-field switcher very quickly can stop or start the 6 Amperes of electrical current running through the anti-Helmholtz coils that create the magnetic field gradient necessary for MOT operation. By turning off and on the B-field, the MOT is also turned off and on. Also, by using this method to monitor MOT atom number, the MOT loading curve can be recorded as a function of time (and later fit to extract trap loss rate coefficients). As earlier stated, the PMT setup for this apparatus has one PMT dedicated for detecting 780±5 nm light for the Rb MOT and another PMT dedicated for detecting 811±5 nm light for the Ar* MOT. This allows for simultaneous monitoring of each individual MOT's atom number. Typically, MOT fluorescence measurements are viewed and recorded on a TEK3014B digital oscilloscope which has the ability to run in "scroll mode" and save and export the voltage measurements in an ascii array.

Alternatively, using the method of absorption imaging (AI), the MOT atom number can be extracted along with the atom cloud density and waist. The probe beam

for AI is typically a few μW of resonant light, collimated in a beam whose waist is $\sim$10 mm and centered on the MOT. An image I_{Back} is taken without the MOT present, but the probe beam is still incident on the CCD array of camera. Another image I_{Dark} is taken where the probe is not turned on nor the camera shutter opened, giving an array of dark counts of the CCD array. Finally an image I_{MOT} is taken with the MOT present. Image data arrays are then processed to give the normalized absorption image shown in Figure 30. A cross section of the data array is then taken through the location of maximum absorption and is fit (RMS) to a Gaussian density profile of Equation 72 where n_0 and ω are fitting parameters. Once n_0 and ω are obtained, the MOT atom number can be estimated by integration. Typically, the method of MOT atom number determined through AI and fluorescence measurements agree to within a factor of 2.

With the MOT atom number, density and volume determined for both the Rb and the Ar* MOTs, the spatial overlap of the two MOTs needs to be confirmed. Spatial overlap of the MOTs is critical to the accurate determination of the β' terms since the interaction depends on each atomic species being in the vicinity of the other where they can interact. Though absorption imaging does individually give spatial detail of where each MOT is relative to the camera and probe beam, it does not allow for the simultaneous measurement of both MOTs since the probe beam needs to be resonant with one atomic transition or the other. To ensure good MOT overlap, fluorescence imaging is also used to image both the Rb and Ar* MOTs simultaneously. Here the image of the MOTs is imaged onto the plane of the CCD array and the shutter to the camera is opened for a specific exposure time. By imaging the Rb MOT alone, the Ar* MOT alone, and the Rb and Ar* MOTs together as in Figure 32, it is clear that the MOTs are well overlapped. This method is performed in two perpendicular directions to eliminate ambiguity due to MOT projections along the imaging axis that can not be detected in the MOT image.

IV.1.2 Observing Trap Loss in the Rb - Ar* MOT

The determination of β' hinges greatly on the ability to measure interspecies trap loss separately from same-species trap loss and trap loss due to background collisions. To do this in a most straightforward manor, the behavior of each MOT alone needs to be directly compared to the behavior of that MOT in the presence of the other MOT. This can be done by either observing a MOT's transient loading curves (with

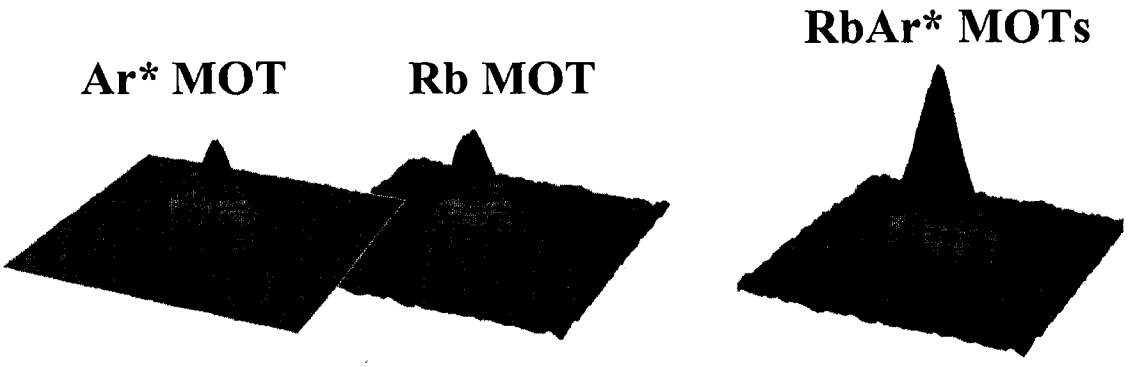

FIG. 32: Fluorescence images of the Ar* MOT alone, the Rb MOT alone and the Rb-Ar* dual MOT ensures good spatial MOT overlap

and without the other MOT present), or by observing the total atom number of a MOT in its steady state (again, with and without the other MOT present).

Since the transient loading curve for either MOT is ~1-4 seconds, the fact that the TEK3014B oscilloscope is capable of recording both PMT channels in a time base where multiple loading curves can be recorded in one array/dataset is taken advantage of. In this fashion, one dataset can contain a few seconds of background measurement (no MOT), a MOT loading curve (one MOT), and a MOT loading curve in the presence of the other MOT (two MOTs). To record the loading curves for the Rb MOT, the scope will record both PMT channels (780 nm and 811 nm). For background light measurement, the trapping (and slowing) lights for each MOT will be on for a few seconds with no B-field on (no MOTs). The trapping lasers for both species are blocked and the B-field is turned back on. Next, recording the Rb MOT loading alone, the 780 nm trapping laser is unblocked and the Rb MOT is allowed to load. The 780 nm trap light is then blocked and the 811 nm light is unblocked and the Ar* MOT is allowed to load. Now with the Ar* MOT present, the 780 nm trap light is unblocked and the Rb MOT is again allowed to load, this time in the presence of the Ar* MOT (see Figure 28). The file on the scope is then saved in ascii to a file for analysis. The same procedure is repeated for the reciprocal measurement for the Ar* MOT.

To observe interspecies trap loss in the MOT steady state, the Rb MOT is allowed

TABLE I: Summary of trap loss coefficients average values [49]

	^{85}Rb	^{40}Ar*
γ	(0.54 ± 0.05) s^{-1}	(0.73 ± 0.26) s^{-1}
β	$(3.7 \pm 1.7) \times 10^{-12}$ cm^3/s	$(5.8 \pm 1.7) \times 10^{-10}$ cm^3/s
β'	$(3.0 \pm 1.3) \times 10^{-11}$ cm^3/s	$(1.9 \pm 0.9) \times 10^{-11}$ cm^3/s

to fully load and the PMT voltage is recorded on the TEK3014B scope where 256 measurements are averaged. This value is subtracted from the background with no MOT for the florescence measurement giving the number of atoms in the MOT. While the Rb is still present and being monitored, the Ar* MOT is allowed to load and the fluorescence measurement is repeated. The difference between the Rb MOT atom number measurements with and without the presence of the Ar* MOT represents observed interspecies trap loss. Though this measurement is conducted when both MOTs are in the steady state, the transient loading curves of the individual MOTs are still recorded so that single species trap loss can still be quantified.

IV.2 ANALYSIS AND DISCUSSION OF RESULTS

When individually loaded, the Rb and Ar* MOTs contain up to 2×10^6 and 5×10^5 atoms at densities of 8×10^{10} and 2×10^{10} atoms/cm^3, respectively, in steady state. By fitting the individual MOT atom loading curves to Equation 77 by a least-squares routine, the single species trap loss coefficients for Rb and Ar* have been determined and are tabulated in Table IV.2. For both the Ar* and Rb MOTs, the values stated in Table IV.2 are with the trapping laser intensities at the maximum values attainable with this apparatus. Where the trap loss term, γ, quantifying background collisions is partial to the experimental apparatus, the trap loss term, β , pertains to the atomic species.

Shown in Figure 33 as function of 780 nm trap light intensity, the value of β_{Rb} varies little over the selected range[49]. When compared to measurements of Wallace *et al.* [50], it is found that the measurements of β_{Rb} for ^{85}Rb are in good agreement as shown in Figure 34.

The β_{Ar} term for ^{40}Ar*, on the other hand, had only been estimated to an order of magnitude. This experiment represents the first homonuclear trap loss coefficient

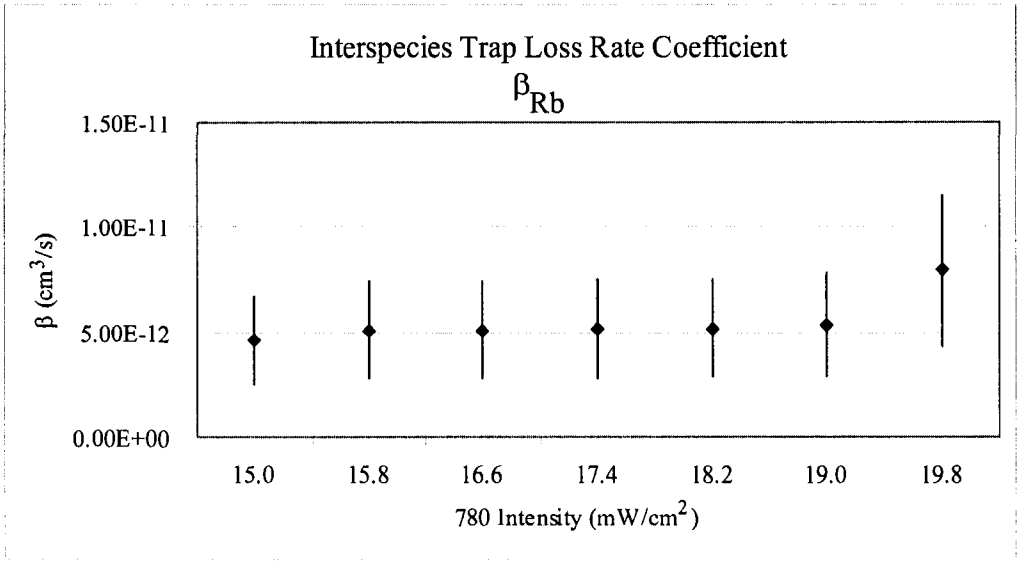

FIG. 33: Plot of β_{Rb} as a function of 780 nm trapping light intensity.

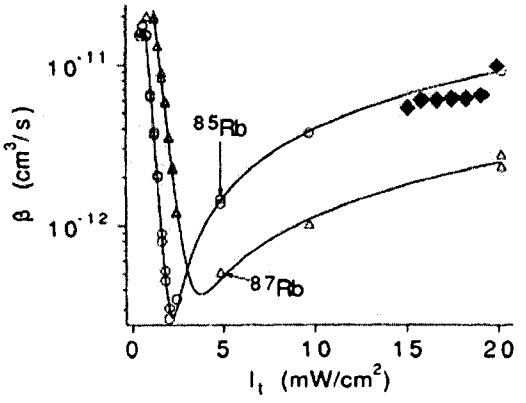

FIG. 34: Values of β_{Rb} obtained from this experiment agree with those of Wallace *et al.*. Here the circles and triangles represent data from Wallace *et al.* and the diamonds represent data from this thesis.

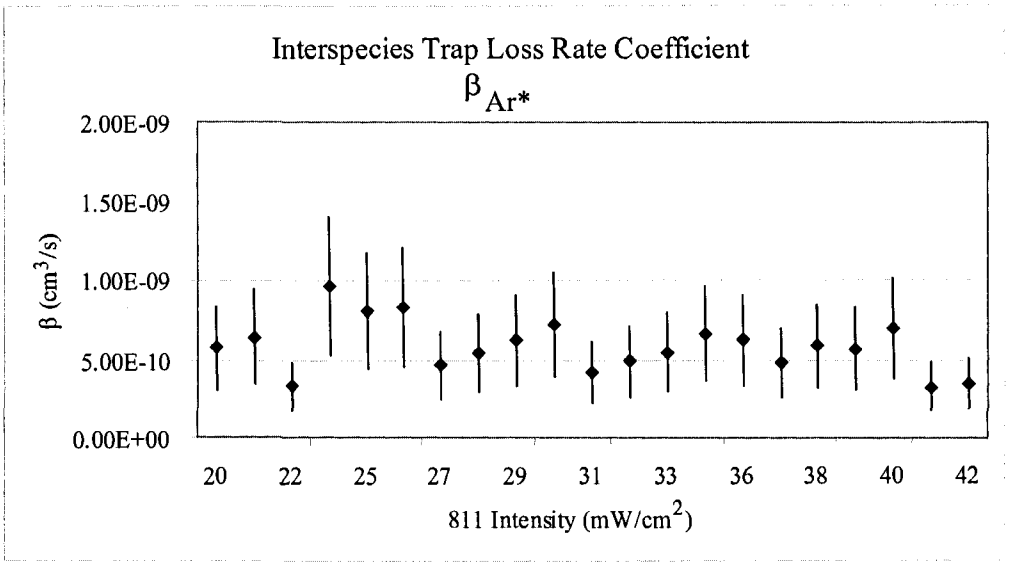

FIG. 35: Plot of β_{Ar} as a function of 811 nm trapping light intensity.

measurement for Ar*, β_{Ar}. Figure 35 shows the values of β_{Ar} over a range of 811 nm trap light intensities[49].

When the Rb and Ar* MOT are simultaneously loaded and allowed to interact, fluorescence measurements reveal the interaction between the two species. As the Rb MOT is allowed to load fully in the absence of the Ar* MOT, the fluorescence is observed. Next, the Ar* MOT is allowed to load while the Rb MOT fluorescence is continuously monitored. As the Ar* MOT loads, there is a slight decrease of roughly 3% in the number of Rb atoms confined in the MOT. Similarly, the Ar* MOT is allowed to load fully in the absence of Rb, and then the Rb MOT is allowed to load while the Ar* MOT fluorescence is monitored. Again a modest decrease in the number of trapped atoms occurs. A typical fluorescence curve is shown in Figure 36 where the Rb MOT is loaded in the presence of the Ar* MOT. Note that as the Rb MOT loads, a decrease in Ar* fluorescence is observed, later to be restored when the Rb MOT is removed. (Though the loading curve in Figure 36 illustrates the effect one MOT has on the other, it should be noted that this is not the method used to determine β'). While both MOTs are loaded there are no observed differences in trap volumes as compared to that of a single species MOTs, consistent with our approximation that the trap loads at constant volume.

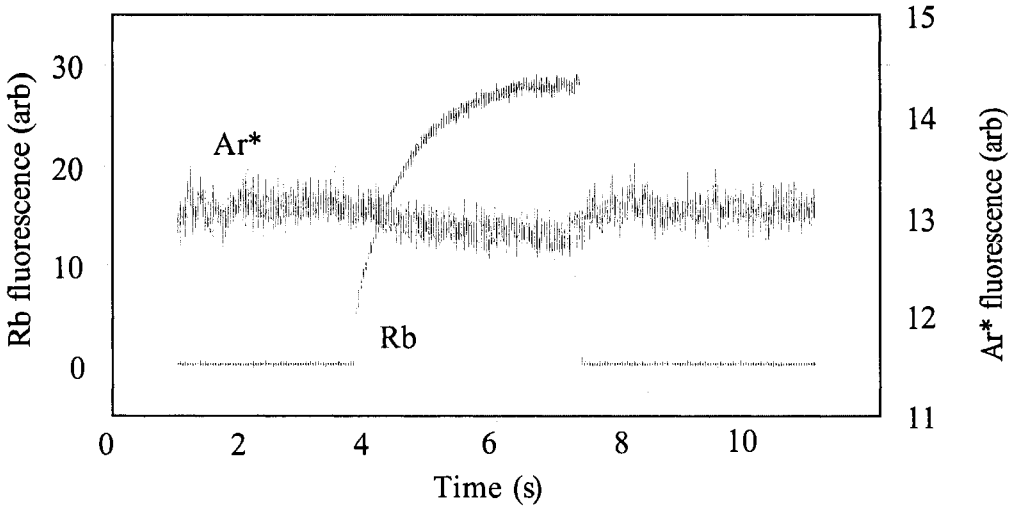

FIG. 36: A typical loading curve for a Rb MOT loading in the presence of an Ar* MOT.

With the single-species and dual-species behavior characterized, Equation 79 can be used to calculate the interspecies trap loss coefficient. With trap light intensities of 20 mW/cm^2 and 42 mW/cm^2 for ^{85}Rb and ^{40}Ar*, respectively, the coefficient for the loss of Rb due to the presence of Ar* is found to be $\beta'_{Rb-Ar*} = 3.0 \pm 1.3 \times 10^{-11}$ cm^3/s and the reciprocal coefficient for the loss of Ar* due to the presence of Rb is $\beta'_{Ar*-Rb} = 1.9 \pm 0.9 \times 10^{-11}$ cm^3/s [49].

In dual alkali-metal systems studied elsewhere, similar measurements have yielded a decrease of 20% in ^{39}K atoms when a ^{85}Rb MOT loads [51], a 45% decrease in ^{40}K when a ^{87}Rb MOT loads [52], and a 15% decrease in Na when a Rb MOT loads [53]. A review of recent heteronuclear trap loss measurements in dual alkali-metal systems can be found in [54]. Interestingly, in these experiments the reciprocal trap loss was usually found to be different. For example, no loss of Rb due to the presence of Na atoms was observed in [53] and no loss of ^{85}Rb due to the presence of ^{39}K atoms was observed in [51]. Here, the two loss rates are found to be similar[49].

Light-assisted collisions can be a significant factor in trap loss, and trap loss rates are found, in general, to depend on intensity and detuning. Mechanisms for trap loss include fine- and hyperfine-state changing collisions and radiative escape. As

the MOT light intensity increases, the recapture energy of the trap increases, but at the same time the excited state fraction increases. It is an interplay between trap depth and excited-state trap loss which explains the intensity dependence of trap loss. These same mechanisms can contribute to heteronuclear trap loss. In addition, doubly-excited state collisions of sodium atoms in a MOT can result in auto-ionization [55]. In metastable noble-gas traps, it is Penning and associative ionization which are mainly responsible for trap loss, and these processes can be enhanced or suppressed by near-resonant light [56] [57]. Typical rate coefficients for Penning and associative ionization in metastable noble gas MOTs are $10^9 - 10^{10}$ cm^3/s. For helium, the ionization rate can be greatly reduced by spin polarization of the atomic sample [58]; however, this suppression of ionization rates by spin polarization for heavier metastable atoms results in a less dramatic suppression factor in Ne* actually results in an increased ionization in Xe*. The ionization rates and suppression factors due to spin polarization in Ar* and Kr* are unknown.

At fixed detuning, the dependence of the loss rate coefficients on trap light intensity has been investigated. Operating at a detuning of -2 Γ for both MOTs, the intensity of the Ar* 811 nm trap light is varied over a range of 20–42 mW/cm^2 while holding the Rb 780 nm trap light constant at 20 mW/cm^2. The lower end of the intensity range was limited to stable trap operation. Results for β'_{Rb-Ar*} and β'_{Ar*-Rb} as a function of 811 nm trap light intensity are shown in Figures 38 and 40, respectively. Error bars arise from the quality of the fit, the reproducibility of the data, and the estimated error in the determination of the number of trapped atoms and MOT volume. Similar data were taken for the reciprocal experiment where the Ar* 811-nm light was held constant at 42 mW/cm^2 and the Rb 780-nm light was varied over a range of 15–20 mW/cm^2. Here we found that $\beta'_{Ar*-Rb} \sim 2 \times 10^{-11}$ cm^3/s, while β'_{Rb-Ar*} varied over a range of $2 - 3 \times 10^{-11}$ cm^3/s with little systematic variation over the range of intensities studied and uncertainties comparable to those in Figures 37 and 39 [49].

IV.2.1 Identifying Trap Loss Mechanisms

Next we turn our attention to identifying the mechanism responsible for the measured trap loss. Ultracold collisions between alkali-metal atom pairs in the ground (nS+nS) or first excited (nS+nP) molecular states do not have enough energy to result in ionization. For sodium, an atom pair in the second excited state (3P+3P) can

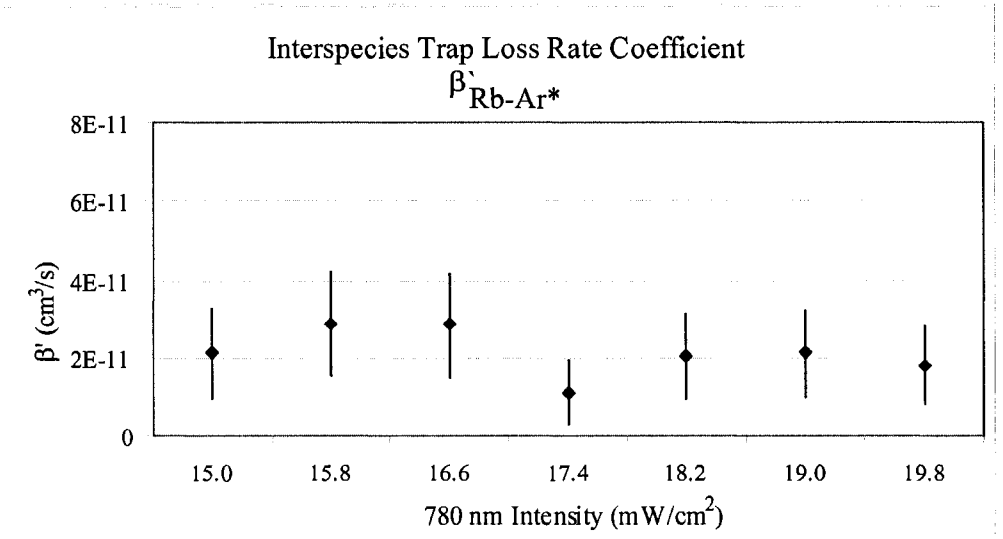

FIG. 37: 780-nm trap light intensity dependence of the interspecies trap loss coefficient β'_{Rb-Ar*}, for the loss of Rb due to the presence of Ar*

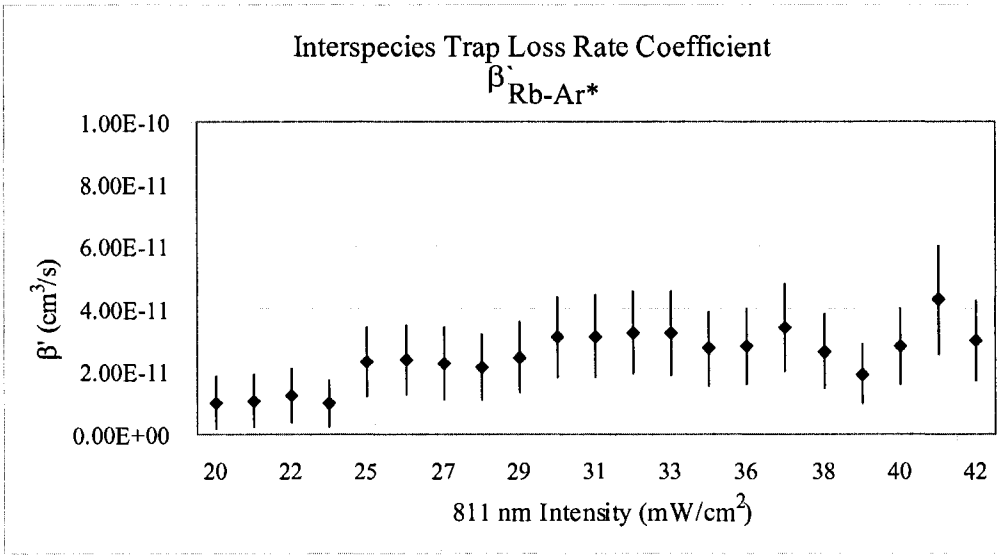

FIG. 38: 811-nm trap light intensity dependence of the interspecies trap loss coefficient β'_{Rb-Ar*}, for the loss of Rb due to the presence of Ar*

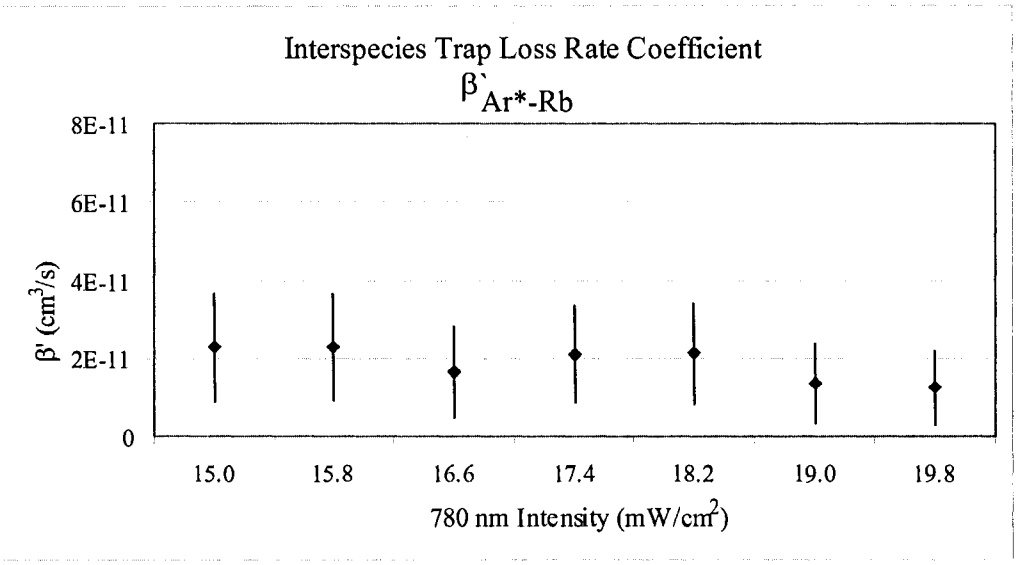

FIG. 39: 780-nm trap light intensity dependence of the interspecies trap loss coefficient β'_{Ar*-Rb}, for the loss of Ar* due to the presence of Rb

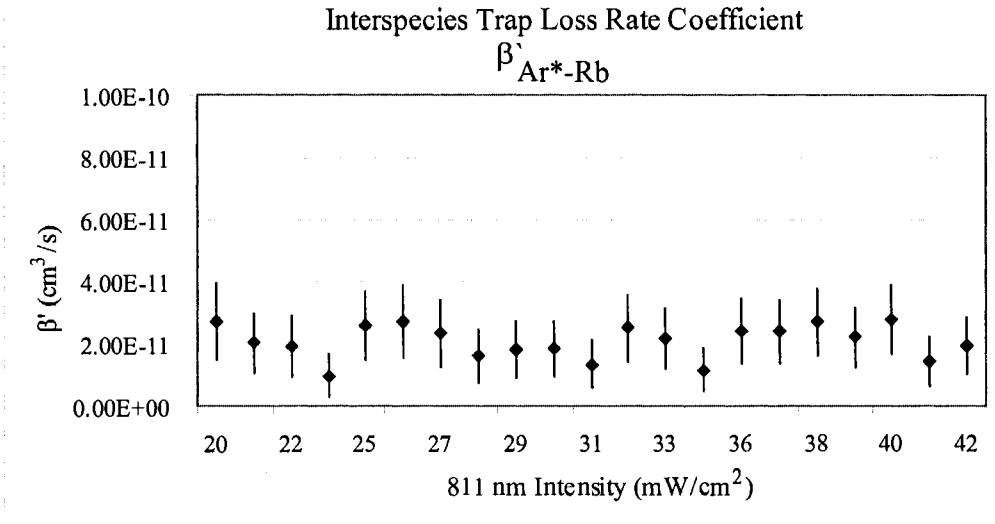

FIG. 40: 811-nm trap light intensity dependence of the interspecies trap loss coefficient β'_{Ar*-Rb}, for the loss of Ar* due to the presence of Rb

autoionize and heteronuclear photoassociative ionization producing $NaCs^+$ has been observed [27]. A metastable noble-gas atom like Ar*, however, contains more than enough internal energy to ionize a Rb atom. Ar* lies 11.6 eV above the ground state, considerably more than the 4.2 eV ionization energy of rubidium. As a result, one would expect that heteronuclear ionization plays a role in alkali-metal—noble-gas trap loss.

In order to confirm that ionization plays a role in Rb-Ar* MOT trap loss, the ion products need to be directly detected. One complication to ion detection is the large background of Ar^+ and Ar_2^+ ions produced in Penning and associative ionization occurring in the Ar* MOT alone. By comparison, for the trap loss observed here, ions produced in interspecies collisions are a negligible part of the total ion signal. To differentiate the ion products, the modified SRS RGA200 residual gas analyzer acts as a quadrupole mass spectrometer (QMS) as described in apparatus section. Ion optics placed in the MOT chamber accelerate all the ions produced in the MOT volume into the QMS where different mass products could be sorted. With only the Ar* MOT present, Ar^+ and Ar_2^+, arising from collision between ultracold Ar* atoms in the MOT, are clearly identified by count peaks at 40 and 80 amu, respectively. With only the Rb MOT present, no ions are detected. When the Rb MOT is superimposed on the Ar* MOT, additional peaks appear at 85 and 125 amu, corresponding to Rb^+ and $RbAr^+$, respectively, as shown in Figure 41.

This clearly identifies heteronuclear Penning and associative ionization as two of the mechanisms contributing to interspecies trap loss[49]. To specify the fraction of total trap loss attributable to ionization, an absolute measurement of ion yield will need to be conducted. The details of the collision dynamics depend on the molecular energy-level structure. Although recent calculations of the long-range interaction between two metastable rare-gas atoms were reported [59], to the best of our knowledge, the structure of Rb+Ar* has not been investigated theoretically.

IV.3 SUMMARY OF TRAP LOSS EXPERIMENT

For the first time, the interspecies trap loss rate coefficients have been measured for ultracold collisions between an alkali and a metastable rare gas, specifically Rb and Ar* in a dual-species MOT as a function of trap light intensity. The two rates have been found to be approximately equal over the range of intensities studied. In addition, the trap loss rate coefficient for cold collisions in a metastable argon MOT

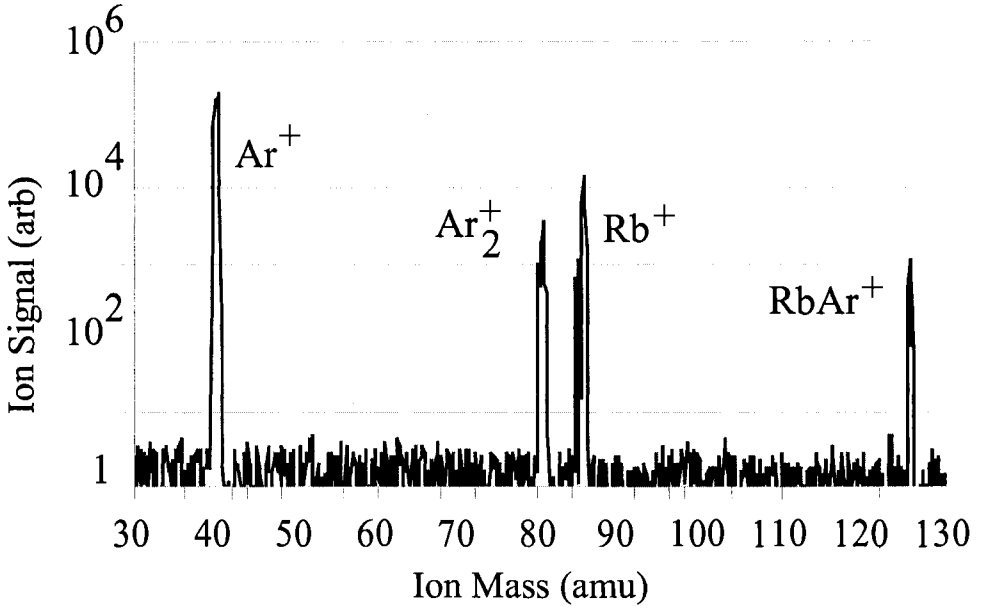

FIG. 41: Ion signal as a function of atomic mass from the quadrupole mass spectrometer

alone have been measured. Using a quadrupole mass spectrometer the production of Ar^+, Ar_2^+, Rb^+, and $RbAr^+$ ions in the dual MOT have been observed, clearly identifying heteronuclear Penning and associative ionization as trap loss mechanisms [49].

CHAPTER V

PHOTOASSOCIATION OF ULTRACOLD AR*

The photoassociative spectroscopy (PAS) of ultracold atoms is a powerful technique capable of investigating long-range interactions between atoms. The ultracold atomic clouds produced by laser cooling and trapping techniques virtually eliminates Doppler broadening in the sample, allowing for PAS to have an unprecedented resolution. To date, most of the PAS experiments conducted have, by far, been of alkali atomic systems. Only recently has a PAS investigation of an ultracold rare gas been conducted in He* [34]. In this experiment, the first PAS of ultracold Ar* along the $4s[3/2]_2 + 4p[5/2]_3$ asymptote will be investigated.

In photoassociation, two free atoms in a light field may be excited into a bound excited molecular state if the light field is resonant with a transition from the initial potential to a vibrational state of the excited molecular potential Figure 42. Once in the excited state potential, the atom pair generally relaxes through a number of different channels to other states. In one channel, the atom pair can relax into the original states by photon emission to a distribution of nuclear kinetic energies. In another, the molecule can relax into a bound ground state molecule. Far from exhausting the list, in yet another channel, a fine or hyperfine changing collision can take place where the atom pair are unbound but find themselves in different electronic states from where they began the collision. This list of exit channel possibilities is extensive and are very important when conducting photoassociation experiments in MOTs since they generally result in trap loss.

V.1 EXPERIMENTAL TECHNIQUE

In photoassociative spectroscopy, a probe laser is incident on a sample of atoms and scanned over a range of frequencies. When the laser is resonant with a free-bound transition to an excited molecular state and an excitation occurs, MOT trap loss increases and a resonance is observed. Scanning the probe laser through an extensive range of frequencies and recording MOT trap loss as a function of that frequency yields a photoassociative spectrum. This experimental technique has been used to successfully investigate many alkali atom systems.

Though it is the more understood mechanism for observing a PA resonance, trap

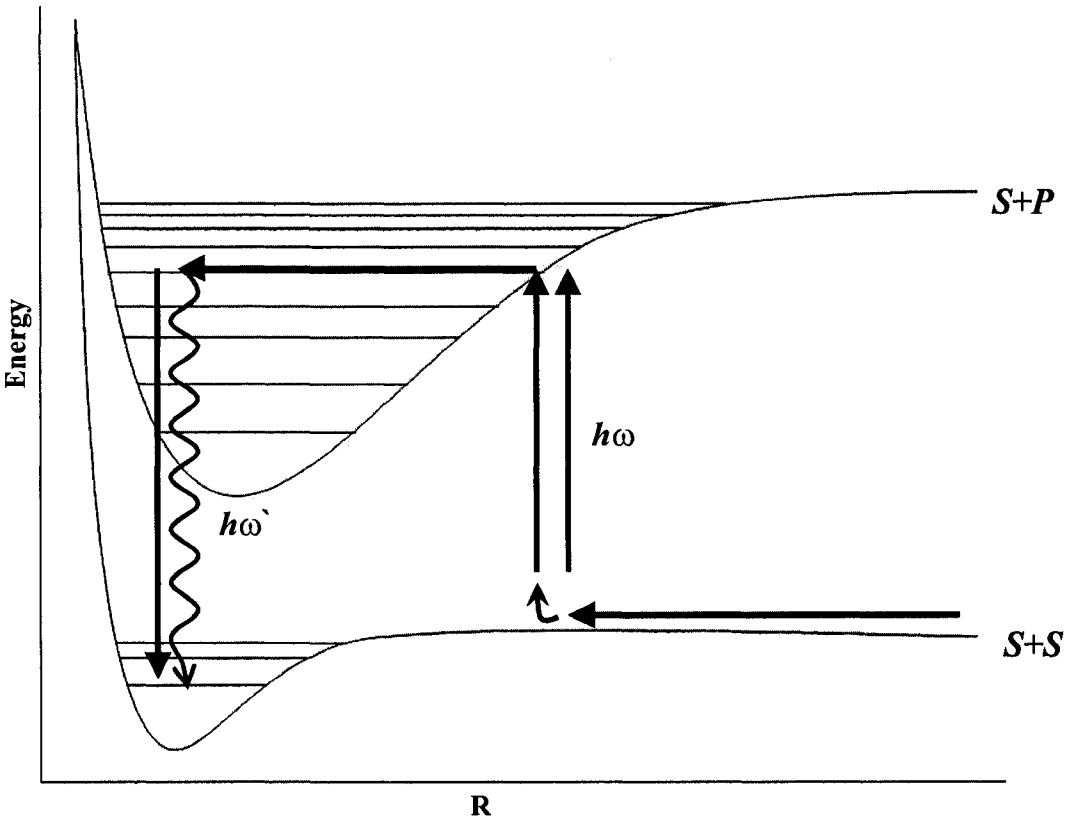

FIG. 42: Schematic of photoassociation during a homonuclear binary collision

loss is not the only method of detection. When the first Na MOT was constructed, it was observed that Na would auto-ionize when two atoms found themselves on a $P_{3/2}$+$P_{3/2}$ potential [37]. In 1993, Lett *et al.* used the Na ion signal, in addition to the trap loss signal, as an observable to detect PA resonances as they scanned a probe laser red of the MOT cycling transition to produce a PA-ion spectrum for Na, probing into the molecular bound-state structure of the $S_{1/2}$+$P_{3/2}$ potential for Na [39]. Though Na is the only doubly-excited state auto-ionizing alkali, the technique was applied to other alkalis by introducing a second, ionization laser tuned specifically to ionize the excited state molecule formed during PA. This method can be very advantageous due to the larger signal to noise ratio compared to trap loss observation.

Though research initiatives have primarily used photoassociative spectroscopy to investigate the alkali elements, there is no reason why the same principles can not be applied to investigate the rare-gas elements. One obvious complication is that in order to cool and trap the rare-gases, they must first be excited (by generally horribly inefficient means) into the metastable state where a feasible cycling transition can be used. But the additional internal energy of two colliding metastable atoms puts their molecular potential well above (~6eV for Ar*+Ar*) the potential for a molecular ion, making ionization possible and favorable. In fact, the magnitude of the ionization rate along the cycling transition is so large, special consideration is given to only perform spectroscopy only after the trap has been allowed to relax for some time, reducing the background ion counts by 10^3.

In this experimental investigation of the photoassociative spectroscopy of Ar*, the molecular potentials attached to the cycling transition, $4s[3/2]_2 + 4p[5/2]_3$, asymptote will be explored. Though investigations have been carried out on ionization suppression and optical shielding of Ne, Kr, and Xe, prior to this investigation, the only rare-gas element, photoassociative spectroscopic investigation yielding a spectra with resonances has been on He* [34] for its prospective application towards a He* BEC [60].

V.1.1 Ar* MOT characterization

To attain the largest ion signal from the MOT during the PA probe period, it is essential that the MOT be optimized for atom number and density. Unfortunately, as conditions in the laboratory change day to day (ambient temperature, magnetic

fields, rf discharge performance, etc.), the MOT too experiences changes making it necessary for daily optimization. Typically, this entails the balancing of light forces and ambient magnetic field compensation by the adjustment of the three shim coils around the science chamber. Optimization of the MOT is done by maximizing the PMT fluorescence signal and atom loading curve as well as observing the MOT fluorescence on the CCD surveillance cameras. After optimization, the Ar* MOT will contain $0.5 - 1 \times 10^6$ atoms. Because conditions are similar to those of the Rb-Ar* trap loss experiment and the MOT loads with constant volume, the density can be estimated to be $\sim 0.5 - 1 \times 10^{10}$ atoms/cm^3. Though in future investigations it may be useful to further characterize the MOT by taking daily absorption images.

V.1.2 Photoassociation lasers

The lasers that will act as the PA probe lasers in this experiment are of two separate systems: High-power diode lasers and a Titanium Sapphire (Ti:S) ring laser. Either one laser system will be the PA probe laser or the other as they will not act simultaneously as the probe laser. The explanation for having the two laser systems for the PA probe is that, though the Ti:S laser is capable for scanning narrow band ~20 GHz over a set frequency with semi-sufficient laser power, the Ti:S has a relatively long start up period and is pumped with an Ar^+ laser that requires large amounts of electrical power and a circulated chilled water supply. To break the dependence on such requirements, an effort was made to move towards the use of high-power laser diodes which are inexpensive, reliable, and simple to maintain. To verify that spectra obtained by using the home-built Littman-Metcalf cavity PA diode lasers was correct, the Ti:S ring laser was also used in the photoassociative spectroscopy experiment. These two laser systems are detailed in the apparatus chapter and share the same diagnostics (2 GHz spectrum analyzer, 300 MHz Fabry-Perot cavity, a 10 GHz etalon, and an Ar* saturated absorption spectrometer). For the PAS experiment, the laser systems will be treated the same once launched from the fiber optic near the science chamber.

The PA probe laser, TEM_{00}, is collimated after the fiber optic using a Thorlabs C110 f=6.24 mm lens to a ~3.0 mm Gaussian waist. The beam is polarization conditioned with AR coated $\lambda/4$ and $\lambda/2$ waveplates to be linearly horizontally polarized. The beam passes through an AR coated polarizing beam splitter before being steered by two IR mirrors through an AR coated f=+400 mm lens and into the center of the

science chamber. The laser at the MOT site is horizontally polarized and focused to a Gaussian waist of $\sim$130 μm (spectra were taken with various polarization orientations resulting in little if any change in the spectra). At the MOT site where the laser is focused, 50 mW of single pass PA laser power will produce a peak intensity of $\sim 10^4$ mW/cm^2 or $\sim 10^4 I_{Sat}$. As the PA laser leaves the science chamber on the other side, the light is again collimated, passes through another AR coated $\lambda/4$ waveplate and retro-reflected back upon itself. Passing through the $\lambda/4$ waveplate a second time results in the retro-reflected beam having a linearly vertical polarization and is again focused to the MOT site. Upon leaving the science chamber, the PA probe is reflected at the polarizing beam splitter to protect the fiber tip from ablation.

To align the PA beam with the MOT, the beam was first switched on with $\sim$30 mW output and the retro-reflection was blocked. Using an IR viewer, the beam was aligned along the axis of the science chamber centered on the entrance and exit ports such that the beam goes directly through the center of the science chamber. With the Ar* MOT loaded and optimized, the PA beam is tuned to resonance and the beam is systematically steered around until the MOT is greatly perturbed. Having an idea of where the beam is relative to the MOT, the PA power is decreased until the MOT is only slightly perturbed and the alignment adjusted for maximum effect at that given power. This step is repeated until satisfied. The PA laser is then detuned an arbitrary 2 GHz red of resonance with 20 mW of PA power. The PA data acquisition timing sequence is then turned on (in accordance with Figure 43), switching the trapping lasers and probe lasers and counting the ions produced during the probe phase. The probe ion rate is monitored on the photon counter and the alignment of the PA beam is adjusted to maximize the probe ion signal. The retro reflection is then unblocked and aligned. When the retro-reflection is precisely aligned, the probe ion counts will roughly double and a scan can now commence. It should be noted that the features in the PA spectra were only observed when the PA probe beam retro-reflection was aligned properly.

V.1.3 Timing, Detection and Data Acquisition

As with any experiment, when acquiring data one must strive for the best signal to noise ratio. The timing and detection schematic used in this experiment is chosen to maximize signal to noise while staying comfortably within the physical capabilities of the apparatus and its electronics. The primary observable of this experiment is

the ions produced by the photoassociation laser, which will be recorded as a function of laser frequency. For alkali atoms confined in a MOT, the atoms generally do not become ionized by either collisions or direct photoionization from the trapping laser (doubly excited ^{40}Na is an exception). For metastable noble gases, however, this is not the case. When two Ar atoms in the metastable $4s[3/2]_2$ state undergo a collision with 11.5 eV of internal energy each, it is energetically favorable to Penning or associatively ionize. This rate is relatively small because the two atoms see each other on an S+S, $1/R^6$ potential. Of the atoms in the MOT however, only $\sim$70 percent are in this state when the trapping lasers are present. The other $\sim$30 percent are in the $4p[5/2]_3$. While P+P potential yield similar rates to the S+S potential and can be neglected, the S+P potential, on the other hand, goes as the $1/R^3$ electric-dipole and at small internuclear distance has a large probability of making a Frank-Condon transition to the Ar_2^+ ion potential where Penning and associative ionization can take place. This rate of S+P ionization is 100 times larger than that for S+S or P+P and for the Ar* MOT in this experiment this rate is on the order of $\sim$50 kHz. By comparison, the ion production rate due to the PA probe laser is $\sim$10 kHz, making the ionization rate due to the excited state fraction quite large and would be devastating to experimental signal to noise.

One way to avoid detection of this enormous background ion signal is to probe a cloud of atoms that are $\sim$100% in the ground state. Once the trapping lasers, responsible for the excited state fraction, were removed, it only requires a few excited state lifetimes before the MOT was near completely in the $4s[3/2]_2$. After this time and the ion transit time for the ions to reach the CEM, the background ion production drops to $\sim$100 Hz. In this small time, ballistic expansion and drop of the atoms are negligible and ions produced by the PA laser can be collected with much better signal to noise. Thus for one data point, this entails the loading of the MOT, tuning off the trapping lasers, waiting some time t, probing with the PA laser, and collecting the ions.

Since many data points are required to be taken in succession for a set, a timing schematic was developed for laser timing and data acquisition. A bit of consideration had to be given to the behavior of the system under these timed conditions. For instance, when the MOT was switched on and off at certain frequencies, it was found to be driven, increasing and decreasing the number of atoms in the MOT on a time scale many times larger than the timing frequency. We found this to occur at $\sim$10 Hz

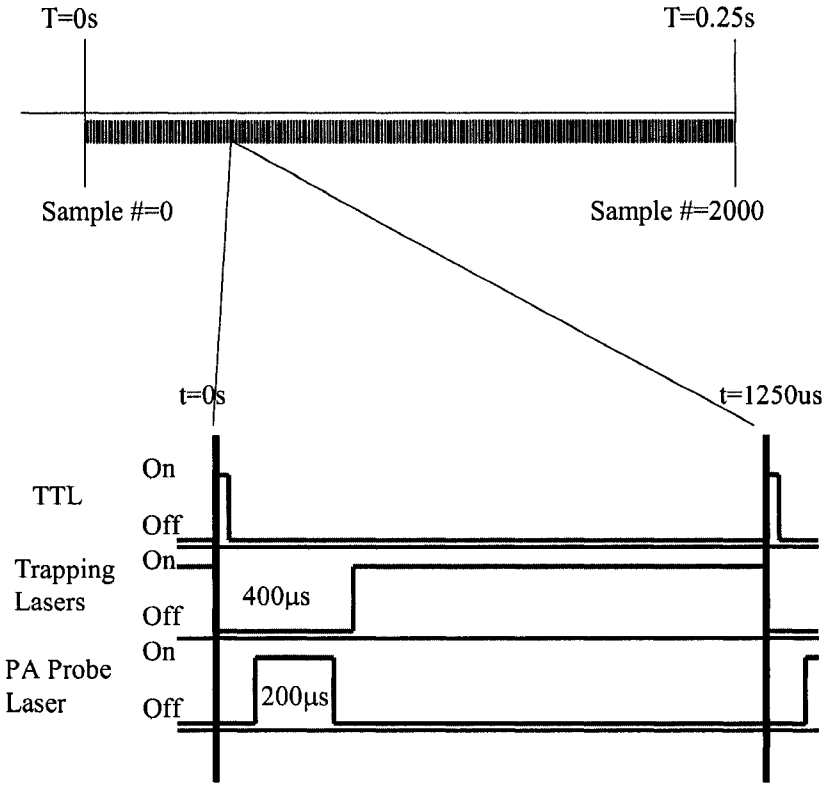

FIG. 43: Timing schematic for the photoassociative spectroscopy experiment.

and a few other frequencies. Also considered was the switching time for the AOMs, limited to ~20 μsec.

The timing schematic developed is pictorially represented in Figure 43. For each probe period, the trapping lasers are turned off at t=0 for 400 μsec. After a 30 μsec delay, the PA laser is switched on for 200 μsec. After t=400 μsec the trapping lasers are on again and the MOT reloads. This probe/MOT cycle is repeated at 800 Hz. During the 200 μsec probe period, a gate is open on the SRS400 photon counter channel A to collect the ions produced during this phase. Channel B on the photon counter is open for 200 μsec again, but is delayed 900 μsec from t=0 serving to record the background ion signal from the MOT for normalization purposes. The photon counter bins the number of ions from 2000 probe/MOT cycles into a single bin, the data values are read by a LabView acquisition program along with other experimental values (300 MHz Fabry-Perot, 10 GHz etalon, SAS, wavemeter data, and MOT fluorescence). This data collected during this sequence serves as one data

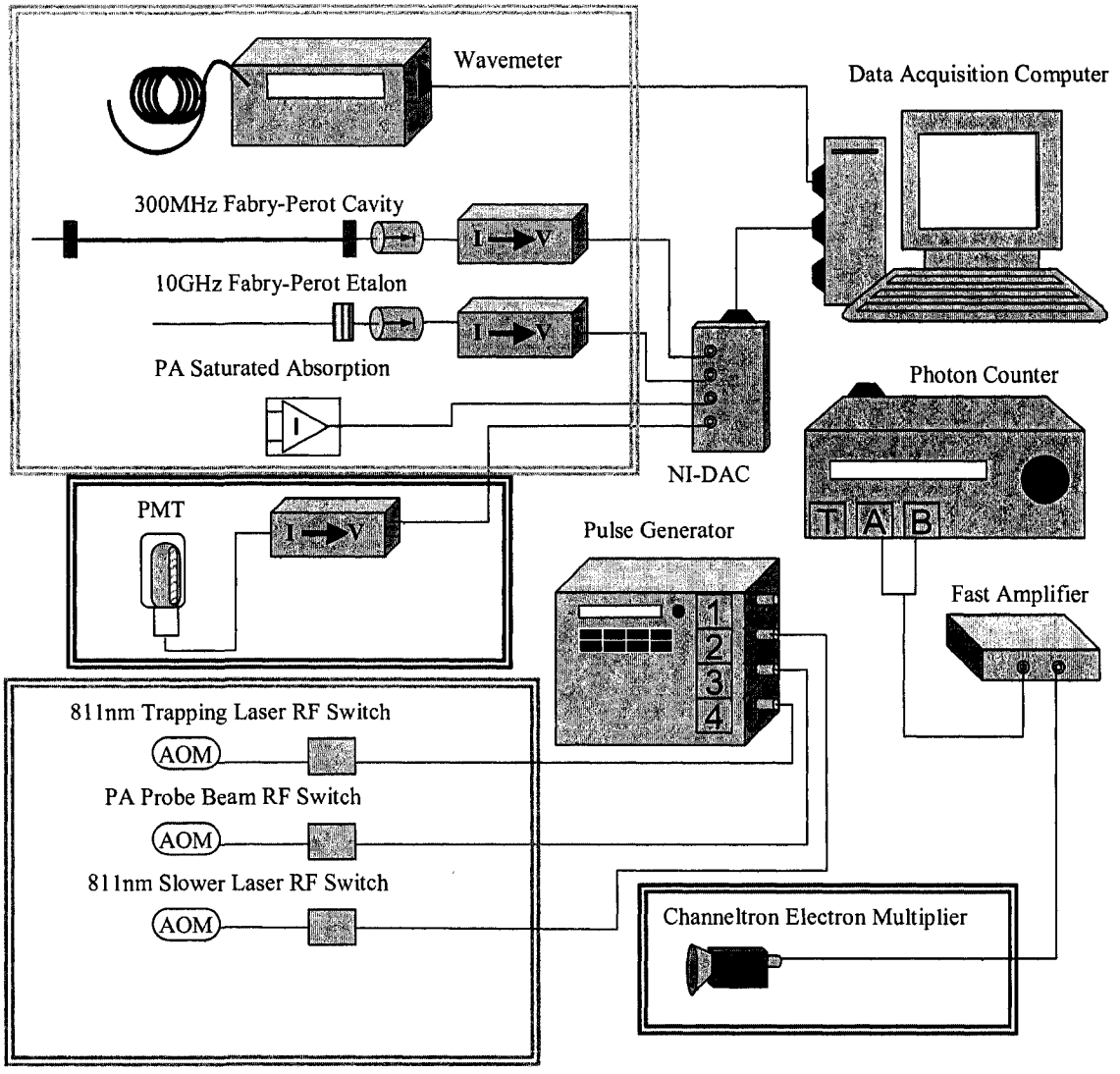

FIG. 44: Pictorial representation of the data acquisition system for the photoassociative spectroscopy experiment.

point for a single frequency. To create a meaningful spectrum, this process is repeated over 500 seconds as the laser is scanned over a 10 GHz (or 2 GHz) range near the atomic resonance. This corresponds to $\sim$ 2000 data points for a given PA scan with a step resolution of $\sim$5 MHz/point. The data acquisition system is pictorially described by Figure 44.

V.2 ANALYSIS AND DISCUSSION OF RESULTS

When the Ar* MOT is loaded without the PA beam present, it contains $\sim 10^6$ atoms and $\sim$ 80 kHz of ions are detected on the CEM (of which $\sim$ 2 kHz are attributed to the atomic beam of Ar*). When the trapping laser light is switched as described above, $\sim$ 2 kHz of ions are detected during the probe period, of which the majority of the counts are attributed to the atomic beam of Ar* and not trapped Ar* in the MOT. When the PA beam is incident on the MOT, the ion rate during the probe period varies from 1-100 kHz depending on the detuning and intensity of the PA beam. To acquire a photoassociation spectrum, the timing/switching scheme described above is run while scanning the PA laser at a fixed intensity over either a 10 GHz or 1 GHz range. The range scanned is selected to include all detectable PA resonances while including the atomic resonance as an absolute reference (observed in the SA spectrum). In the photoassociation of He*, Niehaus *et al.* [34] observed PA channel competition as the intensity of the PA beam was varied. This is also observed in the PA of Ar*. To illustrate this effect, PA spectra of Ar* are acquired over a set of PA beam intensities ranging from $\sim 10^4 - 10^5 I_{Sat}$ and $\sim 10^2 - 10^4 I_{Sat}$ for 10 GHz and 1 GHz scans respectively. When acquired, each data point is recorded with the photodiode reading from both a 300 MHz Fabry-Perot cavity, a 10 GHz etalon, and the SAS or Ar*. In part employed to ensure mode-hop free operation of the probe laser, these three diagnostics allow for a calibration of the detuning of the probe laser such that as the probe laser is scanned, the frequency is known to $\sim$25 MHz or better.

The 1 GHz and 10 GHz photoassociative spectra for Ar* are shown in figures 45 and 46 respectively. The X axis for these spectra have been calibrated to relative detuning from the atomic resonance in GHz via the $\sim$300 MHz Fabry-Perot cavity, 10 GHz etalon and Ar* saturation absorption spectrum. Resonances in the spectra are identified by a discrete change in the ion count relative to the background ionization. Here, the resonances are identified as a reduction in the ion signal. This is quite

different than observations in the PAS of He*, where resonances are clearly increases in ionization rate [34]. An explanation as for the possible reasons for this will be given later. As clearly seen in the 10 GHz PA spectra, there is a broad increase in ionization with increasing probe laser intensity. The resonances locations are determined by the position of the local minima in the spectrum and are tabulated in Table III.

Especially noticeable at high intensities, as the PA beam becomes closer to the atomic resonance, the PA beam increasingly disturbs the MOT, eventually to the point of depleting the MOT completely. This effect was also observed in the PAS of He* [34]. Regardless of this distinguishable effect, it is clear that photoassociative molecular resonances are observed. To ensure that the observed spectra are not artifacts of the diode PA lasers, the spectra were also taken with the Ti:S laser system. The PA spectra obtained using the Ti:S over similar ranges show features at identical detunings, but are less defined. When attempting to reproduce the spectra again using the diode PA lasers, spectra very similar to the Ti:S spectra were obtained. This suggests that the features in the spectra are PA resonances and the fact that the features are less defined are attributed to a subtle, unknown change in experimental conditions.

V.2.1 Ar_2 S+P C_3 Coefficients and Curves

Though, by far, most of the experimental and theoretical work on molecular potentials and PAS is conducted on alkali atoms, Verhaar *et al.*[59] examined the long range diatomic molecular potentials of the rare-gas atoms connected to the asymptotic $R(n-1)p^5ns + R(n-1)p^5np$ states. Conveniently, this includes the $4s[3/2]_2 + 4p[5/2]_3$ states, along which this PA investigation is conducted. Their work explicitly determined the reduced C_3 coefficients for the $ns[3/2]_2 + np[5/2]_3$ curves relevant for ^{20}Ne, ^{40}Ar, ^{84}Kr, and ^{136}Xe. By using a given conversion factor of 1.62×10^{-7} for Ar, the C_3 coefficients can be calculated. These C_3 values for Ar* and other rare gases are tabulated in Table V.2.1 with their associated molecular state. In addition, the long range potentials for the S+P transitions in Ar have been calculated and have been plotted in figures 47 and 48 [61].

It is important to note that of the 40 molecular potentials connected to the $4s[3/2]_2 + 4p[5/2]_3$ asymptote, only 20 are attractive and need to be considered.

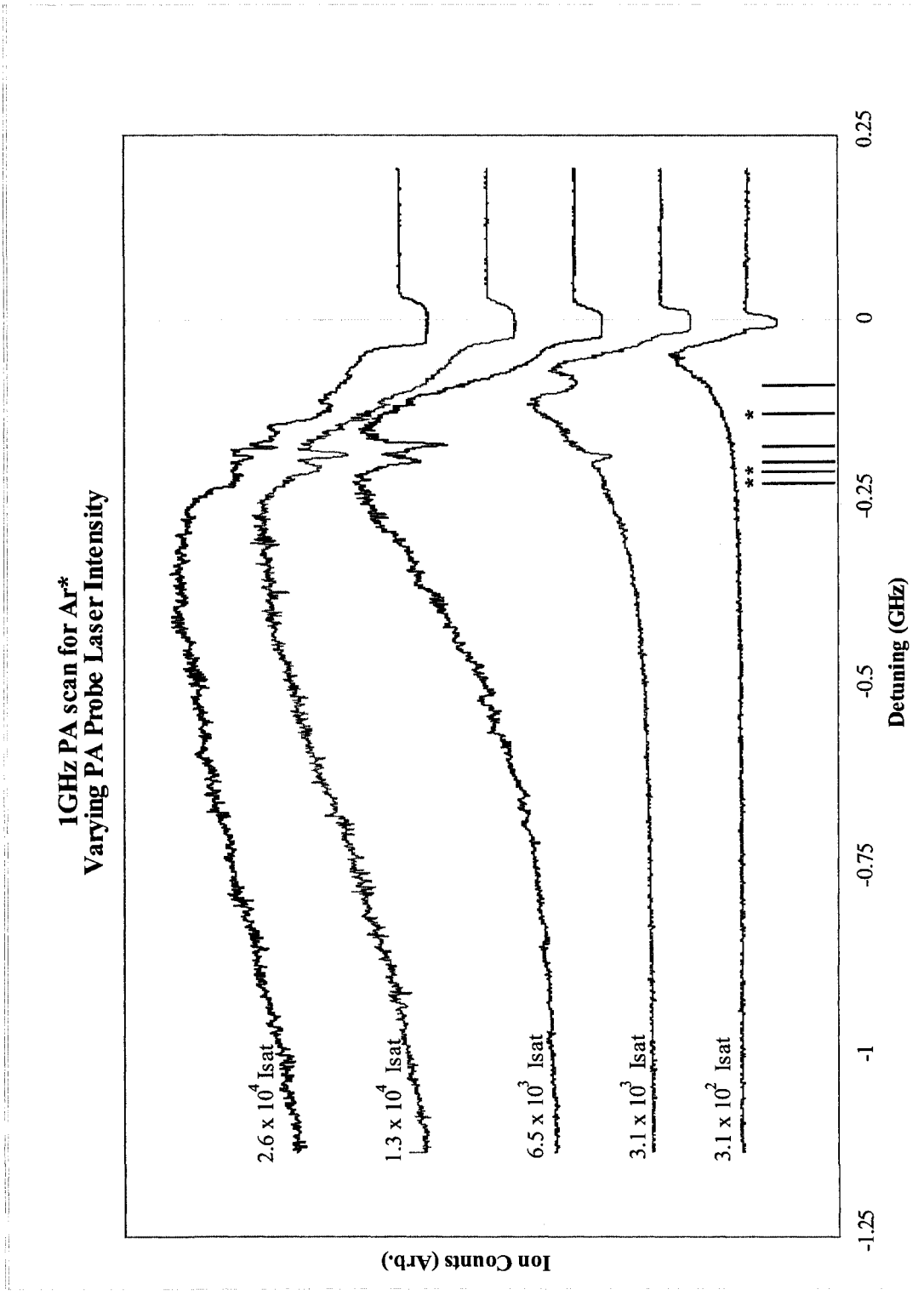

FIG. 45: Photoassociative ionization spectrum for Ar* near the $4s[3/2]_2 + 4p[5/2]_3$ asymptote. Resonance locations are indicated by vertical dashes near the x axis. Spectra are plotted in order of increasing PA intensity starting with the lowest value on the bottom.

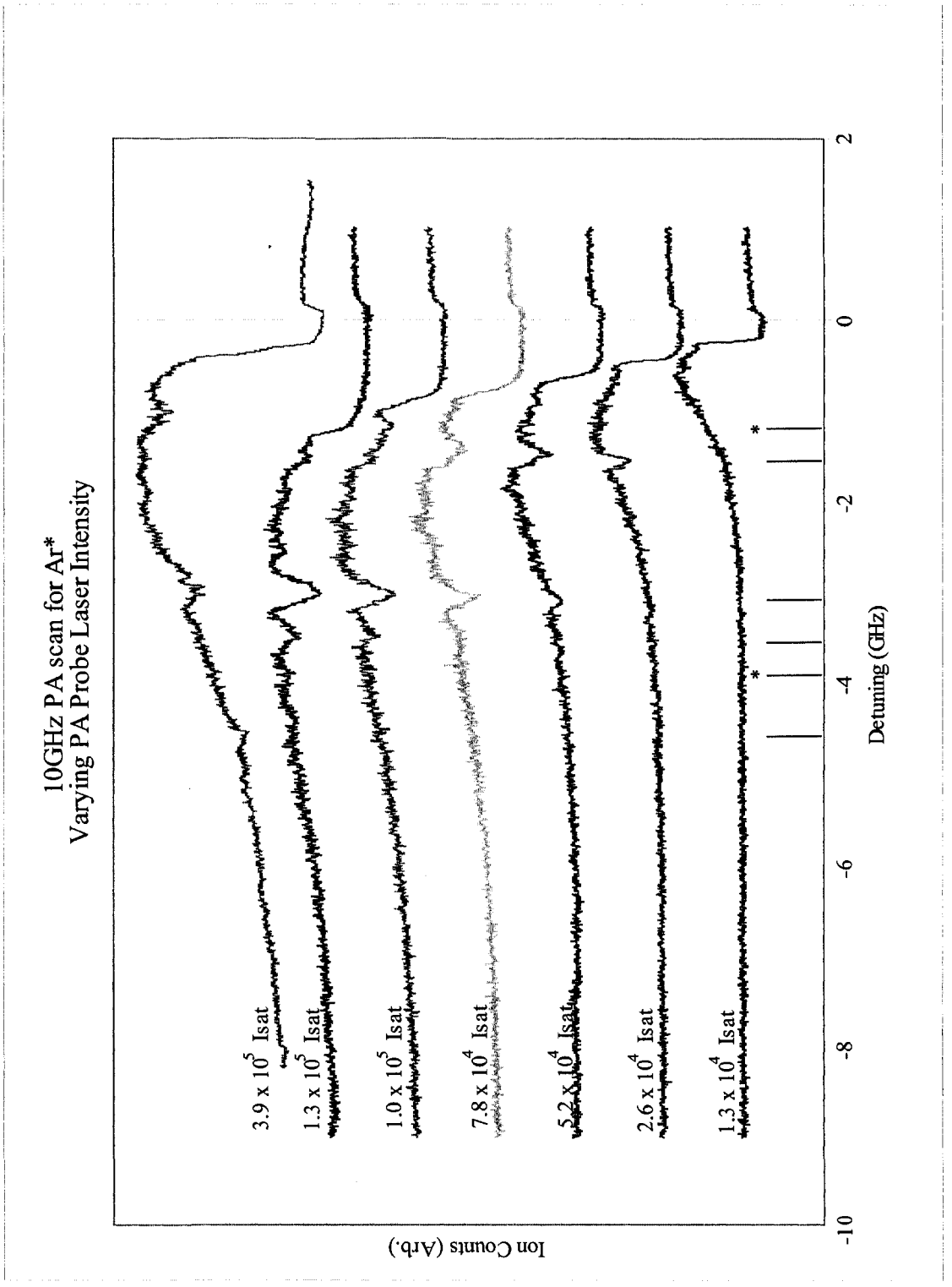

FIG. 46: Photoassociative ionization spectrum for Ar* near the $4s[3/2]_2 + 4p[5/2]_3$ asymptote. Resonance locations are indicated by vertical dashes near the x axis. The highest intensity scan is taken under extraneous experiential conditions. Spectra are plotted in order of increasing PA intensity starting with the lowest value on the bottom.

TABLE II: C_3 coefficients for Ne, Ar, Kr, and Xe diatomic molecular potentials. All C_3 values shown are multiplied by 10^{50} [59]

State $\Omega_{(g/u)}^{(+/-)}$	$C_3^{Reduced}$ (J m^3 ns/nm^3)	Ne_2C_3 (J m^3)	Ar_2C_3 (J m^3)	Kr_2C_3 (J m^3)	Xe_2C_3 (J m^3)
0_u^+	-497.52	-672.64	-805.98	-958.72	-1004.99
0_g^-	-369.02	-498.91	-597.81	-711.10	-745.42
0_u^+	-271.21	-366.67	-439.36	-522.62	-547.84
0_g^-	-183.67	-248.32	-297.54	-353.93	-371.01
0_u^+	-166.55	-225.17	-269.81	-320.94	-336.43
0_g^+	166.55	225.17	269.81	320.94	336.43
0_u^-	183.67	248.32	297.54	353.93	371.01
0_g^+	271.21	366.67	439.36	522.62	547.84
0_u^-	369.02	498.91	597.81	711.10	745.42
0_g^+	497.52	672.64	805.98	958.72	1004.99
1_u	-490.86	-663.65	-795.20	-945.89	-991.54
1_g	-359.33	-485.81	-582.11	-692.43	-725.84
1_u	-252.21	-340.99	-408.59	-486.02	-509.47
1_g	-193.81	-262.03	-313.97	-373.47	-391.50
1_u	-1.35	-1.83	-2.19	-2.61	-2.74
1_g	1.35	1.83	2.19	2.61	2.74
1_u	193.81	262.03	313.97	373.47	391.50
1_g	252.21	340.99	408.59	486.02	509.47
1_u	359.33	485.81	582.11	692.43	725.84
1_g	490.86	663.65	795.20	945.89	991.54
2_u	-470.83	-636.57	-762.75	-907.30	-951.09
2_g	-328.57	-444.23	-532.29	-633.17	-663.73
2_u	-214.48	-289.98	-347.46	-413.31	-433.26
2_g	-16.60	-22.44	-26.89	-31.99	-33.53
2_u	16.60	22.44	26.89	31.99	33.53
2_g	214.48	289.98	347.46	413.31	433.26
2_u	328.57	444.23	532.29	633.17	663.73
2_g	470.83	636.57	762.75	907.30	951.09
3_u	-436.79	-590.54	-707.60	-841.69	-882.32
3_g	-274.95	-371.74	-445.43	-529.84	-555.41
3_u	-71.96	-97.30	-116.59	-138.68	-145.37
3_g	71.96	97.30	116.59	138.68	145.37
3_u	274.95	371.74	445.43	529.84	555.41
3_g	436.79	590.54	707.60	841.69	882.32
4_u	-387.49	-523.89	-627.74	-746.71	-782.74
4_g	-174.94	-236.53	-283.41	-337.12	-353.39
4_u	174.94	236.53	283.41	337.12	353.39
4_g	387.49	523.89	627.74	746.71	782.74
5_u	-318.88	-431.13	-516.59	-614.49	-644.15
5_g	318.88	431.13	516.59	614.49	644.15

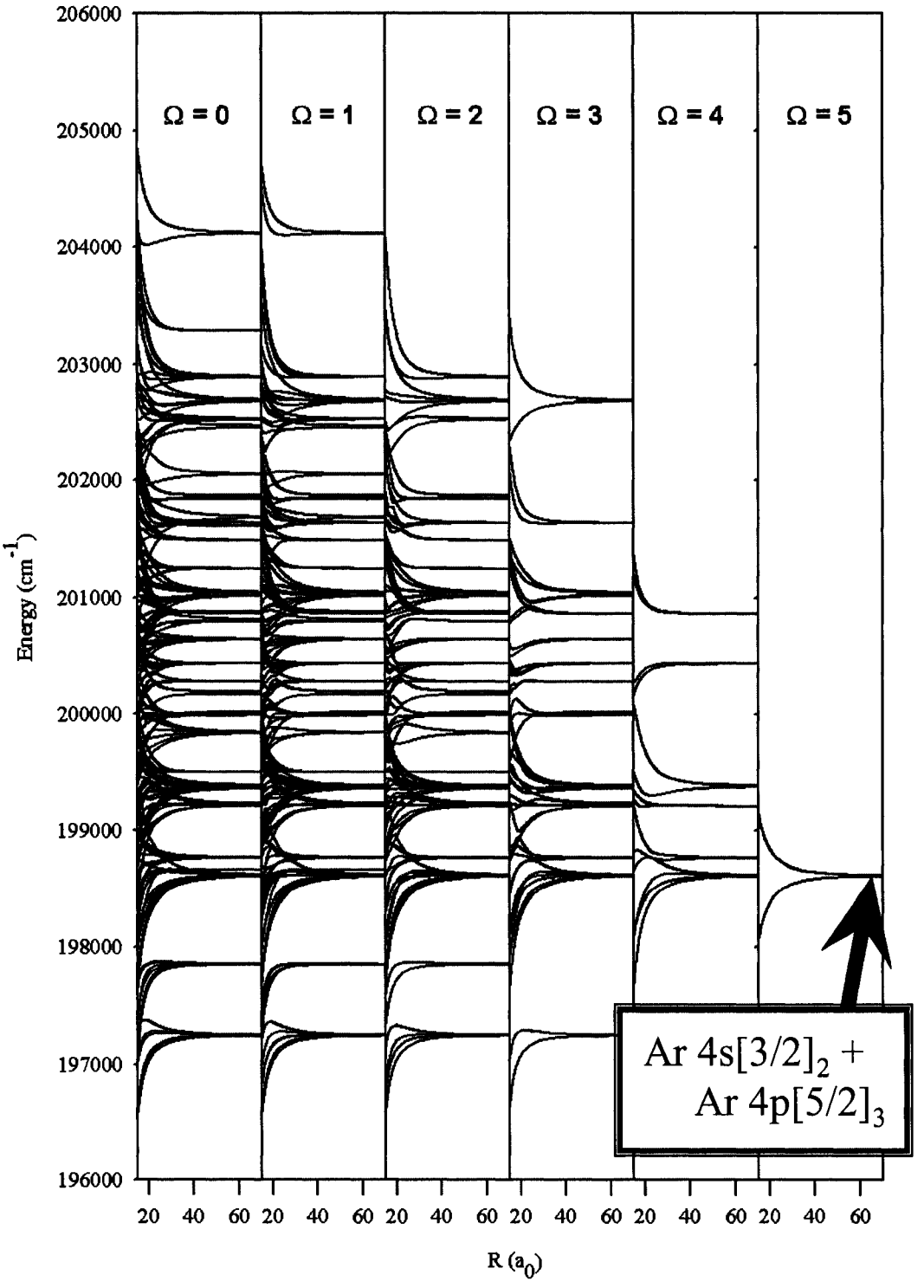

FIG. 47: Diatomic molecular Ar potentials for the S+P transitions for Ω=0...5

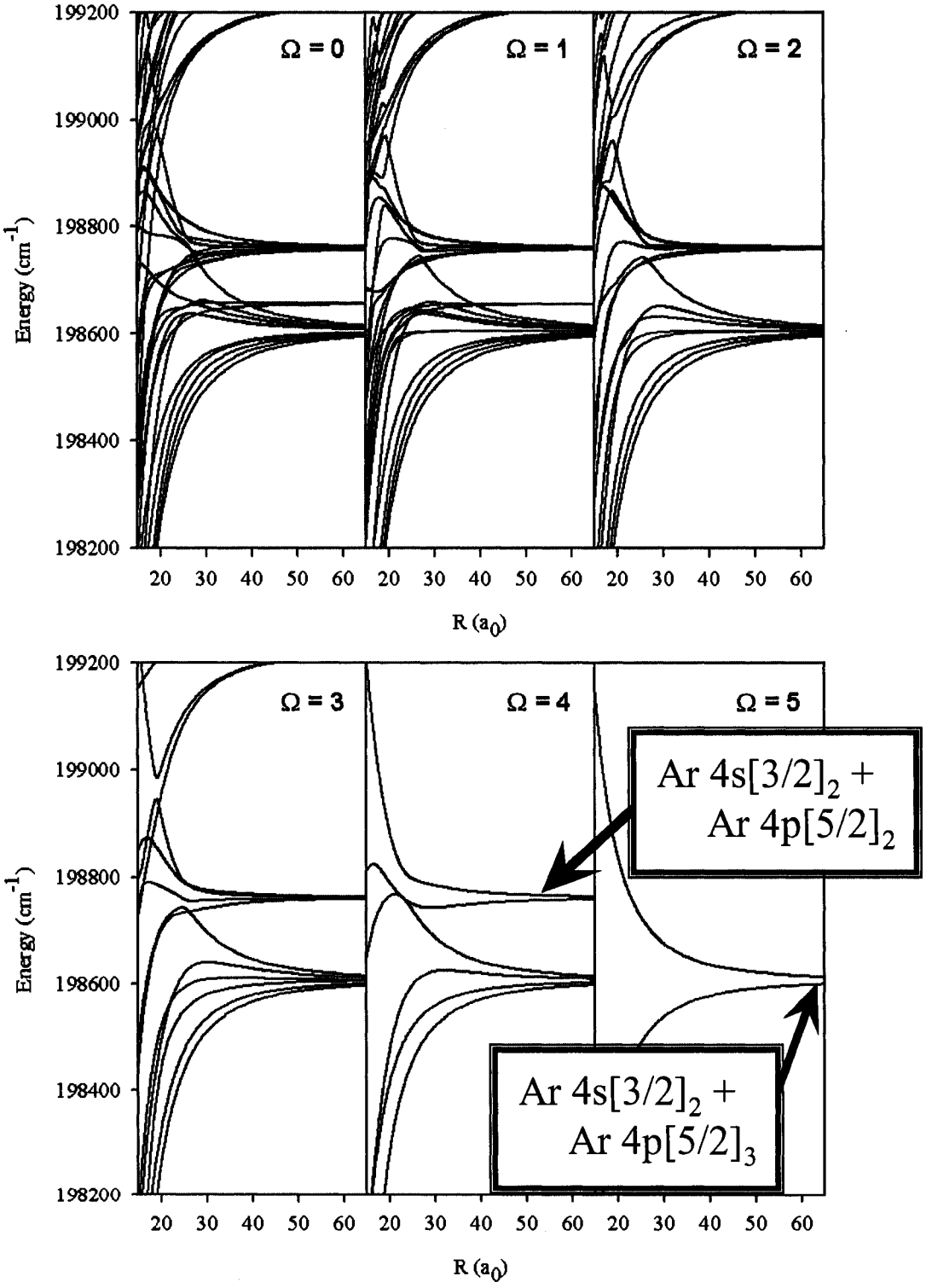

FIG. 48: Diatomic molecular Ar potentials for Ω=0...5, scaled for detail of the potentials connected to the relevant $4s[3/2]_2 + 4p[5/2]_3$ asymptote and the $4s[3/2]_2 + 4p[5/2]_2$ asymptote just above.

V.2.2 The LeRoy-Bernstein Formula

Photoassociative spectroscopy experiments of alkali systems generally rely on an increase in trap loss as a means to observe a molecular resonance. When the PA laser comes into resonance with a free-bound transition to an excited molecular vibrational state, there is a probability, depending on the Frank-Condon factor, that the transition will take place and MOT trap loss will result. This technique generally uses a high power PA laser with a high density MOT, resulting in numerous observed resonances up to hundreds of GHz away from the atomic resonance where MOT perturbation due to atomic resonances is minimal. With many resonances in a single spectra, the peaks can generally be assigned into individual series which are associated with specific excited-state molecular potentials. With the added advantage of a non-zero nuclear spin, often PA resonances of alkalis with hyperfine splitting have shapes that can be tell-tale of the symmetry of the states associated with the resonance, making assignments a bit easier. This is of course not the case for ^{40}Ar where high densities are difficult to achieve and $I = 0$. Depending on the shape of a molecular potential, the number of possible vibrational bound states in a given frequency interval can vary considerably. When considering the number of excited-state molecular potentials possible for a given free-bound transition to an S+P state at large r, (Ar* has 40 for the trapping transition), each of which may have an associated vibrational series, the number of accessible resonances can become very large and proper state assignments becomes far more difficult. For the alkali systems, the number of observed peaks is large, helping to lift the ambiguity of which series a peak may belong to. In an ideal case like this where an abundance of PA spectroscopic information is available, the coefficient of the leading long-range term in the molecular potential (among other data) can be extracted using the LeRoy-Bernstein formula [41].

$$D - E = \left[\left(\sqrt{\frac{\pi}{2\mu}}\frac{\Gamma(1+1/n)}{\Gamma(1/2+1/n)}\frac{\hbar(n-2)}{(-C_n)^{1/n}}\right)(\nu_D - \nu)\right]^{\frac{2n}{n-2}} \tag{82}$$

Here D is the molecular dissociation energy, E is the energy of the vibrational level ν, ν_D is the non-integer effective dissociation level, n is the order of the leading coefficient for the molecular potential, μ is the reduced mass, and Γ is the gamma function. The LeRoy-Bernstein formula is an effective tool for the analysis of states near dissociation, but because it depends exclusively on atomic parameters, the approximation

breaks down at internuclear distances where the valence electron wavefunctions begin to overlap. For this experiment, the molecular interaction on the S+P potential will be investigated for near-dissociation levels. The dipole-dipole dominated potential has a leading coefficient of C_3/R^3, hence n=3. Equation 82 then becomes

$$D - E = \frac{1}{C_3^2}\left[\left(\hbar\sqrt{\frac{\pi}{2\mu}}\frac{\Gamma(4/3)}{\Gamma(5/6)}\right)(\nu_D - \nu)\right]^6 \tag{83}$$

If a sufficient number of resonances are in a spectra, it is possible to identify progressions of peaks belonging to a vibrational series, each series arising from a single excited-state molecular potential. Knowing the value of $D - E$ from the relative resonances positions, by using Equation 83 and a simple least squares fitting routine with fitting parameters ν, ν_D, and C_3, one can extract the values of C_3 for each series. These values can then be compared to theoretical calculations to check accuracy and give possible molecular state assignments.

If the PA spectra are of insufficient number of resonances to determine a series progression, as is the case for Ar*, the reciprocal analysis must be done. Here, theoretically calculated C_3 values for the relevant molecular curves will be used with Equation 83 to determine energies where resonances may be observed which will be compared with the experimentally observed resonances to make preliminary molecular assignments.

Using the C_3 values for Ar* from Table V.2.1 in Equation 83 for a range of $\nu_D - \nu$ from 1 to 50, the energy values for vibrational resonances in the associated series are obtained. Of the 40 molecular potentials connected to the $4s[3/2]_2 + 4p[5/2]_3$ asymptote, only the 20 corresponding to attractive potentials need to be considered. The resulting 1000 calculated vibrational resonances range from 1 Hz - 500 GHz+ in red detuning from the $4s[3/2]_2 + 4p[5/2]_3$ asymptote. It is important to notice that this approach makes an assumption that the dissociation energy D is equal to the energy of the $4s[3/2]_2 + 4p[5/2]_3$ asymptote. Generally, this may not be the case since nearby potentials associated with other asymptotes can add perturbations which may raise the dissociation energy above the asymptote. Fortunately, the $4s[3/2]_2 + 4p[5/2]_3$ potentials are not perturbed and the assumption is valid.

In Figure 49, the calculated vibrational resonances that occur between 0-10 GHz for each state have been plotted on an arbitrary Y axis. As seen in Figure 49, the number of possible molecular resonances occurring within 10 GHz of the atomic transition is plentiful. Without a means to eliminate some of the possibilities, assigning

observed resonances to particular molecular states would indeed be difficult.

With the theoretical vibrational resonances calculated and the observed resonances tabulated, a comparison is made between the two sets to determine which calculated resonances may contribute to an observed resonance. In doing this, experimental uncertainty in laser frequency is accounted for to the observed resonance position. The results of this comparison are presented in Table III. Due to the few number of resonances observed and many corresponding possibilities for each, the assignments in Table III can only be regarded as preliminary. It is also difficult to narrow the possibilities for resonances by determining which, if any, series may not contribute to the observed resonances.

In [59], it is mentioned that of the possible excited state potentials, most attractive potentials have an ionization probability close to unity. The exception is the fully stretched state of Ω=5 for Ar*, which to first order cannot ionize because of spin selection rules.

Consider the case of He* where ionization suppression by spin polarization is the strongest among the metastable rare gases. Penning ionization of He* at small internuclear distances can be understood with the aid of Figure 50. When an He atom is excited to the metastable state (He*), a core electron is excited into the valence shell such that the spin of the valence electron is identical to the spin of the unpaired electron remaining in the core shell. Due to the Pauli exclusion principle, the valence electron cannot occupy the vacancy without flipping its spin which makes this transition dipole forbidden. When considering two unpolarized He* atoms (A and B), at small internuclear distances, the valence electron of Atom B may fill the vacancy in the core of Atom A if the spin orientation is correct. With the valence shell of Atom A now closed, the excess electron is ejected, leaving behind Atom A in the ground state and Atom B as an ion. If, however, Atoms A and B were polarized, the spins of the valence electrons of both atoms are identical and the transfer of the electron to fill a core vacancy is forbidden. Hence ionization through this mechanism is suppressed. Though this example was stated for He*, it should also be somewhat valid for Ar*, but has not yet been investigated.

The high probability to ionize in states other than the spin stretched state suggests a molecular lifetime on a time scale much shorter than the vibrational period of the molecule, leading to an extremely broad linewidth. Verhaar *et al.* suggests that results in PAS may vary and it may be the case where no resolvable structure from the

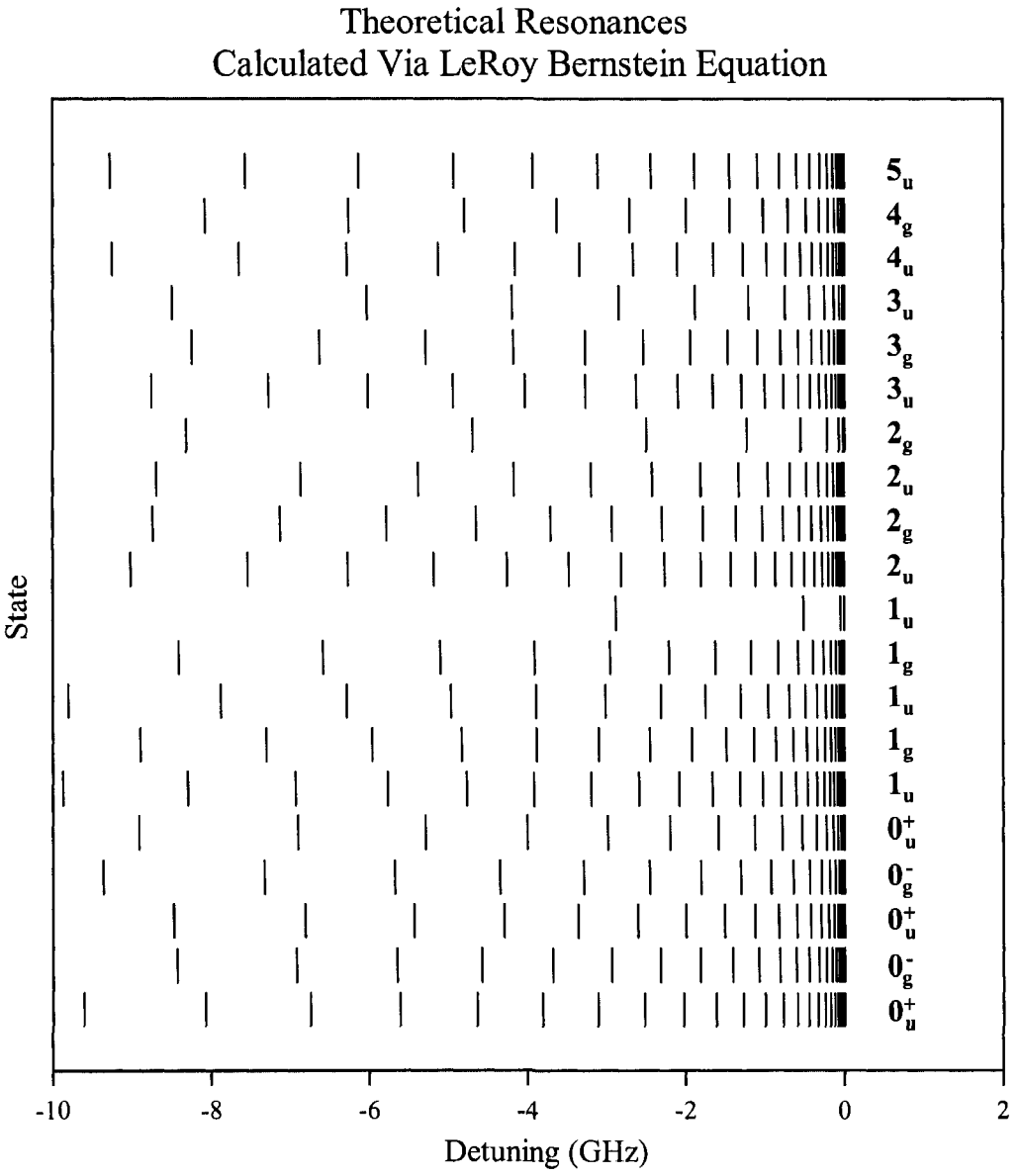

FIG. 49: Diatomic molecular resonances for Ar for the S+P transitions for Ω=0...5

TABLE III: Tabulated are the observed resonances labeled by number in n and possible corresponding calculated resonances located within the estimated experimental error. Included are the Ω and $\nu_D - \nu$ values and the state number. An (*) is used to denote low confidence.

n	δ Obs. (GHz)	δ Calc. (GHz)	Ω	#	ν–ν_D	n	δ Obs. (GHz)	δ Calc. (GHz)	Ω	#	ν–ν_D
1	4.5400	4.5800	0	2	28	9	0.189	0.185	0	4	13
2*	3.84	3.81	0	1	30			0.183	1	1	18
		3.88	1	2	27			0.195	3	2	15
		3.89	1	3	24	10	0.165	0.159	0	2	16
3	3.47	3.47	2	1	29			0.168	1	2	16
4	3.07	3.11	0	1	29			0.166	1	4	13
		3.09	1	2	26			0.164	3	1	17
		3.11	5	1	25	11*	0.12	0.126	0	1	17
5	1.44	1.42	2	1	25			0.114	0	4	12
		1.44	4	2	18			0.114	1	2	15
		1.44	5	1	22			0.114	3	1	16
6*	1.10	1.12	2	1	24			0.126	4	2	12
		1.10	3	2	10	12	0.0840	0.0877	0	1	16
		1.09	5	1	21			0.0849	0	3	13
7*	0.221	0.229	0	2	17			0.0826	0	5	11
		0.225	0	5	13			0.0901	1	1	16
		0.219	2	4	6			0.0902	2	2	14
		0.213	5	1	16			0.0840	2	3	12
8*	0.201	0.200	0	3	15			0.0820	3	2	13
		0.198	2	1	18						
		0.201	2	2	16						
		0.195	3	2	15						
		0.208	4	1	17						
		0.204	4	2	13						

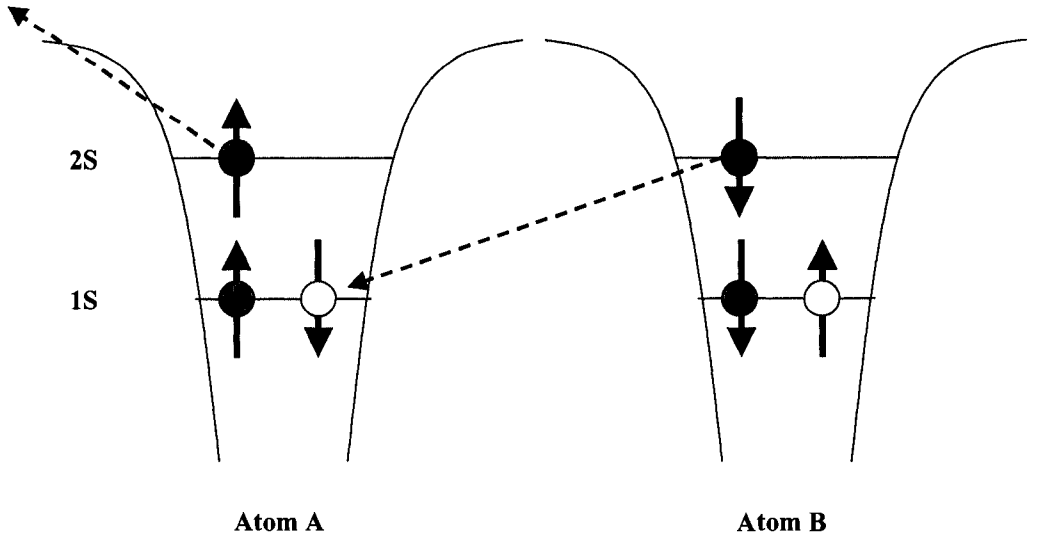

FIG. 50: Schematic of Penning ionization in He*.

potentials where Ω=0,1,2,3, and 4 arise because of this broadening effect. In the PAS of He*, they have made preliminary assignments of the observed resonances (observed as increases in ionization) to vibrational states in an Ω=0 and an Ω=1 potential and they offer an explanation for the reason the resonances are not broadened by short lifetimes [34]. This explanation states that, though the Ω=0,1 states should ionize resulting in broad peaks, there is a mixing of states in the region where the fine structure energy is comparable to the dipole-dipole interaction which allows for the transfer of the population from Ω=0 or 1 to the Ω=2 spin stretched state. This Ω=2 potential corresponding to the spin stretched state in He* has an ionization rate orders of magnitude less than that of the Ω=0,1 states [60]. This transfer of population to the Ω=2 potential occurs during the molecular vibrational period as the atoms approach from large R, reducing the rate of ionization and effectively increasing the lifetime (and hence decreased linewidth) of the state.

The PA spectra for Ar* are qualitatively different from those of He* along the trapping transitions. In the He* spectra, the resonances are clearly increases in the ionization rate while in the PAS of Ar*, a broad background of an increased ionization rate shows features where the ionization rate is dramatically decreased and changes as a function of intensity. In the PAS of He* along a different transition $2s[3/2]_2$ + $2p[5/2]_2$ shows similar effects as the probe intensity is changed, where dip-like

features at one intensity become peaks at a different probe intensity. Neihaus *et al.* offer the explanation that this observation is attributed to channel competition between the long-range molecular states and the pure-long-range molecular states in He*. Pure long range states are states where both the inner and outer classical turning points are located at more than a few a_0 internuclear distance where the atoms never get close enough to ionize. These pure-long-range states are generally brought about by perturbations in the molecular potential due to near-by potentials with identical symmetries. If present in Ar* along the $4s[3/2]_2 + 4p[5/2]_3$ potentials, exciting to these states could result in the observed decrease in ionization. Upon close investigation of the calculated curves shown in Figure 48 (which include only the dipole-dipole interaction), no pure-long-range states are found to exist in the $4s[3/2]_2 + 4p[5/2]_3$ potentials suggesting this is likely not the mechanism responsible for the dips of the ion signal in the PA spectra of Ar* (however, it should be noted that these states do exist along other Ar* S+P potentials).

Another mechanism that could potentially explain the dips in the PA spectra of Ar* could be the excitation to states where the vibrational period is much longer than the lifetime of the state. In the semiclassical picture, if the C_3 coefficient dominating a potential is very small, the gradient of the potential would also be extremely small at large internuclear distance where an elicitation to a vibrational bound state would most likely be made. Due to a small potential gradient, the nuclear kinetic energy of the two atoms does not increase quickly, extending the time they spend at large internuclear distances. When this time surpasses the typical excited state lifetime of the molecule, the molecule can dissociate before reaching small internuclear distances where ionization takes place. Upon inspecting Table V.2.1 and Figure 48 for a molecular potential of this nature, it is found that the most likely candidate will be the 1_g state with $C_3 = 2.9 \times 10^{-50}$ J m^3. However, as Figure 51 shows, the calculated locations of the vibrational states for this potential using the LeRoy-Bernstein Equation suggest this is not the mechanism responsible for the observed peaks.

This raises further questions of how the resonances seen in the PAS of Ar* arise. If Ar* lacked the strong coupling of states which allowed He* to mix states of different Ω, the ionization would occur very quickly for the non-spin stretched states, making resonances GHz wide and leading to a very broad PAS ion signal [59]. One might ask what to expect to observe for excitations to the series of states with Ω=5. These

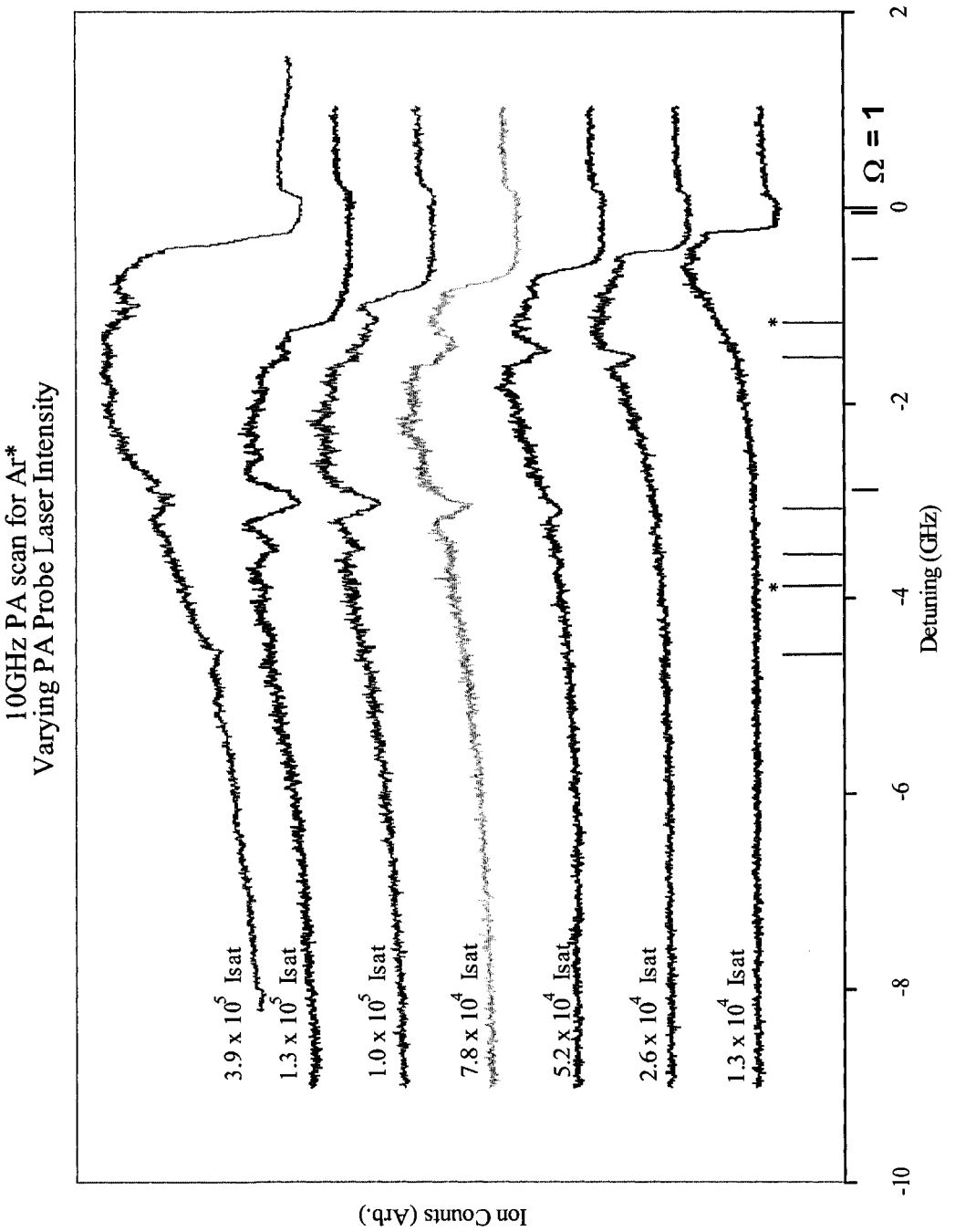

FIG. 51: The 10GHz PA spectrum for Ar* with the vibrational states from the $\Omega{=}1_g$, $C_3 = 2.9 \times 10^{-50}$ J m^3 potential indicated along the x axis. Spectra are plotted in order of increasing PA intensity starting with the lowest value on the bottom.

spin stretched states connect to the $4s[3/2]_2 + 4p[5/2]_3$ asymptote. When the LeRoy-Bernstein equation is used to calculate vibrational resonances of the Ω=5 potential, it is found that the observed resonances at δ=3.07, 1.44, 1.10, and 0.22 GHz may have contributions from vibrational states in this potential. Upon inspecting of Table III, there are in fact vibrational states from this potential within the experimental uncertainty of the PA probe laser. Figure 52 shows a visual representation of where the vibrational series for the Ω=5 potential would be located. Without a doubt, the possible agreement warrants further investigation. For now, only preliminary assignments can be suggested.

If this is the mechanism responsible for the observed features in the PA spectra of Ar*, the effect would be most noticeable in a spin polarized sample. The MOT, however, is to a large degree an unpolarized sample of atoms due to the magnetic field gradient produced by the anti-Helmholtz coils and the many polarizations of light present. Though this is often the case, it is not impossible that the MOT has some degree of polarization that changes day to day. The fact that the features were more defined in spectra taken some days than others could be explained by this. To verify these results, the experiment would need to be repeated in a spin polarized sample of Ar* atoms and the suppression of ionization by spin polarization measured.

V.2.3 Contributions of Rotational Energy Levels

As previously discussed, the rotational energy constant B_ν for levels near dissociation can be explicitly expressed in terms of parameters of the vibrational level, including the leading power and coefficient of the molecular potential n and C_n, the energy difference from dissociation $D - E(\nu)$, and the reduced mass of the system μ.

$$B_\nu = \frac{\hbar}{4\pi\mu c}\left(\frac{D - E(\nu)}{C_n}\right)^{2/n} \frac{\Gamma(1+1/n)\Gamma(1/2-1/n)}{\Gamma(1/2+1/n)\Gamma(1-1/n)} \tag{84}$$

When estimating how rotational levels may affect the spectra for an experiment such as photoassociative spectroscopy, the fact that the system is being excited from the ground state to an excited state needs to be considered. Since the "ground state" in this experiment is of some distribution of rotational states, it is important to consider not just the rotational levels along the potentials being excited to, but also to include the possible rotational states that we may be exciting from. This is especially the case when considering bound-bound transitions where excitations are

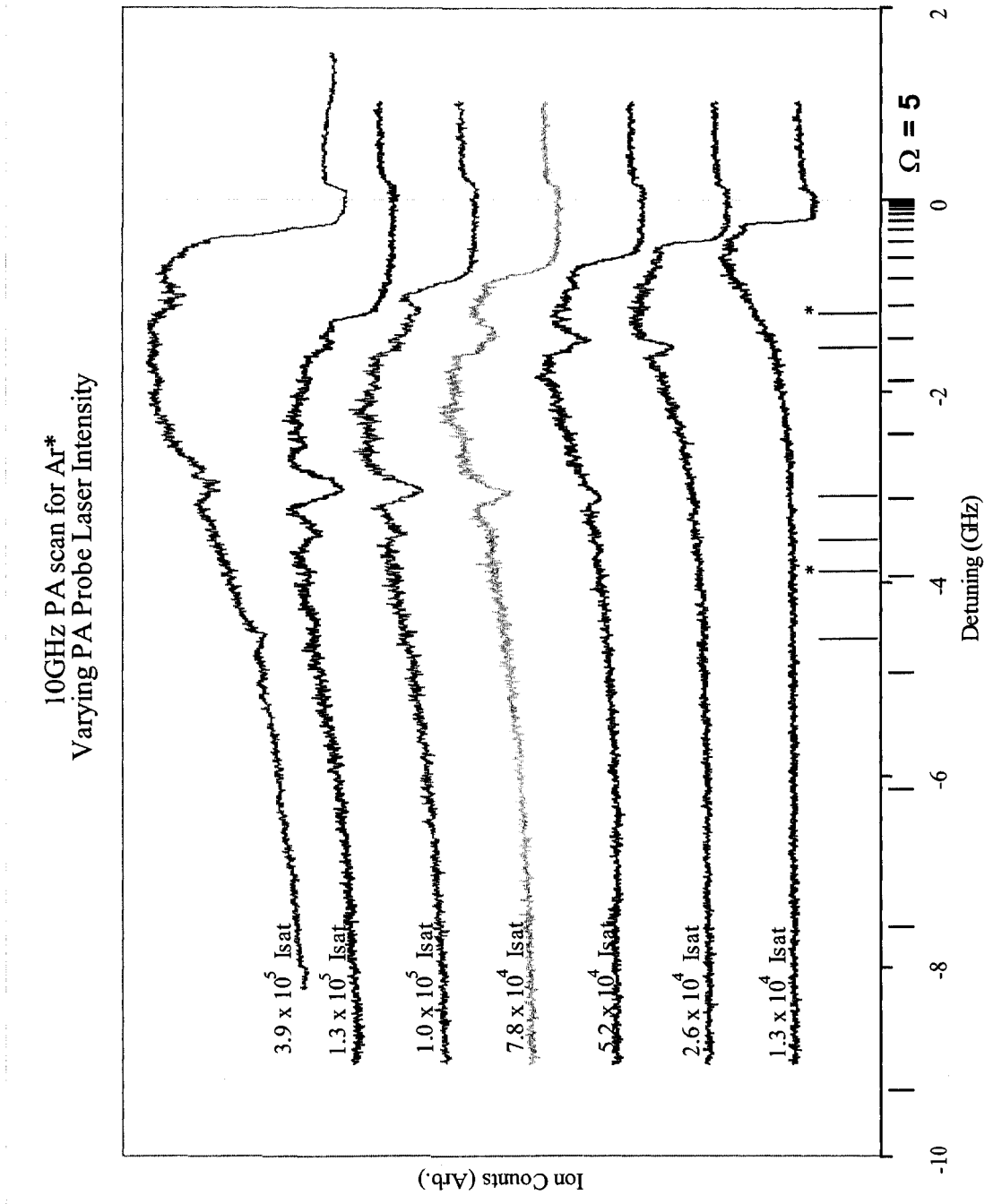

FIG. 52: The 10GHz PA spectrum for Ar* with the vibrational states from the Ω=5 potential indicated along the x axis. Spectra are plotted in order of increasing PA intensity starting with the lowest value on the bottom.

made going from one bound ro-vibrational state to another. Including the structure of the ground and excited states is important in this case and leads to the P, Q and R branches ($\Delta J = -1, 0$ or $+1$) of the rotational spectra that may be resolved in some spectra.

In this experiment, however, free-bound transitions are taking place during photoassociation where the atoms are initially free in the ground state and are excited into a bound ro-vibrational state. This means that only the excited state rotational structure and the contributing partial waves need to be considered. At typical MOT temperatures, the thermal width of the free atoms is only ~10 MHz, resulting in contributions from just a few partial waves.

If two similar atoms undergo a collision while one atom is singly excited, the potential is then dominated by the $n = 3$, or $V(R) \approx D - C_3/R^3$ dipole-dipole potential. Giving the upper state the primed designation of B'_ν, the expression becomes

$$B_\nu = \frac{\hbar}{4\pi\mu c}\left(\frac{D - E(\nu)}{C_3}\right)^{2/3} \frac{\Gamma(1+1/3)\Gamma(1/2-1/3)}{\Gamma(1/2+1/3)\Gamma(1-1/3)} \tag{85}$$

giving

$$B_\nu = \frac{\hbar}{4\pi\mu c}\left(\frac{D - E(\nu)}{C_3}\right)^{2/3} 2.6015 \tag{86}$$

To give an estimate of the contributions that rotational energy structure may have towards the observed spectra, consider that the rotational energy spacing are given by the expression

$$E_{rot} = B_\nu[J_T[J_T + 1] - \Omega^2] \tag{87}$$

where J_T is the total angular momentum (including that of the rotating molecule). If it were the case where a transition was being made from a bound molecular state to another (bound-bound transition), then the rotational energy level structure of both states would need to be considered when estimating how it would affect the observed spectra (since selection rules state $\Delta J_T = 0, \pm 1$ leading to the P, Q and R branches for $\Delta J_T = -1, 0$ and 1 respectively). For this experiment, however, photoassociation is a free-bound transition where two free atoms, with energy above the dissociation level of the ground state potential, undergo a transition into a bound excited molecular state. Because the ground state atoms lie in some thermal distribution above

dissociation, the energy differences between nearest neighbor rotational states result in sub-megahertz energy differences. This makes valid the approximation that only the rotational level spacings of the bound excited molecule need to be considered.

For this assessment, consider the $\Omega = 5$ molecular potential with contributions from the first three partial waves ($l = 0, 1, 2$) correspondingly to the total angular momentum of ($J_T = 5, 6, 7$) which can be expected at these temperatures. The resonance of interest will be located at 3 GHz detuning from dissociation ($D - E(\nu) =$ 3.0 GHz). For these figures, $B_\nu \sim 3.1$ MHz, leading that the first three partial waves would contribute additional resonances at 13, 44, and 80 MHz red of the -3.0 GHz resonance. Upon inspecting the shape of the resonance in the spectra, no additional peaks due to rotational spectra are resolved, but this does not exclude the possibility that some of the broad linewidth of the peak is not due to unresolved rotational spectra.

V.3 SUMMARY OF THE AR* PHOTOASSOCIATIVE SPECTROSCOPY RESULTS

For the first time, photoassociative spectroscopy of Ar* has been conducted. The exploratory experiment focused on the $4s[3/2]_2 + 4p[5/2]_3$ asymptote associated with the trapping transition in Ar*. Spectra taken over 10 GHz at various probe laser intensities have revealed twelve molecular resonances observed in the ion signal. The LeRoy-Bernstein equation was used to calculate the possible vibrational states in the many molecular potentials along this asymptote. When compared to the locations of the observed resonances, the locations of the calculated vibrational states suggest a number of molecular potentials could be responsible. Preliminary assignments are made with consideration to the experimental uncertainty in laser frequency. Various possible mechanisms were explored to explain the character of the PA spectra and its differences to those observed in the PA spectra of He*. Though some mechanism are more likely than others, further investigation is necessary to come to a definitive conclusion regarding the dominating mechanism.

CHAPTER VI

CONCLUSION AND OUTLOOK

The interspecies trap loss rate coefficients have been measured for ultracold collisions between Rb and Ar* in a dual-species MOT and the two rates have been found to be approximately equal over the range of intensities studied. In addition, the trap loss rate coefficient for cold collisions in a metastable argon MOT alone have been measured. Using a quadrupole mass spectrometer the production of Ar^+, Ar_2^+, Rb^+, and $RbAr^+$ ions in the dual MOT have been observed, clearly identifying heteronuclear Penning and associative ionization as trap loss mechanisms.

In a step towards the photoassociative spectroscopy of Rb+Ar* and production of RbAr molecules, the first ever investigation of the photoassociative spectroscopy of Ar* has been made. With scans that go out 10 GHz red of the atomic transition, 12 resonances have been observed yielding preliminary state assignments. Qualitatively, the acquired PA spectra for Ar* show both similarities and differences to He* PA spectra recently obtained by other groups, raising interesting questions which clearly warrant further investigation of this system.

Future studies will focus on characterizing the molecular energy levels of Rb+Ar* using photoassociative spectroscopy and on the production of ultracold, ground state RbAr, a weakly bound van der Waals molecule.

BIBLIOGRAPHY

[1] V.I. Balykin, V.S. Letokhov, and V.I. Mushin, Pisma Zh. Eksp. Teor. **29**, No. 10, 614 (1979).

[2] J.E. Bjorkholm, R.R. Freeman, A. Ashkin, and D.B. Pearson, Phys. Rev. Lett. **41**, 1361 (1978).

[3] E. L. Raab, M. Prentiss, Alex Cable, Steven Chu, and D. E. Pritchard, Phys. Rev. Lett. **59**, 2631 (1987).

[4] M. H. Anderson, J. R. Ensher, M. R. Matthews, C. E. Wieman, E. A. Cornell, Science, **269**, 198 (1995).

[5] K. B. Davis, M.-O. Mewes, M. R. Andrews, N. J. van Druten, D. S. Durfee, D. M. Kurn, and W. Ketterle, Phys. Rev. Lett. **75**, 3969 (1995).

[6] C. C. Bradley, C. A. Sacket, J. J. Tollett, and R. G. Hulet, Phys. Rev. Lett. **75**, 1687 (1995).

[7] D. G. Fried, T. C. Killian, L. Willmann, D. Landhuis, S. C. Moss, D. Kleppner, and T. J. Greytak, Phys. Rev. Lett. **81**, 3811 (1998).

[8] F. Pereira Dos Santos, J. Leonard, J. Wang, C.J. Barrelet, F. Perales, E. Rasel, C.S. Unnikrishnan, M. Leduc, and C. Cohen-Tannoudji, Phys. Rev. Lett.**86**, 3459 (2001).

[9] J. M. McGuirk, G. T. Foster, J. B. Fixler, M. J. Snadden, and M. A. Kasevich, Phys. Rev. A **65**, 033608 (2002).

[10] M. Takamoto, F.-L Hong, R. Higashi, and H. Katori, Nature **435**, 321 (2005).

[11] D. DeMille, Phys. Rev. Lett. **88**, 067901 (2002).

[12] M. Saffman and T.G. Walker, Phys. Rev. A **72**, 022347 (2005).

[13] A. Wallraff, D. I. Schuster, A. Blais, L. Frunzio, J. Majer, M.H. Devoret, S. M. Girvin, and R. J. Schoelkopf, Phys. Rev. Lett. **95**, 060501 (2005).

[14] For a review see, J. T. Bahns, P. L. Gould, and W. C. Stwalley, Formation of Cold (T<= 1K) Molecules, Adv. At. Mol. Opt. Phys. 42, 172 (2000).

[15] For a review see, H.L. Bethlem and G. Meijer, Production and application of translationally cold molecules, Int. Rev. in Physical Chem. 22, 73 (2003).

[16] M.B. El Hadj Rhouma, H. Berriche, Z.B. Lakhdar, F. Spiegelman, J. Chem. Phys. **116**, 1839 (2002).

[17] T. Takekoshi, B. M. Patterson, R. J. Knize, Phys. Rev. Lett. **81**, 5105 (1998).

[18] A. Fioretti, D. Comparat, A. Crubellier, O. Dulieu, F. Masnou-Seeuws, and P. Pillet, Phys. Rev. Lett. **80**, 4402 (1998).

[19] C. Gabbanini, A. Fioretti, A. Lucchesini, S. Gozzini, and M. Mazzoni, Phys. Rev. Lett. **84**, 2814 (2000).

[20] A. N. Nikolov, E. E. Eyler, X. Wang, H. Wang, J. Li, W. S. Stwalley, and P. L. Gould, Phys. Rev. Lett. **82**, 703 (1999).

[21] D. Wang, J. Qi, M.F. Stone, O. Nikolayeva, H. Wang, B. Hattaway, S.D. Gensemer, P.L. Gould, and W.C. Stwalley, Phys. Rev. Lett. **93**, 243005 (2004).

[22] M.W. Mancini, G.D. Telles, A.R.L. Caires, V.S. Bagnato, and L.G. Marcassa, Phys. Rev. Lett. **92**, 133203 (2004).

[23] K. Gibble, S. Chang, and R. Legere, Phys. Rev. Lett. **75**, 2666 (1995)

[24] L. Marcassa, S. Muniz, E. de Queiroz, S. Zilio, V. Bagnato, JWeiner, P.S. Julienne, K.-A. Suominen, Phys. Rev. Lett. **73**, 1911 (1994).

[25] J. Lawall, C. Orzel, and S. L. Rolston, Phys. Rev. Lett. **80**, 480 (1998).

[26] M. S. Santos, P. Nussenzveig, L. G. Marcassa, K. Helmerson, J. Flemming, S. C. Zilio, and V. S. Bagnato, Phys. Rev. A **52**, R4340 (1995).

[27] J.P. Shaffer, W. Chalupczak, and N.P. Bigelow, Phys. Rev. Lett. **82**, 1124 (1999).

[28] G. D. Telles, L. G. Marcassa, S. R. Muniz, S.G. Miranda, A. Antunes, C. Westbrook, and V. S. Bagnato, Phys. Rev. A **59**, R23 (1999).

[29] U. Schloder, h. Engler, U. Schunemann, R. grimm, and M. Weidemuller, Eur. Phys. J. D **7**, 331 (1999).

[30] W. Sptitz, G. Wokurka, F. Strauch, P. Kohns, and W. Ertmer, Opt. Lett. **19**, 1571 (1994).

[31] M-O Mewes, G. Ferrari, F. Schreck, A. Sinatra, and C. Salomom, Phys. Rev. A **61**, 011403(R) (1999).

[32] S.G. Crane, X. Zhao, W. Taylor, and D.J. Vieira, Phys. Rev. A **62** 011402(R) (2000).

[33] T. Loftus, J.R. Bochinski, and T.W. Mossberg, Phys. Rev. A **63**, 053401 (2001).

[34] N. Herschbach, P. J. J. Tol, W. Vassen, W. Hogervorst, G. Woestenenk, J. W. Thomsen, P. van der Straten, A. Niehaus, Phys. Rev. A **61**, 050702(R) (1999).

[35] W. Demtröder, *Atoms, Molecules and Photons* (Springer, Verlag Berlin Heidelberg, 2006).

[36] H.J. Metcalf, P. van der Straten, *Laser Cooling and Trapping*(Springer, New York,1999).

[37] P. L. Gould, P. D. Lett, P. S. Julienne, and W.D. Phillips, Phys. Rev. Lett. **60**, 788 (1987).

[38] W. Ketterle, K. B. Davis, M. A Joffe, A. Martin, and D Pritchard, Phys. Rev. Lett. **70**, 2253 (1993).

[39] P. D. Lett, K. Helmerson, W. D. Phillips, L. P. Ratliff, S. L. Rolston, and M. E. Wagshul, Phys. Rev. Lett. **71**, 2200 (1993).

[40] D. Leonhardt, J. Weiner, Phys. Rev. A **52**, 1419 (1995).

[41] R. J. LeRoy and R. B. Bernstein, J. Chem. Phys. **52**, 3869 (1970).

[42] J. M. Brown, A. Carrington, *Rotational Spectroscopy of Diatomic Molecules*(Cambridge University Press, New York,2003).

[43] J. Frank, Trans. Faraday Soc. **21**, 536 (1925).

[44] E. U. Condon, Phys. Rev. **32**, 858 (1928).

[45] G. Herzberg, *Molecular Spectra and Molecular Structure*(Krieger Publishing Co. Inc., Florida,1989).

[46] C. Y. Chen, K. Bailey, Y. M. Li, T. P. O'Conner, Z.-T. Lu, X. Du, L. Young, and G. Winkler, Rev. of Sci. Instrum. **72**, 271 (2001)

[47] Hauke Busch Ph.D. Dissertation (2004).

[48] K.S. Repasky, A.R. Nehrir, J.T. Hawthorne, G.W. Switzer, and J.L. Carlsten, Appl. Opt. **45** 9013, (2006).

[49] H. C. Busch, M.K. Shaffer, E. M. Ahmed, and C. I. Sukenik, Phys. Rev. A **73**, 023406 (2006).

[50] C. Wallace, T. Dinneen, K. Tan, T. Grove, and P. Gould, Phys. Rev. Lett. **74**, 1087 (1995).

[51] L.G. Marcassa, G.D. Telles, S.R. Muniz, and V.S. Bagnato, Phys. Rev. A **63**, 013413 (2000).

[52] J. Goldwin, S.B. Papp, B. DeMarco, and D.S. Jin, Phys. Rev. A **65**, 021402(R) (2002).

[53] Y.E. Young, R. Ejnisman, J.P. Shaffer, and N.P. Bigelow, Phys. Rev. A **62**, 055403 (2000).

[54] M.W. Mancini, A.R.L. Caires, G.D. Telles, V.S. Bagnato, and L.G. Marcassa, Eur. Phys. J. D **30**, 105 (2004).

[55] L. Marcassa, R. Horowicz, S. Zilio, V. Bagnato, J. Weiner, Phys. Rev. A **52**, R913 (1995).

[56] K.A. Suominen, K. Burnett, P. S. Julienne, M. Walhout, U. Sterr, C. Orzel, M. Hoogerland, and S. L. Rolston, Phys. Rev. A **53**, 1678 (1996).

[57] H. Katori and F. Shimizu, Phys. Rev. Lett. **73**, 2555 (1994).

[58] N. Herschbach, P.J.J. Tol, W. Hogervorst, and W. Vassen, Phys. Rev. A **61**, 050702(R) (2000).

[59] M. R. Doery, E. J. D. Vredenbregt, J. G. C. Tempelaars, H. C. W. Beijerinck, and B. J. Verhaar , Phys. Rev. A **57**, 5 (1998).

[60] N. Herschbach, P. J. J. Tol, W. Hogervorst, W. Vassen, Phys. Rev. A **61**, 050702(R) (1999).

[61] Edgar Vredenbregt, Private Communications. (S+P curve program written by M.R. Doery).

[62] K.B. MacAdam, A. Steinbach, and C. Wieman, Am. J. Phys. **60** 1098, (1992).

[63] C.E. Wieman and L. Hollberg, Rev. Sci. Instr. **62** 1, (1991).

[64] T. Hansch, Appl. Opt. **4** 895, (1972).

[65] M.G. Littman and H.J. Metcalf, Appl. Opt. **17** 2224, (1978).

[66] L. Nilse, H.J. Davies, and C.S. Adams, Appl. Opt. **38** 548, (1999).

[67] M. de Labachelerie and G. Passedat, Appl. Opt. **32** 269, (1993).

[68] V.V. Vassiliev, S.A. Zibrov, and V.L. Velichansky, Rev. Sci. Instrum. **77** 013102 (2006).

[69] C. Petridis, I.D. Lindsay, D.J.M. Stothard, and M. Ebrahimzadeh, Rev. Sci. Instrum. **72** 3811, (2001).

[70] A. Andalkar, S.K. Lamoreaux, and R.B. Warrington, Rev. Sci. Instrum. **71** 4029, (2000).

[71] V.P. Gerginov, Y.V. Dancheva, M.A. Taslakov, S.S. Cartaleva, Opt. Comm. **149** 162, (1998).

[72] T. Nayuki, T. Fujii, K. Nemoto, M. Kozuma, M. Kourogi, M. Ohtsu, Opt. Rev. **5** 267, (1998).

APPENDIX A

LAB VIEW DATA ACQUISITION PROGRAM

This section addresses and comments on the Lab View program used for data acquisition of the photoassociative spectroscopy section of this thesis. The working program, which communicates to the srs400 photon counter, Burleigh wavemeter and the NI DAQ board, is named "PAS_Main_DAQ_buff_wave_etalon_2pmt.vi". In brief the program will create or open a specific file, initialize the SRS400 photon counter, recursively read available data from the photon counter, wavemeter, and DAQ card, store that data in an array of arbitrary size, and upon data run completion will write that data in tab delimited spreadsheet formatted text file.The program begins by clicking the "Run" button on the front panel view and continues to acquire data until the large green boolean is clicked.

More specifically, the "PAS_Main_DAQ_buff_wave_etalon_2pmt.vi" program follows the following, more detailed, description. After the "Run" button has been clicked, the program will either an existing or create a file, whose name and path is given in the code panel, and will write the date and time of the run followed by a carriage return. The program will then initialize the SRS400 photon counter, declaring proper ports, sending commands to reset and start the counter and reading in any outgoing communications from the counter that may be in the buffer, clearing the SRS400 buffer, priming for subsequent communications. Values passed from the leftmost sequence frame are the file name and path and the port value for the SRS400.

In the second sequence frame, a while loop begins with a manual boolean as its case. Within the loop, the status of the SRS400 "data ready" is queried. If data is ready, a case structure will sequentially read the SRS400 Channel A data, SRS400 Channel B data, 5 voltage values (BNC 2, 3, 4, 5, 6) from the NI DAQ board, and the Wavemeter value. If the SRS400 data ready status returns data NOT ready, all fields will be assigned the value of -9999999. After the case structure, all fields are indexed in an array of arbitrary size (along with the CPU time of each iteration of diagnostics). When the boolean is manually changed on the front panel, the while loop will exit and the indexed array of data and the file name and path will be passed.

The final sequence frame of the program is for post conditioning and file writing. Here the data array is scanned for "good" data. If a row in the array has "-9999999"

as a value, the row is discarded, if it does not, the data is considered "good" and is written to the file. Once each row in the array has been scanned, the file is closed and the program terminates.

It should be noted that the wavemeter serial rs232 communications code was modified from legacy code previously written by Dr. Mark Havey. This sub-VI sends a command to the wavemeter requesting a data string, waits for the string, and decodes the incoming string extracting the wavelength value.

APPENDIX B

EXTENDED TUNING OF A SLAVE DIODE LASER

To appear in *Review of Scientific Instruments*

M.K. Shaffer, G. Ranjit, and C.I. Sukenik
Old Dominion University, Department of Physics,
Norfolk, Virginia 23529

Semiconductor diode lasers are used in both commercial applications and experimental physics as a result of their low cost, high efficiency, and broad wavelength coverage. This has been especially true in atomic and molecular physics experiments [62, 63]. Because both precise tunability and frequency stability are often important, it is common to construct an external cavity diode laser (ECDL) by using a frequency-selective optical element such as a diffraction grating in the cavity to control the frequency of the light which is fed back to the laser diode. If the front facet of the laser diode has sufficiently low reflectivity, the laser output frequency is then determined by the external cavity. Tuning is achieved by rotating the grating or a mirror, depending on the cavity design [64, 65]. If the laser is to operate at a fixed wavelength, then placement of the tuning element in the cavity is usually not too important; however, if frequency scanning is required- as in spectroscopy experiments, for example- then cavity geometry is critical. If the pivot point of the tuning element in the cavity is not precisely positioned in order to keep the cavity length commensurate with the new wavelength during tuning, the laser will intermittently mode-hop or run multi-mode as it is scanned [66, 67]. Correct positioning of the pivot point however, requires micron level accuracy and is not trivial. Several authors have demonstrated techniques for increasing the scan range of an ECDL by applying feed-forward adjustments to the laser diode current as the external cavity is mechanically adjusted [68, 69, 70, 71, 72]. Recently, Repasky, *et al.* [48] described an electronic feedback technique to enable very long mode hop-free scans of an ECDL.

In this Note, we describe our investigation of the application of the technique in [48] to an injection-locked diode laser system. In injection locking, light from a "master" laser is sent directly into a "slave" laser causing it to lase with the spectral properties of the master, but usually providing higher power than one would obtain

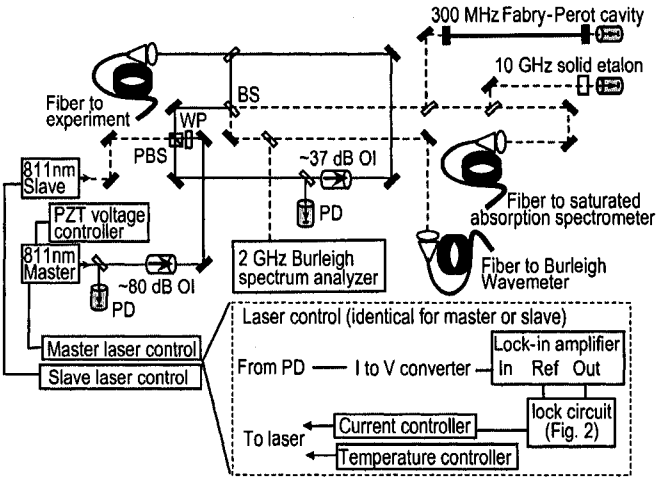

FIG. 53: Schematic of experimental setup. PBS: polarizing beamsplitter cube; BS: beamsplitter; WP: waveplate; OI: optical isolator; PD: photodiode; Dashed optical path indicates master and slave laser beam overlap.

from the master alone. If the laser is to be scanned, it is critical that the slave laser smoothly follow the master during scanning. We have found that an injection-locked diode laser will typically follow the master for only ~500 MHz before it begins to operate multi-mode, thereby limiting the utility of the long scan capability of the ECDL.

In [48] a small modulation was placed on the laser current and phase-sensitive detection was used to monitor the laser power. If the laser cavity does not maintain the resonance condition during scanning, sideband suppression is reduced and the amplitude and phase of the modulated power change, thereby providing an "error signal" which can be applied to the laser current in order to bring the cavity back into resonance. Using this approach, Repasky *et al.* were able to extend the mode-hop free tuning of a Littman-Metcalf ECDL, operating at 758 nm, from 1 GHz to more than 65 GHz. We have implemented this technique to an injection-locked diode laser system and find that although the amplitude and phase characteristics of the modulated power of the slave laser differ from those of the ECDL, a suitable error signal- used to send feedback to the slave current and allow the slave laser to stay in resonance with the master laser- is still produced. We have investigated two separate injection-locked laser systems, one with an ECDL in Littman-Metcalf configuration

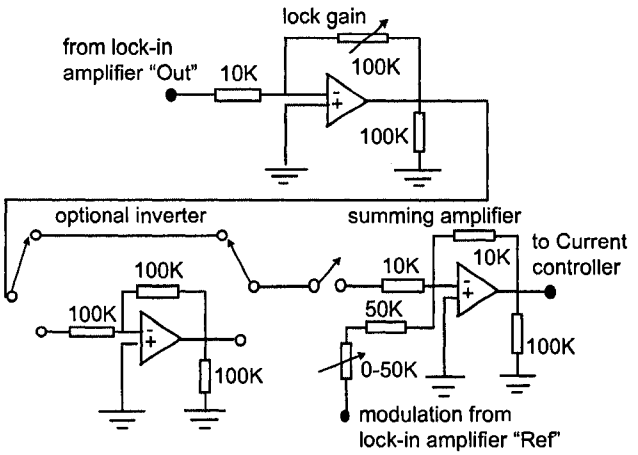

FIG. 54: Amplifier circuit with gain and polarity control for providing combined modulation and error signal to the diode laser current controller. All operational amplifiers are 1/4 TL074.

and the second operating in Littrow configuration. In both setups, no attempt was made to correctly position the pivot point of the tuning element. We found the same performance in both setups. Here we report details of the apparatus using the Littman-Metcalf ECDL.

A schematic of the experimental arrangement is shown in Figure 53. An 808 nm 150 mW diode laser (Sanyo DL-LS2031) was collimated (Thorlabs L110P-B) and placed in a 7 cm long external cavity containing a 1200 lines/mm diffraction grating (Edmund Scientific K43-848). The laser was tuned by applying a voltage to a piezoelectric transducer (PZT) placed behind the horizontal adjust of the cavity mirror. The PZT (Thorlabs AE0203D08F) has an extension of 6.1 μm at 100 V. The master laser was temperature stabilized to $\sim$10 ppm with a homemade temperature controller and operated at 125 mA with a homemade current controller. At this current, the ECDL output is 26 mW. With no electronic feedback, the laser scans $\sim$1.5 GHz before mode-hoping. We monitor the laser output with light reflected off an uncoated glass beam splitter and detected on an external photodiode as shown in Figure 53. We modulate our laser current at 8 kHz. Output of the photodiode is directed to a current to voltage converter and then sent to the input of a Princeton Applied Research PAR 120 lock-in amplifier. The lock-in amplifier also provides the

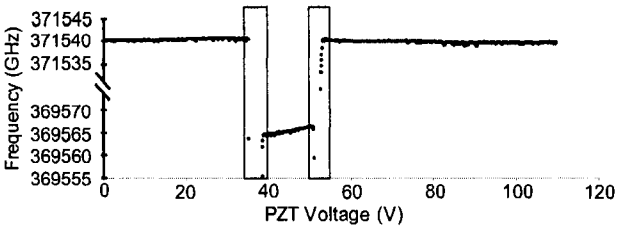

FIG. 55: Output frequency of slave laser without electronic feedback vs. master laser PZT voltage (corresponding to master laser frequency). Boxed region indicates multi-mode behavior.

reference signal used to modulate the laser current. The lock-in amplifier demodulates the photodiode signal. If the amplitude and/or phase characteristics of the photodiode signal (at the modulation frequency) change, the voltage output of the lock-in amplifier also changes. This output voltage can be used as an error signal to provide feedback to the diode laser current. We use the time constant setting of the PAR 120 to provide integration and the zero-adjust feature (DC offset) to subtract a fixed voltage from the output and lock the laser to the zero-crossing of the output signal. The output of the lock-in amplifier is sent to the simple amplifier circuit shown in Figure 54 to provide gain and polarity control of the integrated error signal and sum it with the modulation needed for the phase sensitive detection of the laser power. The output of the lock circuit is then sent to the current controller where it is summed with the set point voltage which controls the laser current. When the feedback technique of [48] is applied, we are able to scan the ECDL by 23 GHz, limited by the full extension of the PZT element.

Light from the ECDL is injected into a collimated slave laser (Sanyo DL-LS2031, Thorlabs L230P-B). The laser current is 168 mA. Only tens of μW of light is required to injection-lock the slave when the two polarizations are the same. We find it convenient to direct the ECDL light into the slave via a polarizing beam splitter cube. In this configuration, the injected light has a polarization nearly perpendicular to the slave light and it typically requires a few mW to pull the slave. Though the ECDL is now capable of scanning 23 GHz, the slave laser (without electronic feedback) will only be pulled single mode for a small range of $\sim$600 MHz and will then run multi-mode before switching to its free-running wavelength as shown in Figure 55,

where the laser frequency (monitored by a Burleigh WA-1000 wavemeter) is plotted vs. ECDL PZT voltage. Additional laser diagnostics are provided by a low finesse 300 MHz Fabry-Perot cavity, a low finesse 10 GHz solid etalon, and a high finesse 2 GHz optical spectrum analyzer. A saturated absorption spectrometer is used to provide an absolute wavelength reference.

In an attempt to extend the scan range of the slave, we have applied the same technique used on the master laser to the slave laser. Here, the current of the slave laser diode is modulated at 12 kHz (so as to not interfere with the master ECDL lock circuitry) and the modulated power is again monitored on a photodiode. (In an alternate arrangement, we have also used the internal photodiode of the laser diode to monitor the power). As the frequency of the master laser is scanned, the amplitude and phase characteristics of the modulated power of the slave laser change resulting in a change to the output voltage of the lock-in amplifier. The presence of the modulation added to the current can be observed as an AC component of the total output power of the laser, which we will refer to as P_{mod}, having amplitude A_{mod} and phase ϕ_{mod} relative to the reference modulation signal. Figure 56a (56b) shows A_{mod} (ϕ_{mod}) for both the master and slave laser as the master laser is scanned, with no feedback applied to either laser. A_{mod} is normalized to its maximum value during the scan. Figure 56 c shows the resulting error signal (with DC offset applied) produced by the lock-in amplifier. As seen in Figs. 4a and 4b, the amplitude and phase characteristics of the modulated power of the slave laser do in fact differ from those of the master. What matters for locking the slave laser, however, is that the demodulated signal (the output of the lock-in amplifier) has a form which can be used as an error signal. Indeed, as can be seen in Figure 56c, where the output of the lock-in amplifier (with DC offset applied) is shown, a perfectly suitable error signal is produced. Finally, in Figure 56d, we show the normalized total output power of each laser as it is scanned without electronic feedback. When the error signal is integrated, sent to the locking circuitry of Figure 54, and forwarded to the slave laser current controller, the slave laser is now capable of following the master ECDL over the full 23 GHz scan range as shown in Figure 57, where the wavemeter output and transmission through a 10 GHz solid etalon are displayed.

In conclusion, we have investigated the application of an electronic feedback technique to an injection-locked diode laser. We find that without the electronic feedback, the slave laser will only follow the master ECDL for ~600 MHz, but once locked the

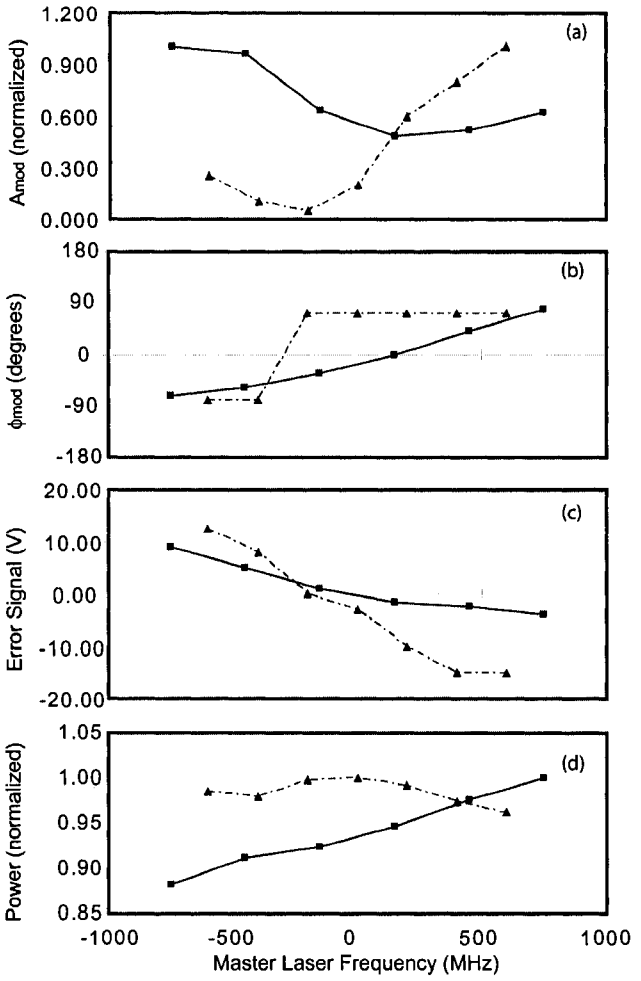

FIG. 56: For master laser (squares) and slave laser (triangles): (a) normalized A_{mod} vs. laser frequency; (b) ϕ_{mod} vs. laser frequency; (c) output of the lock-in amplifier (used as the error signal) vs. laser frequency; and (d) normalized total laser power vs. laser frequency.

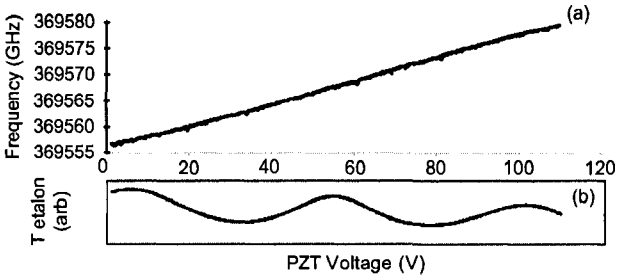

FIG. 57: (a) Output frequency of slave laser with electronic feedback vs. master laser PZT voltage; (b) Transmission of slave laser light through a 10 GHz solid etalon vs. master laser PZT voltage.

slave laser is capable of following the full scan range of the master laser. We expect that the scanning range can be extended even further by application of a piezoelectric element with greater displacement capability. We gratefully acknowledge support from the National Science Foundation. We thank K.S. Repasky for helpful correspondence.

VITA

Michael K. Shaffer
Department of Physics
Old Dominion University
Norfolk, VA 23529

Education

Ph.D. in Physics, 2008, Old Dominion University, Norfolk, Virginia.
M.S. in Physics, 2004, Old Dominion University, Norfolk, Virginia.
B.S. in Physics, 2002, Frostburg State University, Frostburg, Maryland.

Awards

Dissertation Fellowship, Old Dominion University, 2007-2008.

Experiences

Graduate Research Assistant in Experimental Ultracold Atomic, Molecular, and Optical Physics, Old Dominion University. Advisor - Dr. Charles Sukenik, December 2004-May 2008.

Graduate Research Assistant in Experimental Mossbauer Spectroscopy, Old Dominion University, Advisor- Dr. Desmond Cook, September 2002- December 2004.

Graduate Teaching Assistant and Student Laboratory Instructor, Old Dominion University, June 2002- December 2004.

Research Assistant for Data Analysis for Geodynamics and Gravity Field modeling, Joint Center for Earth Systems Technology, University of Maryland Baltimore County, Advisor- Dr. Erricos Pavlis, June 2001- August 2001.

Research Assistant in Solar Physics, Johns Hopkins University Applied Physics Laboratory, Advisor- Dr. David Rust, June 2000- August 2000.

Journal Publications

"Trap Loss in a Dual Species Rb-Ar* Magneto-optical Trap," H.C. Busch, M.K. Shaffer, E.M. Ahmed, and C. I. Sukenik, Phys. Rev. A. **73**, 023406 (2006).
"Extended Tuning of an Injection-Locked Diode Laser" M.K. Shaffer, G. Ranjit, and C. I. Sukenik, (to appear in Rev. Sci. Instrum.)

Typeset using LaTeX.